Constraining the Cosmic Microwave Background Temperature Evolution and the Population and Structure of Galaxy Clusters and Groups from the South Pole Telescope and the Planck Surveyor

Jiayi Liu

Constraining the Cosmic Microwave Background Temperature Evolution and the Population and Structure of Galaxy Clusters and Groups from the South Pole Telescope and the Planck Surveyor

Jiayi Liu

Dissertation der Fakultät für Physik
Dissertation of the Faculty of Physics

der Ludwig-Maximilians-Universität München
at the Ludwig Maximilian University of Munich

für den Grad des
for the degree of

Doctor rerum naturalium

vorgelegt von Jiayi Liu
presented by

aus Beijing, China
from

München, den 29.07.2014

1^{st} Evaluator: Prof. Dr. Joseph Mohr

2^{nd} Evaluator: P.D. Dr. Klaus Dolag

Date of the oral exam: 29-07-2014

Zusammenfassung

Galaxienhaufen, riesige, massereiche Systeme die aus bis zu mehreren hundert Galaxien bestehen, stellen kosmologische und astrophysikalische Laboratorien von unschätzbarem Wert dar. Neben ihrer faszinierenden Galaxien beinhalten sie dunkle Materie, dessen tiefes Gravitationspotential sogar Licht ablenkt und so Abbildungen des Hintergrundes verzerrt. Baryonisches Gas wird beim Einfallen auf mehr als 10^7 K erhitzt wodurch freie Elektronen Röntgenlicht abstrahlen. Die Beobachtung dieser Phänomene hat bereits zu einem besseren Verständnis der Gravitation, der Teilchenphysik und der Hydrodynamik geführt. Des Weiteren hängt die Entstehung von Galaxienhaufen, die Maxima des Dichtefeldes darstellen, stark von den Anfangsbedingungen im Universum ab, wodurch sie sich hervorragend für kosmologische Untersuchungen eignen.

In dieser Arbeit werden wir zunächst die grundlegenden Eigenschaften des Universums klären und entsprechende Beobachtungen vorstellen. Dann werden wir zeigen, wie Galaxienhaufen aufgrund ihrer Rotverschiebungen und Massen für kosmologische Untersuchungen genutzt werden können. Allerdings ist die Masse nicht direkt messbar, so dass man sich anderer Beobachtungsgrößen bedienen muss. Wir werden optische, Röntgen- und Mikrowellenbeobachtungen einführen und erklären, wie diese genutzt werden können um Massen abzuschätzen. Nach dieser Einführung werden wir auf drei Arbeiten im Bereich der Astrophysik von Galaxienhaufen näher eingehen.

Zunächst werden wir eine Untersuchung von Galaxienhaufen, die von *Planck* aufgrund des Sunyaev-Zel'dovich Effekts (SZE) selektiert und von Panstarrs im Optischen beobachtet wurden, vorstellen. Um die volle Stärke von SZE Himmelsdurchmusterungen ausspielen zu können müssen die Rotverschiebungen der einzelnen Galaxienhaufen bekannt sein. In dieser Arbeit widmen wir uns 237 potentiellen Galaxienhaufen ohne gemessene Rotverschiebungen aus dem *Planck* Katalog. Wir bestätigen 60 dieser Kandidaten und präsentieren deren Rotverschiebung. Die Aufnahmen 83 weiterer Kandidaten, die sich alle nahe der galaktischen Ebene befinden, sind so stark von Sternen verunreinigt, dass wir weder die Zugehörigkeit einzelner Galaxien noch verlässliche Rotverschiebungen angeben können. Für die übrigen 94 Kandidaten konnten wir keine optischen Entsprechungen finden. Wir ermitteln die Genauigkeit unserer Rotverschiebungen, indem wir weitere 150 bestätigte *Planck* Haufen mit spektroskopischen Rotverschiebungen untersuchen, und messen $\sigma_{z/(1+z)} \sim 0.022$. Nach einem Vergleich mit dem bereits veröffentlichen *Planck*-Katalog erwarten wir, dass es sich, bis auf ein paar wenige Galaxienhaufen mit sehr hoher Rotverschiebung jenseits der von Pannstarrs erreichten Tiefe, bei den von uns nicht bestätigten Kandidaten um Rausch-Fluktuationen handelt. Wir verbinden die Tiefe der optischen Beobachtungen mit einem Modell der Galaxienpopulation von massereichen Galaxienhaufen um eine untere Grenze der Rotverschiebung anzugeben, jenseits derer wir eine optische Entsprechung nicht hätten beobachten können.

Des Weiteren benutzen wir South Pole Telescope (SPT) Beobachtungen mit 95GHz, 150GHz und 220GHz, um das SZE Signal von 46 Galaxienhaufen und Gruppen aus dem ~ 6 deg^2 Röntgenkatalog *XMM-Newton* Blanco Cosmology Survey (XMM-BCS) genauer zu studieren. Mit ihrer großen Spanne an Rotverschiebungen und den niedrigen Massen ergänzt diese Arbeit vorangegangene. Wir entwickeln eine Methode die es uns ermöglicht, anhand der Röntgen-Leuchtstärke und der dadurch abgeleiteten Masse die SZE Signifikanz- und $Y_{\rm sz}$-Massenrelationen zu bestimmen. Die SZE Signifikanz-Massenrelation stimmt mit der Extrapolation der selben Relation für höhere Massen überein. Unsere $Y_{\rm sz}$-Massenrelation stimmt zwar mit der Extrapolation der SPT Relation für höhere Massen überein, zeigt jedoch

eine 2,4σ Abweichung zur selben Relation von *Planck*, die ebenfalls für solch niedrige Massen ermittelt wurde, auf. Wir gehen weiter auf diese Abweichung ein und diskutieren Unterschiede in den Katalogen sowie mögliche systematische Fehler, die zu dieser beitragen können. Des weiteren untersuchen wir die Auswirkung von Radiogalaxien in unseren röntgen-selektierten Systemen. Wir identifizieren 18 Galaxienhaufen in denen sich 1 GHz Sydney University Molonglo Sky Survey (SUMSS) Quellen näher als 2 Bogenminuten zum Röntgenzentrum befinden; 3 davon wurden mit einer Signifikanz $> 4\,\sigma$ auch mit SPT nachgewiesen. Wir untersuchten den Einfluss dieser Punktquellen auf unser Ergebnis der SZE Skalierungsrelationen und fanden keinen Beleg für systematische Abweichungen. Wir untersuchten auch den Einfluss staubiger Galaxien. Durch Mittelung der 220 GHz Daten, fanden wir einen Hinweis auf einen Exzessfluss auf dem $2.8\,\sigma$ Signifikanzniveau, welcher einer mittleren Unterschätzung des SZE Signals von $(17 \pm 9)\%$ in diesem Ensemble von Systemen niedriger Masse entspräche. Schließlich sagen wir eine Verbesserung der Kentniss dieser SZE Masse-Observablen Skalierungsrelation um einen Faktor vier bis fünf, basierend auf zukünftigen Daten von SPTPol und XMM-XXL, vorher.

Schließlich stellen wir eine Arbeit vor, in der wir Galaxienhaufen verwenden, um mögliche Abweichungen von der adiabatischen Entwicklung der Temperatur der kosmischen Hintergrundstrahlung zu messen. Eine adiabatische Temperaturentwicklung ist eines der Fundamente des kosmologischen Standardmodells. Anhand des von SPT gemessenen SZE Spektrums messen wir Abweichungen der Form $T(z) = T_0(1+z)^{1-\alpha}$. Wir erklären, wie wir das Verhältnis des SZE Signals bei 95 und 150 GHz benutzen um die Temperatur der Hintergrundstrahlung zu bestimmen. Wir bestätigen das zuverlässige Funktionieren unserer Methode indem wir sie mit von einer neuen hydrodynamischen Simulation erzeugten Beobachtungen testen. Schließlich werten wir einen Katalog mit 158 von SPT selektierten Galaxienhaufen aus, und messen $\alpha = 0.017^{+0.030}_{-0.028}$, in übereinstimmung mit der Standardvorhersage $\alpha = 0$. In Verbindung mit weiteren veröffentlichten Ergebnissen erhalten wir $\alpha = 0.005 \pm 0.012$, was diese veröffentlichte Ergebnisse um $\sim 10\%$ verbessert. Des Weiteren messen wir die effektive Zustandsgleichung, welche in Modellen mit zerfallender dunkler Energie relevant ist, und finden $w_{\rm eff} = -0.994 \pm 0.010$.

Abstract

Galaxy clusters, the massive systems host hundreds of galaxies, are invaluable cosmological probes and astrophysical laboratories. Besides these fascinating galaxies, the concentration of dark matter creates a deep gravitational potential well, where even light passing by is bended and the background image is distorted. The baryonic gas falling into the potential well is heated up to more than 10^7 K that free electrons start to emitting in X-ray. Observing those phenomena leads to a throughout understanding of gravity, particle physics and hydrodynamics. In addition, residing on the top of the density perturbations, clusters are sensitive to the initial condition of the Universe, such that they are complimentary tools for cosmology studies.

In this thesis we first introduce the basic framework of the Universe and supporting observational evidence. Following that, we sketch the principle to use clusters for cosmology study via their redshift and mass distribution. However cluster mass is not a direct observable, so we need to estimate it by other channels. We briefly exhibit cluster observations in optical, X-ray and microwave bands and discuss the challenges in estimating the underlying cluster mass with them. After this introduction, we present our results on three aspects of the cluster cosmology study.

First, we present a study of *Planck* Sunyaev-Zel'dovich effect (SZE) selected galaxy cluster candidates using Panoramic Survey Telescope & Rapid Response System (Pan-STARRS) imaging data. To fulfil the strength of SZE survey, the redshifts of clusters are required. In this work we examine 237 *Planck* cluster candidates that have no redshift in the *Planck* source catalogue. Among them, we confirmed 60 galaxy clusters and measure their redshifts. For the remaining sample, 83 candidates are so heavily contaminated by stars due to their location near the Galactic plane that we do not identify galaxy members and assign reliable redshifts. For the rest 94 candidates we find no optical counterparts. By examining with 150 *Planck* confirmed clusters with spectroscopy redshifts, our redshift estimations have an accuracy of $\sigma_{z/(1+z)} \sim 0.022$. Scaling for the already published *Planck* sample, we expect the majority of the unconfirmed candidates to be noise fluctuations, except a few at high redshift that the Pan-STARRS1 (PS1) data are not sufficiently deep for confirmation. Thus we use the depth of the optical imaging for each candidate together with a model of the expected galaxy population for a massive cluster to estimate a redshift lower limit, beyond which we would not have expected to detect the optical counterpart.

Second, we use 95GHz, 150GHz, and 220GHz observations from South Pole Telescope (SPT) to study the SZE signatures of a sample of 46 X-ray selected groups and clusters drawn from $\sim$ 6 deg^2 of the *XMM-Newton* Blanco Cosmology Survey (XMM-BCS). The wide redshift range and low masses make this analysis complementary to previous studies. We develop an analysis tool that using X-ray luminosity as a mass proxy to extract selection-bias corrected constraints on the SZE significance- and $Y_{\rm sz}$-mass relations. The SZE significance-mass relation is in good agreement with an extrapolation of the relation obtained from high mass clusters. However, the fit to the $Y_{\rm sz}$-mass relation at low masses, while in agreement with the extrapolation from high mass SPT sample, is in tension at $2.8\,\sigma$ with the constraints from the *Planck* sample. We examine the tension with the *Planck* relation, discussing sample differences and biases that could contribute. We also analyse the radio galaxy point source population in this ensemble of X-ray selected systems. We find 18 of our systems have 1 GHz Sydney University Molonglo Sky Survey (SUMSS) sources within 2 arcmin of the X-ray centre, and three of these are also detected at significance > 4 by SPT. Among these three,

two are associated with the brightest cluster galaxies, and the third is a likely unassociated quasar candidate. We examined the impact of these point sources on our SZE scaling relation result and find no evidence of biases. We also examined the impact of dusty galaxies. By stacking the 220 GHz data, we found $2.8\,\sigma$ significant evidence of flux excess, which would correspond to an average underestimate of the SZE signal that is $(17 \pm 9)\,\%$ in this sample of low mass systems. Finally we predict a factor of four to five improvements on these SZE mass-observable relation constraints based on future data from SPTpol and XMM-XXL.

In the end we present a study using clusters as tools to probe deviations from adiabatic evolution of the Cosmic Microwave Background (CMB) temperature. The expected adiabatic evolution is a key prediction of standard cosmology. We measure the deviation of the form $T(z) = T_0(1+z)^{1-\alpha}$ using measurements of the spectrum of the SZE with SPT. We present a method using the ratio of the SZE signal measured at 95 and 150 GHz in the SPT data to constrain the temperature of the CMB. We validate that this approach provides unbiased results using mock observations of cluster from a new set of hydrodynamical simulations. Applying this method to a sample of 158 SPT-selected clusters, we measure $\alpha = 0.017^{+0.030}_{-0.028}$, consistent with the standard model prediction of $\alpha = 0$. Combining with other published results, we find $\alpha = 0.005 \pm 0.012$, an improvement of $\sim 10\%$ over published constraints. This measurement also provides a strong constraint on the effective equation of state, $w_{\rm eff} = -0.994 \pm 0.010$, which is presented in models of decaying dark energy.

Contents

Zusammenfassung vii

Abstract ix

Contents xii

List of Figures xiii

List of Tables xv

List of Acronyms xvii

1 Introduction 1
- 1.1 From Cosmology to Astrophysics . . . 1
  - 1.1.1 Foundations of Cosmology . . . 1
  - 1.1.2 Structure Formation . . . 5
  - 1.1.3 Cosmological Probes . . . 6
- 1.2 Galaxy Clusters and Cosmology . . . 8
  - 1.2.1 Cluster Masses . . . 9
  - 1.2.2 Cluster Distribution in Mass and Redshift Space . . . 10
  - 1.2.3 Cluster Observations . . . 11
  - 1.2.4 Biases in Scaling Relations . . . 14
- 1.3 Organization . . . 15

2 Optical Follow-up of Planck Cluster Candidates with PS1 17
- 2.1 Abstract . . . 17
- 2.2 Introduction . . . 18
- 2.3 Data Description . . . 20
  - 2.3.1 Planck SZE Source Catalogue . . . 20
  - 2.3.2 PAN-STARRS1 Data . . . 21
- 2.4 Method . . . 26
  - 2.4.1 Confirmation and Redshift Estimation . . . 26
  - 2.4.2 Redshift Lower Limits . . . 29
- 2.5 Results . . . 31
  - 2.5.1 Validation Using Confirmed Planck Clusters . . . 31
  - 2.5.2 Results from the Planck Candidates Sample . . . 33
- 2.6 Conclusions . . . 36

3 SZE-Mass Relations in Low Mass Clusters and Groups **39**
3.1 Abstract . . . 41
3.2 Introduction . . . 41
3.3 Data Description and Observables . . . 42
3.3.1 X-ray Catalog . . . 42
3.3.2 SPT Observations . . . 44
3.3.3 SPT-SZ Cluster Significance . . . 44
3.3.4 Integrated Y_{500} . . . 46
3.4 Method . . . 48
3.4.1 Description of the Method . . . 48
3.4.2 Validation with Mock Cluster Catalogs . . . 49
3.5 Results . . . 52
3.5.1 SPT Significance Extraction . . . 52
3.5.2 Testing the Null Hypothesis . . . 52
3.5.3 SPT ζ-mass Relation . . . 53
3.5.4 SZE Y_{500}-mass Relation . . . 57
3.5.5 Potential Systematics . . . 60
3.5.6 Point Source Population . . . 60
3.6 Conclusions . . . 62
3.7 Appendix . . . 64
3.7.1 Likelihood function . . . 64
3.7.2 XMM-BCS Cluster Sample . . . 67

4 Constraints on the CMB Temperature Evolution using Multi-Band Measurements of the Sunyaev Zel'dovich Effect with the South Pole Telescope **69**
4.1 Abstract . . . 70
4.2 Introduction . . . 71
4.3 Method . . . 72
4.4 Verification of Method with Simulations . . . 74
4.5 SPT Results . . . 75
4.5.1 Selection bias . . . 76
4.6 Conclusions . . . 78

5 Conclusions **81**
5.1 Summary of Results . . . 81
5.2 Beyond the Standard Model . . . 82

Bibliography **97**

Acknowledgements **99**

Curriculum Vitae **101**

List of scientific publications **103**

List of Figures

1.1 Possible thermal history of the Universe 4
1.2 Velocity-distance relation among extra-galactic nebulae 7
1.3 Colour-magnitude relation of galaxies 12
1.4 Illustration of thermal SZE 14
1.5 Illustration of selection biases 16

2.1 The sky distribution of *Planck* clusters and candidates within the PS1 region 19
2.2 The Y_{sz}–θ_{500} distribution of *Planck* clusters and candidates 22
2.3 Stellar locus scatter and repeatability of Pan-STARRS data 23
2.4 Example pseudo-colour image in the *g*ri bands of cluster candidate 218 24
2.5 The stellar loci in three different colour-colour spaces for the *Planck* cluster 307 25
2.6 The distributions of *griz* band 10σ depths (`mag_auto`) for PS1 fields around each *Planck* candidate 27
2.7 The observed number of red galaxies in the *Planck* confirmed cluster 442 at $z = 0.3436$ 29
2.8 Redshift limits for the *Planck* sample 31
2.9 Photo-z validation 33

3.1 The luminosity-redshift distribution of the XMM-BCS clusters from Šuhada et al. (2012) and the SPT-SZ clusters from Andersson et al. (2011) 45
3.2 Constraints on the ζ-mass relation from an analysis of the mock catalog . . . 51
3.3 BCS optical image of cluster 044 53
3.4 The measured significance ξ_X versus the expected SPT-SZ $\langle\zeta(L_X, z)\rangle$ from XMM-BCS sample 54
3.5 Constraints on the SPT ζ-mass relation parameters A_{SZ} and B_{SZ} for the non-point source sample (SPT-NPS) 56
3.6 Constraints on the Y_{500}-mass relation parameters A_Y and B_Y for the non-point source sample (SPT-NPS) 57
3.7 Comparison with the *Planck* $Y_{500} - L_X$ relation 59

4.1 Measurements of the temperature of the CMB as a function of redshift 77

List of Tables

2.1 Photo-z comparison for Rozo et al. (2014) sample 32
2.2 Sky positions and redshifts of *Planck* candidates 34
2.3 Unconfirmed Planck candidate 36

3.1 $L_{\rm X}$-mass relations with different luminosity bands 44
3.2 Constraints on the SPT zeta-mass relation parameters 55
3.3 Constraints on the Y_{500}-mass relation 58
3.4 SPT significance of the XMM-BCS sample 67

List of Notations

ACT Atacama Cosmology Telescope
AGN Active Galactic Nucleus
BAO Baryon Acoustic Oscillation
BCG Brightest Cluster Galaxy
BCS Blanco Cosmology Survey
BOSS Baryon Oscillation Spectroscopic Survey
BICEP Background Imaging of Cosmic Extragalactic Polarization
COBE Cosmic Background Explorer
CMB Cosmic Microwave Background
DES Dark Energy Survey
FWHM Full Width Half Maximum
GR General Relativity
H_0 Hubble constant
HOD Halo Occupation Distribution
HON Halo Occupation Number
ICM Intra-Cluster Medium
JWST James Webb Space Telescope
LSST Large Synoptic Survey Telescope
MCMC Monte Carlo Markov Chain
Ω_Λ energy density of dark energy at today over the critical density
Pan-STARRS Panoramic Survey Telescope & Rapid Response System
PS1 Pan-STARRS1
PSF Point Spread Function
photo-z photometric redshift
RASS *ROSAT* All Sky Survey
$\rho_{\rm crit}$ critical density of the universe
RS Red Sequence
RCS Red-Sequence Cluster Survey
RMS Root Mean Square
SDSS Sloan Digital Sky Survey
SNe Ia Type Ia supernovae
SNR Signal-to-Noise Ratio
SPT South Pole Telescope
SUMSS Sydney University Molonglo Sky Survey

SZ Sunyaev-Zel'dovich
SZE Sunyaev-Zel'dovich effect
tSZE thermal SZE
kSZE kinematic SZE
$T_{\rm CMB}$ CMB temperature
WISE Wide-field Infrared Survey Explorer
WMAP Wilkinson Microwave Anisotropy Probe
XMM-BCS *XMM-Newton* Blanco Cosmology Survey

Chapter 1

Introduction

> Darkness gives me a pair of black eyes,
> while I use them to look for brightness.
>
> Cheng Gu, Chinese poet

Similar to Charles Darwin's evolutionary theory on the development of life on Earth, the Big Bang theory provides the comprehensive understanding of the evolution of the Universe. But even with quantitative evidence on many different scales, challenges to our understanding remain: mysterious components of the Universe, i.e. dark matter and dark energy, have not yet been discovered in laboratories on the Earth; profound questions about the initial conditions before the Big Bang are still under debate (Guth, 1981; Efstathiou, 1995; Susskind, 2003); intriguing questions such as 'are there additional spacetime dimensions' and 'is a new theory of matter and light needed at the highest energies' must await answers until we achieve a more fundamental understanding of the Universe (Committee on the Physics of the Universe, 2003).

This thesis serves as a step toward answering those questions by studying the most massive collapsed systems in the Universe: galaxy clusters. In this chapter, we review the background of using galaxy clusters to understand the nature of the Universe and discuss the key observables required to enable that endeavor. In § 1.1 I briefly introduce the basic knowledge of our Universe and in § 1.2 I focus on an introduction to galaxy clusters. We conclude this chapter with an overview of the structure of this thesis in § 1.3.

1.1 From Cosmology to Astrophysics

In the following section we briefly summarise the basis of modern cosmology. In § 1.1.1, we specify the assumptions from which one can develop a model for the overall dynamics of the Universe. In § 1.1.2, we focus on deviations from the zero-order dynamics of the Universe, i.e. the structure formation. In § 1.1.3 we present results from multiple probes, linking the observational data with the theoretical predictions. We leave the discussion of galaxy clusters for the next section.

1.1.1 Foundations of Cosmology

Just two years after his magnificent presentation of General Relativity (GR), Einstein (1917) described the dynamics of the Universe based on two assumptions. The first one, soon recog-

nized as an axiom or principle in modern cosmology, states that the Universe is homogeneous and isotropic on large scales. It is called the cosmological principle and is still the foundation of most cosmological models. The second assumption was the presence of a cosmological constant, which Einstein adopted to offset the gravitational attraction and to create a static universe model that prevailed at that time. This assumption was soon falsified by observational evidence of an expanding universe by Hubble (1929). However, before the new Millennium, discoveries of an accelerating expansion of the Universe (Riess et al., 1998; Perlmutter et al., 1999) led to a revival of the cosmological constant. This work was recognized with the Nobel prize in 2011. In the following we describe the basic consequences derived from these two assumptions.

Friedmann (1922), Lemaître (1927), Robertson (1935) and Walker (1937) separately derived the general metric, $\mathrm{d}s^2$, of the space-time geometry under GR with the assumption of an isotropic and homogenous universe:

$$\mathrm{d}s^2 = c^2\mathrm{d}t^2 - a^2(t)\Big[\frac{\mathrm{d}r^2}{1-\kappa r^2} + r^2(\mathrm{d}\theta^2 + \sin^2\theta\mathrm{d}\phi^2)\Big], \tag{1.1}$$

where $a(t)$, the scale factor, describes the overall size of the universe, κ indicates the spatial curvature with values of $+1$, 0, or -1 corresponding to closed, flat, or open geometries, and (r, θ, ϕ) are the spherical coordinates.

The scale factor plays a central role in the cosmological coordinate as representing the ratio of physical length to comoving length. The comoving length is the distance between comoving coordinates, which is a grid expands at the same rate with the whole universe as sticked to it. This notation results that the comoving length is invariant under the expansion of the Universe.

The scale factor is also associated with an important observable, i.e. the cosmological redshift, which is an analogy of the Doppler effect in GR. A local observer receiving photons from distant sources sees frequency ν (wavelength $\lambda = c/\nu$) changing as:

$$\nu(t_{\mathrm{source}})/\nu(t_{\mathrm{obs}}) = \lambda(t_{\mathrm{obs}})/\lambda(t_{\mathrm{source}}) = a(t_{\mathrm{obs}})/a(t_{\mathrm{source}}). \tag{1.2}$$

The name, redshift, is from the fact that the Universe is expanding, and therefore the wavelength is increased relative to the one measured in the lab frame or rest frame of the source.

Typically, we set $a(t_{\mathrm{today}}) = 1$ and $a(t)$ is smaller than 1 given that we are in an expanding universe. Furthermore we define the redshift of a source as:

$$z \equiv \frac{\lambda(t_{\mathrm{obs}})}{\lambda(t_{\mathrm{source}})} - 1 = \frac{1}{a(t_{\mathrm{source}})} - 1. \tag{1.3}$$

With this equation, we link the measurable quantity, redshift, to the scale of the Universe at the time of the light was emitted relative to the scale today. However, diligence is needed for these conversions because the physical Doppler shift caused by the peculiar motion of celestial objects is indistinguishable from the cosmological redshifts.

Inserting the homogeneous and isotropic metric into the Einstein field equation

$$\mathcal{R}_{\mu\nu} - \frac{1}{2}g_{\mu\nu}\mathcal{R} = 8\pi G T_{\mu\nu} + \Lambda g_{\mu\nu}, \tag{1.4}$$

leads to two differential equations describing the time evolution of the scale factor:

$$\frac{\ddot{a}}{a} = -\frac{4}{3}\pi G(\rho + 3p) + \frac{\Lambda}{3}, \tag{1.5}$$

and

$$\left(\frac{\dot{a}}{a}\right)^2 = \frac{8\pi G\rho}{3} - \frac{\kappa}{a^2} + \frac{\Lambda}{3}, \tag{1.6}$$

where $\dot{a}$ denotes a time derivative, $\rho(t)$ is the mean mass-energy density ($c = 1$), $p(t)$ is the total pressure of the components of the mass-energy, and Λ is the cosmological constant. A simpler solution is available by using the fact that pressure is linked to mass-energy density by the equation of state for each component i:

$$w_i = p_i/\rho_i. \tag{1.7}$$

The typical value of w is 0 for non-relativistic matter and $-1/3$ for relativistic particles (i.e. photons). Moreover it is interesting that the cosmological constant can be treated as an energy term with $w = -1$. This is why the Λ term is also named as the dark energy with density of:

$$\rho_\Lambda = \Lambda/8\pi G. \tag{1.8}$$

Although the vacuum energy shares the same property as the cosmological constant-like dark energy, the vacuum energy has a measured and predicted density that is extremely small comparing to the cosmological constant. The nature of the dark energy is even more interesting.

With the above notation, we could simplify Equations (1.5) and (1.6), and rewrite the differential equation describing the time evolution of the expansion history of the universe. Important notation related to Equation (1.6) is:

$$H^2 \equiv \left(\frac{\dot{a}}{a}\right)^2 = \frac{8\pi G\sum_i \rho_i}{3} - \frac{\kappa}{a^2}, \tag{1.9}$$

where $H(t)$ is the Hubble parameter describing the expansion rate at time t and sometimes named as Hubble constant (H_0) at today. Note that the expansion rate is fully governed by the composition and geometry of the Universe. By measuring either side of the equation, we could gain more knowledge on the other side.

One useful application from Equation (1.9) is that if the total density equals

$$\rho_{\rm crit} \equiv \frac{3H^2}{8\pi G}, \tag{1.10}$$

at any time, it indicates the $\kappa = 0$ or, equivalently, that the geometry of the universe is flat. This special density is called the critical density of the universe ($\rho_{\rm crit}$).

Instead of deriving from Equations (1.5) and (1.6) together, we solve the Hubble parameter by using the conservation law of GR, $T^{\mu\nu}_{;v} = 0$:

$$\dot{\rho}_i = -3H(\rho_i + p_i). \tag{1.11}$$

And if each component is evolving independently, which is a reasonable assumption at later stages after the Big Bang, we could separately solve each component with Equation (1.7) as:

$$\rho_i \propto a^{-3(1+w_i)}. \tag{1.12}$$

Figure 1.1 shows a possible thermal history of the Universe. At late times in the Universe the matter and radiation evolve differently according to Equation (1.12). Although the Universe is dominated by dark energy at the present epoch, it has passed through previous phases of

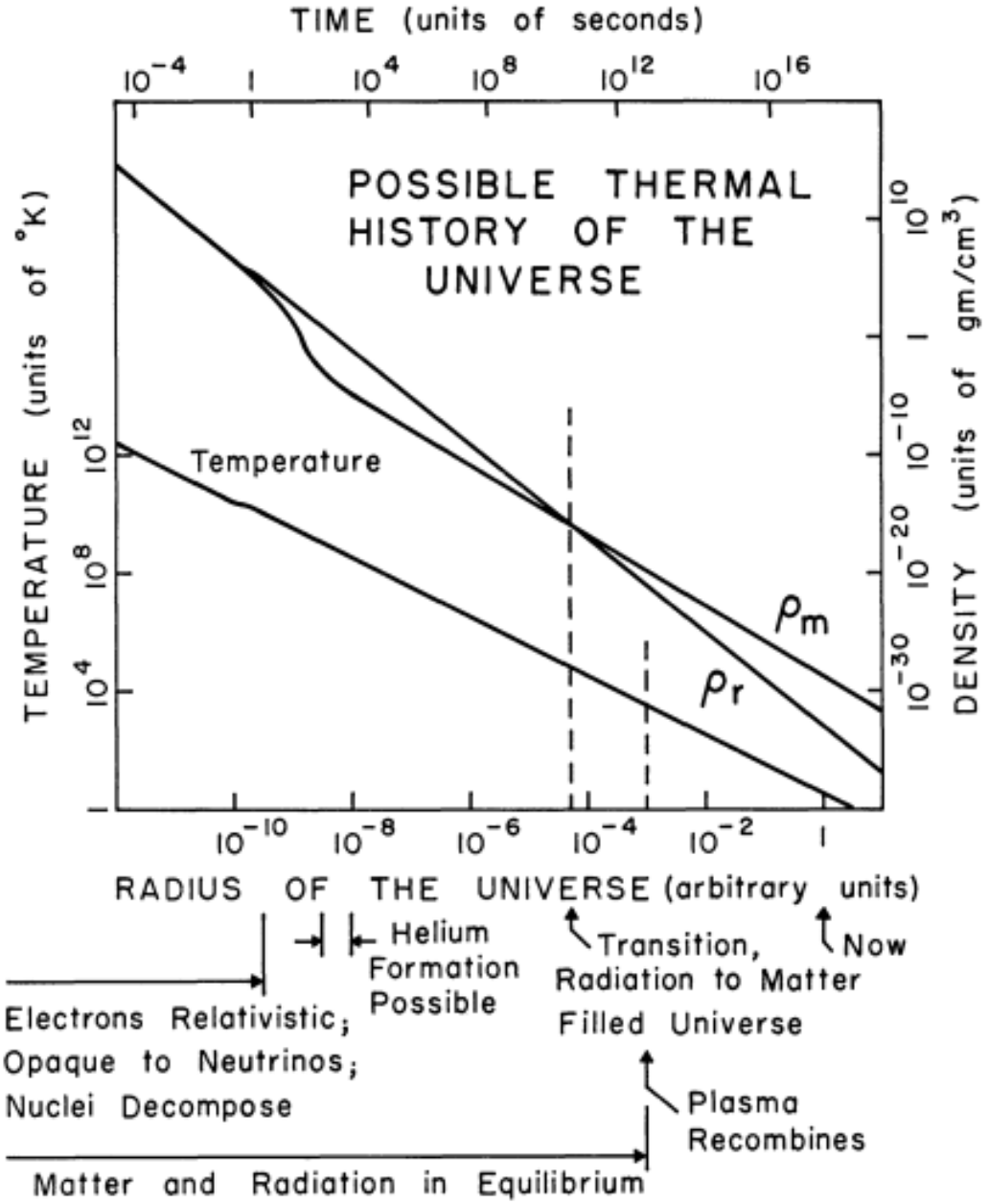

Figure 1.1: Possible thermal history of the Universe from Dicke et al. (1965). The x-axis shows the scale factor and is also linked to the time from the Big Bang. $\rho_{\rm m}$ and $\rho_{\rm r}$ lines show the density evolution of matter and radiation in the Universe. (Reproduced by permission of the AAS.)

matter domination and radiation domination. At a very early epoch (radius $\sim 10^{-9}$ smaller) the temperature was so high that all matter is relativistic, and the evolution of the Universe becomes particularly simple.

By defining the dimensionless density of each component as $\Omega_i(z) \equiv \rho_i(z)/\rho_{\rm crit}(z)$, where i can be either geometry (κ), matter (M), radiation (γ), or cosmological constant (Λ), we can express the Hubble parameter as a function of redshift as:

$$H(z) = H_0\sqrt{\Omega_\gamma(0)(1+z)^4 + \Omega_{\rm M}(0)(1+z)^3 + \Omega_\kappa(1+z)^2 + \Omega_\Lambda(0)}. \tag{1.13}$$

So far we have derived the expansion history of the Universe as a whole. As shown in Equation (1.13) the expansion history $H(z)$ of the Universe is determined by the composition of the Universe and the evolution of each of those components as the Universe expands. Thus, a measure of the expansion history provides a direct constraint on the composition of the Universe and allows one to test how the energy density of components such as the dark energy evolve with time.

1.1.2 Structure Formation

In this section, we introduce the formation of structures from the initial fluctuations in the density field. Deviating from the global evolution of the Universe, the positive density perturbations separate from the expansion and seed the structures we see today. Because models of inflation suggest that the density fluctuations are Gaussian distributed with random phase, these perturbations are typically described by a power spectrum:

$$P(k) \equiv < |\delta_k|^2 >, \tag{1.14}$$

where δ_k is the Fourier component of the spatial density contrast $\delta(x) \equiv \frac{\rho(x)-\langle\rho\rangle}{\langle\rho\rangle}$. If perturbations can be described as a Gaussian random field, then the power spectrum contains a complete statistical description of them.

In the limit where the perturbations are very small (the linear regime), the growth function is commonly used (c.f. Voit, 2005, and reference therein):

$$D(a) \propto \frac{\delta\rho}{\rho} \propto \frac{\dot{a}}{a}\int_0^a \frac{{\rm d}a}{\dot{a}^3} \tag{1.15}$$

with the normalisation of 1 at today, i.e. $D(z=0) = 1$. This equation shows that the amplitude of fluctuations is linked to the overall expansion history of the Universe.

Various processes alter the linear perturbation development and leave different signatures imprinted on the power spectrum of density perturbations. In the early Universe, during the radiation-dominated era (see Figure 1.1), the perturbation growth is halted at scales smaller than the Hubble length. Furthermore, the photon baryon fluid damps the perturbation modes as photons diffuse out of higher-density regions. Later in the matter dominated era, the perturbations resume growth And the streaming and pressure of matter components can further damp small-scale perturbations. Each effect imprints on the $P(k)$, thus the measurements of power spectrum at different scales and redshifts lead to an understanding of the composition of the Universe and the processes that were at play during the evolution of density perturbations.

1.1.3 Cosmological Probes

In this section, I link the theoretical prediction from previous sections to astronomical observations. Those supportive observations are introduced from the smallest scale, atomic level, to the giant structures spanning several million light-years to emphasize the success of the modern cosmology theory.

Hot Plasma

Even though an expanding universe model was accepted after Hubble's observations, the implications for a hot early epoch or for the Big Bang theory were realised only later. Definitive evidence was obtained only after 30 years. The measurement by Penzias & Wilson (1965) of an isotropic excess antenna temperature was crucial and its likely cosmological origin was clearly explained (Dicke et al., 1965).

In the discovery, they found a 3.5 K excess of radiation, which could not be explained by any known sources. Later this value was measured to be 2.725 K (Fixsen et al., 1996), which corresponds to a mass density of $\rho_\gamma \sim 5 \times 10^{-31}$kg m^{-3}. In comparison, the critical density of the Universe is about 1×10^{-26}kg m^{-3}. The radiation density is a tiny fraction of the energy density in the Universe today. But as shown in Figure 1.1, in the early Universe the radiation is the dominant component; it's energy density scales as $(1+z)^4$ (c.f. Equation (1.12)), where matter component scales as $(1+z)^3$. Both relations indicates that the early Universe is much denser, and the earlier expression relating the redshift and radiation wavelength indicates that at early epochs the temperature of the black body radiation was also very high..

In such a hot and dense environment, electrons are ionised from atoms, and the radiation and matter are coupled through electron scattering and are in thermal equilibrium. When the temperature drops to about 3000 K as Universe expands, matter becomes neutral and the Universe becomes transparent to the photons that decouple from the matter and cosmic radiation background. As a consequence of the expansion of the Universe, the radiation dilutes and forms the Cosmic Microwave Background (CMB) today.

The CMB radiation is originated from the Big Bang but has decoupled from matter with a mean-free-path longer than the size of the Universe such that it is isotropic and matches a black body spectrum. Indeed, the spectral properties observed by the Cosmic Background Explorer (COBE) match such a spectrum and provide strong limits on non-thermal energy transfer to the radiation field.

Besides the uniformity of the CMB, it also encodes rich information by its anisotropy. As introduced in § 1.1.2, the perturbations are sensitive to the underlying composition of the Universe. Once CMB photons decouple from the matter, they rarely interact before reaching us. They encode some of the earliest information we can obtain about the Universe so far. So, by observing the CMB anisotropy, we probe the perturbations at and early phase in the Universe and are able, in principle, to study the initial conditions and composition of the Universe.

The discovery of the CMB anisotropy was established by COBE (Wright et al., 1992) at an angular resolution of 7°. The field evolves quickly with better resolution and sensitivity. The recent result from satellites Wilkinson Microwave Anisotropy Probe (WMAP) and *Planck*, along with ground-based experiments such as SPT and Background Imaging of Cosmic Extragalactic Polarization (BICEP) are tightening the cosmological constraints.

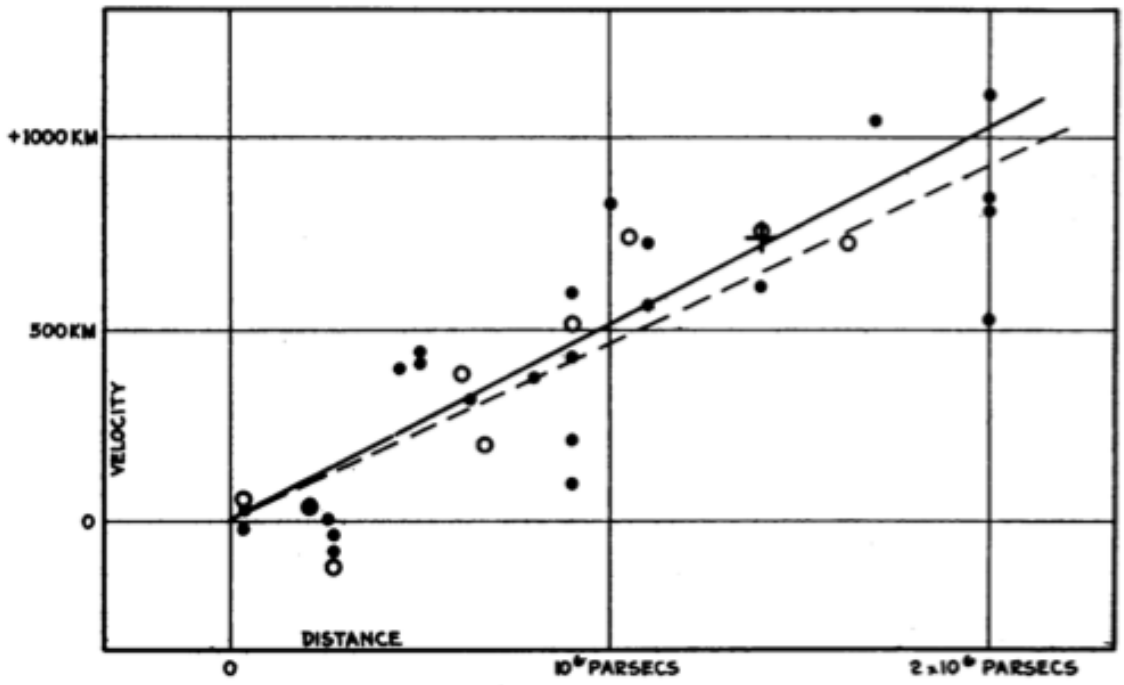

Figure 1.2: Velocity-distance relation among extra-galactic nebulae (reproduced from Hubble, 1929).

Stars

The bright celestial objects served as the only channel for people to learn about the Universe for thousands of years. They also played an important role in the development of the modern cosmology.

Photon travels along the null geodesics, thus the distance traveled to an observer at time t_0 from their source is simply:

$$D_{\rm C} = \int_{t_e}^{t_0} \frac{c{\rm d}t}{a(t)}. \tag{1.16}$$

Because photons are further dimmed by the expansion of the Universe (c.f. Equation (1.3)), the relation between the absolute luminosity (L) from the emitting source and the apparent luminosity (l) one observes iss:

$$L = l \times 4\pi[(1+z)D_{\rm C}]^2. \tag{1.17}$$

Therefore by observing objects with known absolute luminosity, we could measure the distances to those objects. With their redshift obtained via spectroscopic features, we could then study the expansion history of the Universe and its composition. By assuming the brightest stars in distant galaxies have the same intrinsic luminosity, Hubble (1929) measured distances of nearby galaxies versus their redshifts and presented evidence of an expanding Universe.

Besides the pioneer work of revealing the expanding nature of the Universe, his method of using standard candles became a useful tool in cosmological study. And finding objects with knowns luminosities is the crucial step for this method.

Certain types of supernovae, the magnificent explosion of dying stars, are found to be standard candles. Especially Type Ia supernovae (SNe Ia), where a white dwarf in a binary system accretes matter pushing its mass over the Chandrasekhar limit, present a tight relation between their peak brightness and fading time (Phillips, 1993). In addition their peak luminosities are so bright that they out-shine their host galaxies and are observable over cosmological distance scales.

Two teams, the Supernova Cosmology Project and the High-z Supernova Search Team, used these SNIa distance measurements to find an astonishing result that the expansion of the Universe is accelerating Perlmutter et al. (1999); Riess et al. (1998). This result clearly supported a dark energy-like component as the energy source required to change of the expansion rate. However, the nature of dark energy is still under debate.

Galaxies

Similar to the standard candle method, standard rulers can also be used as a cosmological probe. One of them is the characteristic scale in the galaxy distribution that results from Baryon Acoustic Oscillation (BAO). Sharing the same origin with the CMB anisotropy, the BAO is an outcome from the oscillation of matter and radiation in the early universe and features a scale of 150 Mpc (Peebles & Yu, 1970). This large size protects the BAO feature from the complex physics of galaxy formation, and therefore it would be used as a standard ruler to measure cosmological distances.

However, the BAO feature is weak and can only be observed with very large samples. This requires surveying the large scale matter distribution in the Universe. Galaxy surveys like the 6dFGS (Beutler et al., 2011), the Sloan Digital Sky Survey (SDSS) (Padmanabhan et al., 2012), the Baryon Oscillation Spectroscopic Survey (BOSS) (Anderson et al., 2012), and the WiggleZ survey (Blake et al., 2011) are providing complementary cosmological constraints to the CMB and the SNe Ia data.

Galaxy Clusters

In previous sections we explored the tools to study cosmological models using light created and thermalised at atomic scales as well as that emitted by exploding stars and galaxies. However, we are only utilising baryonic component, which occupies only 4 per cent of the total composition of the Universe (Hinshaw et al., 2013). Galaxy clusters, the most massive, collapsing systems in the Universe are dominated by dark matter and provide us a complementary channel for cosmology research. Located at the peaks of density perturbations, they are extremely sensitive to the underlying cosmological model; meanwhile, the deep gravitational potential wells heat the gas to several keV, accelerate galaxies to velocities of 1000 km/s, and alter the direction of propagating light. Moreover, energetic merging events in clusters also provide rich information for astrophysical studies. In the following section, I review the important aspects of galaxy clusters for cosmology study.

1.2 Galaxy Clusters and Cosmology

We first introduce the formation of a galaxy cluster and define its mass in § 1.2.1. Then we briefly link the mass to cosmology applications in § 1.2.2. We further discuss the observational

aspects of galaxy clusters in § 1.2.3 and conclude with a discussion of biases present in observed mass-observable relations due to selection effects in § 1.2.4.

1.2.1 Cluster Masses

Cluster are formed via a hierarchical process from tiny initial density perturbations. Small clumps of matter are the first pieces deviating from the Hubble flow to form stars and galaxies as the power spectrum of density perturbation has larger amplitudes at small scales. Progressively, these small objects merge and relax within larger scales. And at the top of this hierarchy galaxy clusters are currently the largest structures undergoing virialization.

The description of cluster formation is presented in terms of a spherically symmetric collapse model (Gunn & Gott, 1972). A slightly higher density region originating from the density perturbation decouples from the initial expansion of the rest of the Universe. Gradually, the expansion of the overdense region halts and reverses by its own gravity. In a perfectly spherically symmetric case, each shell of mass moves according to:

$$\frac{\mathrm{d}^2 r_{\rm sh}}{\mathrm{d}t^2} = -\frac{4\pi G}{r_{\rm sh}^2}\sum_i (1+3w_i)\int_0^{r_{\rm sh}} \rho_i r^2 \mathrm{d}r, \tag{1.18}$$

where $r_{\rm sh}$ is the distance of the mass shell to the center of mass and i represents matter, radiation, and dark energy with the equations of state, w_i, respectively. Because at the early formation stage of clusters, the pressure term is negligible compared to the gravitational pull from the matter, we can solve this differential equation without cosmology parameters present. One characteristic length is the turnaround radius, at which a cluster stops expansion and reverses to collapse:

$$r_{\rm ta} = \Big(\frac{2GM_{\rm sh}t_c^2}{\pi^2}\Big)^{1/3}, \tag{1.19}$$

where $M_{\rm sh}$ is the mass inside the shell and t_c is the time for a shell that collapses to the center.

A further simplification to a constant density profile leads to the common spherical top-hat model, which suggests each shell collapses with the same speed and thus there no shells pass through one another. By applying the virial theorem, the cluster will be relaxed with radius of half $r_{\rm ta}$. This implies a density of $6M_{\rm sh}/\pi r_{\rm ta}^3$. With equation (1.19), the density can be expressed in terms of the critical density as $8\pi^2\rho_{\rm crit}/(Ht)^2$. For a matter-dominated universe ($\Omega_M = 1$), we know from equation (1.13) that $a \propto t^{2/3}$ such that $Ht = 2/3$. Thus, at collapse the structure exhibits a constant overdensity of $\Delta_{\rm vir} = 18\pi^2$ with respect to $\rho_{\rm crit}$. In more realistic universe this value has to be changed according to the cosmological parameters, which effect the density evolution. Bryan & Norman (1998) has provided a useful approximation of $\Delta_{\rm vir}$ for a flat universe with cosmological constant as:

$$\Delta_{\rm vir} = 18\pi^2 + 82[\Omega_{\rm M}(z) - 1] - 39[\Omega_{\rm M}(z) - 1]^2. \tag{1.20}$$

In addition to this theoretical approach of deriving the density contrast Δ_v of a collapsed object, other alternative definitions are inspired by observations and simulations. One choice is to use the mean matter density $\rho_m = \Omega_M(z)\rho_{\rm crit}$. This is preferred by simulation studies but not by observations, because it requires a prior knowledge of the cosmological parameter, $\Omega_{\rm M}$. The second choice is the threshold of density contrast. $\Delta = 200$ is popular because it is approximately the same as the theoretical value in Equation (1.20). Whereas $\Delta = 500$ is also

widely used because the higher density contrast corresponds to a cluster region that is more easily detectable and because simulations show that this inner region of clusters tends to be more relaxed than the outer parts within virial radius.

1.2.2 Cluster Distribution in Mass and Redshift Space

As the most massive collapsed objects in the universe, the clusters are forming at the maxima of the density field, and their distribution in mass and redshift is extremely sensitive to the structure growth rate and clustering matter density in the Universe. Thus clusters provide a power constraint on cosmological models. This demographics study of clusters is commonly focusing on the mass function, which describes the number density of clusters with certain mass ranges at different redshifts.

A cluster is born in a dark matter halo, which is formed from a region where the density perturbation overdensity has an amplitude that surpasses a critical value (δ_c). In particular, the number density of collapsed halos, the mass function, can be expressed in as:

$$n(M,z) = \frac{\Omega_{\rm M}\rho_{\rm crit}}{M}\mathrm{erfc}\Big[\frac{\delta_c}{\sqrt{2}\sigma(M,z)}\Big], \tag{1.21}$$

where the variance of the density fluctuations σ^2 on a mass scale M is extracted using a top-hat window function $W_k(x) = 3(\sin x - x\cos x)/x^3$:

$$\sigma^2(M,z) = (\frac{1}{2\pi})^3 \int P(k,z)|W_k(kR)|^2 \mathrm{d}^3k \tag{1.22}$$

within radius $R = (3M/4\pi\rho_{\rm crit})^{1/3}$ that corresponds to the radius of a sphere whose enclosed mass would be M. The $\sigma^2(M,z)$ represents the variance at mass scale M and redshift z. The first factor in Equation (1.21) calculates the characteristic density of objects of mass M in the Universe, and the second factor corresponds to the fraction of the Gaussian distribution that exceeds the critical overdensity threshold (Press & Schechter, 1974). With this expression we can relate the cluster mass function to different characteristics of the Universe such as the matter density and the growth rate of density perturbations.

As observational study works with the differential form of the mass function, which is commonly written as:

$$\frac{\mathrm{d}n}{\mathrm{d}\ln M} = \sqrt{\frac{2}{\pi}}\frac{\Omega_{\rm M}\rho_{\rm crit}}{M}\frac{\delta_c}{\sigma}\exp(-\sigma_c^2/2\sigma^2). \tag{1.23}$$

This equation clearly shows that the mass function drops exponentially at the massive end. So the presence of massive clusters in the Universe provides a powerful constraint on cosmological models.

Theoretical studies continue to improve the detail of the formula by incorporating more realistic aspects of structural formation. Sheth & Tormen (1999) introduce ellipsoidal collapse to replace the spherical model. Other studies have advanced using an excursion set approach to resolve difficulties with the peak statistics approach (Lacey & Cole, 1993). In addition, simulation studies enable a numerical approach with empirical fitting formulae adopted in Tinker et al. (2008); Watson et al. (2013):

$$\frac{\mathrm{d}n}{\mathrm{d}\ln M} = \frac{\rho_{\rm crit}}{M}f(\sigma)\Big|\frac{\mathrm{d}\ln\sigma}{\mathrm{d}\ln M}\Big|, \tag{1.24}$$

at each redshift.

The above-mentioned mass function formulae constructively link the cluster number density to the underlying density perturbation. However the cluster mass is not a direct observable. Observers always need to find a proxy for mass estimation. In the following section we describe some of these approaches.

1.2.3 Cluster Observations

To use the mass function to interpret observations, an estimation of the cluster masses is required. In the following we present cluster observables and discuss their advantages and weaknesses.

Optical

As the name suggests, the galaxy cluster is a concentration of galaxies on the sky, which was discovered at the end of the eighteenth century by Charles Messier and William Herschel. Systematic studies and catalogs were undertaken by George Abell and collaborators, who grouped the galaxies within a ~ 1.5 Mpc bounding radius. This method is still the basis of many optical cluster finding algorithms (Postman et al., 1996; Olsen et al., 1999). To overcome the difficulties of projection of non-cluster galaxies, Gladders & Yee (2000) proposed a new cluster search technique that focuses on early type galaxies, which lie along a restricted space in colour versus magnitude, known as the Red Sequence (RS). Leaning on the advance of large sky surveys, Gladders & Yee (2005) and following efforts (Koester et al., 2007; Hao et al., 2010; Rykoff et al., 2014) have successfully compiled the largest cluster catalogs to date.

In addition to the efficiency of cluster searching, the optical data also provide useful insights into cluster properties. The first relevant information is the cluster mass. As expected that the total number of galaxies or the total luminosity of a cluster is correlated with the cluster mass although they exhibit large scatters (Lin et al., 2004; Gladders et al., 2007; Song et al., 2012a). However, in a recent study Rozo & Rykoff (2014) show that an mass estimator built upon the observed RS galaxies achieves a mass scatter of $\approx 25\%$, which is comparable to other methods. Besides tracing the luminous components, gravitational lensing studies (Hoekstra, 2007; von der Linden et al., 2014) trace the distortion of background galaxies caused by the gravity of galaxy clusters, enabling a direct probe of the cluster mass.

Additional information provided by optical data is the redshift of the cluster, which is crucial for many astrophysical applications. Given the rapid growth in cluster samples, the more accurate spectroscopic redshift measurement is often too costly. Based on the same RS technique, Song et al. (2012b) estimate redshifts for cluster samples selected from a 720 square degree South Pole Telescope Sunyaev-Zel'dovich survey (SPT-SZ) catalog to support further cosmological study (Reichardt et al., 2013).

Galaxies consist of stars. In the case of passively evolving stellar populations, there is a distinct break around 4000 Å. By comparing the difference of the luminosities on the two sides of the break, we can estimate the redshift. Furthermore those galaxies from the same redshift present a linear relation in the colour-magnitude plot as shown in Figure 1.3. Then the cluster redshift is measured by comparing observed cluster galaxies with theoretically computed RS position. We apply this technique later in Chapter 2.

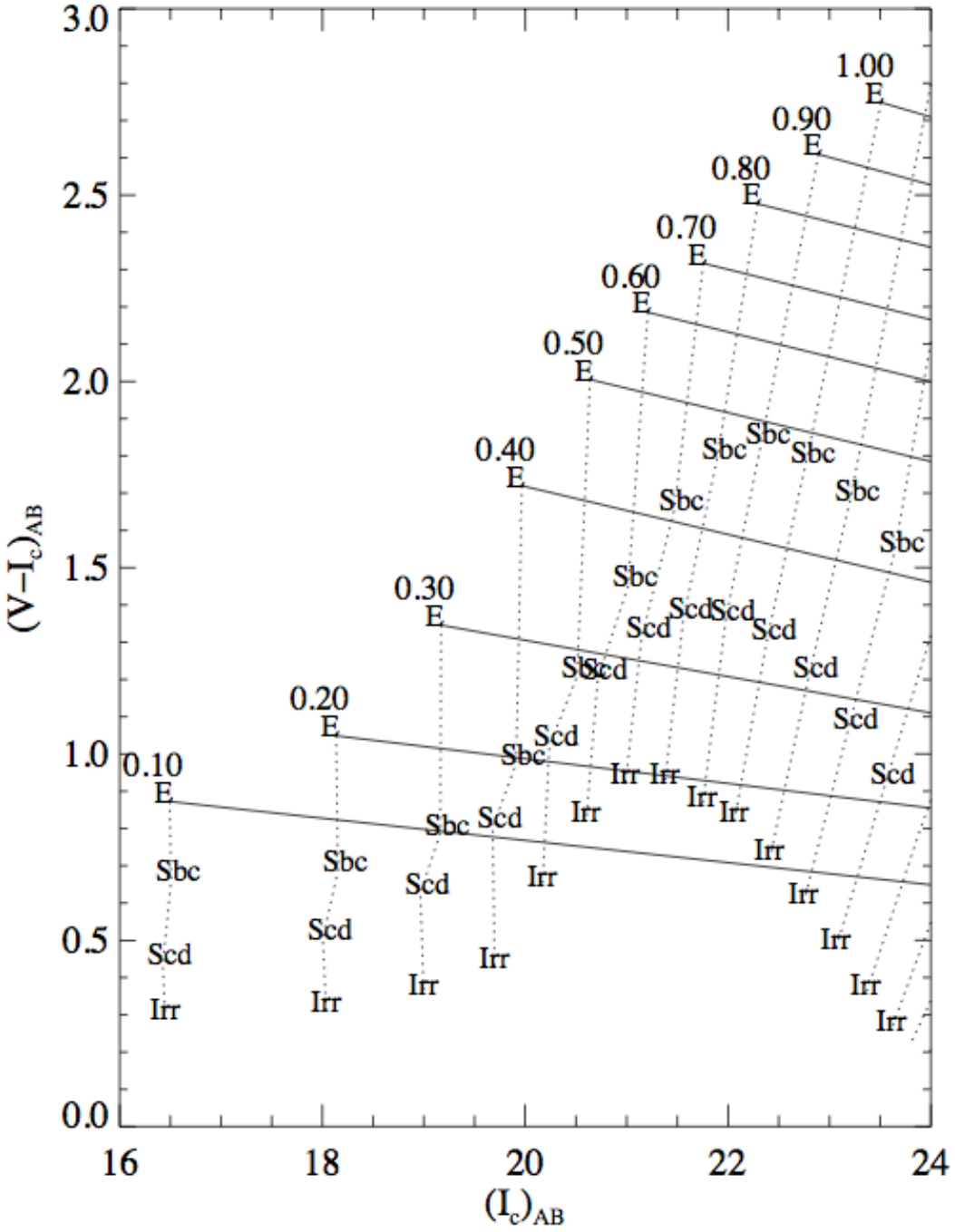

Figure 1.3: Colour-magnitude relation of galaxies from Gladders & Yee (2000). Each solid line represents the expected RS of early type galaxies in V–I bands at the associated redshift. The locations of galaxies of other types are shown with dotted lines extending blueward of the RS at each redshift. (Reproduced by permission of the AAS.)

X-ray

The deep gravitational potential of galaxy cluster heats up the in-falling gas into high temperature ($\sim$keV) such that the majority of the baryonic matter emits in X-ray (see Sarazin, 1988, for detailed discussion). Moreover, the X-ray luminosity correlates with the cluster mass. Typically the radiation is dominated by the bremsstrahlung radiation, and the emissivity is therefore proportional to the square of the gas density times the temperature. Detailed studies of X-ray profiles can be carried out to estimate the cluster hydrostatic masses, but these masses are only as accurate as the assumption of hydrostatic equilibrium. And X-ray luminosity ($L_{\rm X}$), temperature ($T_{\rm X}$), gas mass ($m_{\rm g}$) or the combination $Y_{\rm X} = T_{\rm X} m_{\rm g}$ are used as proxies for cluster mass.

Microwave

Soon after the discovery of CMB radiation, Weymann (1966) proposed that Compton scattering would distort the initial blackbody spectrum of the CMB and Sunyaev & Zel'dovich (1970, 1972) predicted that the intergalactic hot gas of galaxy clusters would produce such a distortion, now named as the Sunyaev-Zel'dovich effect (SZE).

With the advance of bolometer technologies, the SZE studies have shifted from the follow up of previously known clusters (e.g. Benson et al., 2004) to surveys for completely new systems (e.g. Staniszewski et al., 2009). Ongoing projects like *Planck*, SPT, and Atacama Cosmology Telescope (ACT) have provided hundreds of newly discovered clusters and yielded cosmological constraints based on clusters. Here I briefly review the basis of the SZE and reveal its advantages in cosmological studies.

The thermal SZE (tSZE) is proportional to the integrated electron pressure along the line of sight:

$$y(\boldsymbol{\theta}) = \frac{\sigma_{\rm T}}{m_{\rm e}c^2} \int P_{\rm e}(\boldsymbol{\theta}, l) dl, \tag{1.25}$$

where $\sigma_{\rm T}$ is the Thompson scattering cross section, and $P_{\rm e}$ denotes the electron pressure. And this results in a spectrum shift of the CMB temperature ($T_{\rm CMB}$) at the position of the cluster ($\boldsymbol{\theta}$) on the sky:

$$\frac{\Delta T_{\rm CMB}}{T_{\rm CMB}} = y(\boldsymbol{\theta}) g(x), \tag{1.26}$$

where $g(x) = x\coth(x/2) - 4$ and $x \equiv h\nu / kT_{\rm CMB}$ is the equivalent frequency[1] (Carlstrom et al., 2002). So by measuring the temperature distortion, we directly estimate the projected electron pressure of a cluster, which provides a good mass proxy for the cluster. Also, because the SZE is a distortion of the CMB radiation, the signature does not suffer from cosmological dimming. Thus, it is an extremely useful tool for studying cluster samples that span a wide range of redshift.

However the CMB itself exhibits temperature fluctuations, and these contaminate the SZE signature in the CMB temperature maps. To reduce the noises, a matched-filter technique is applied (Melin et al., 2005, 2006) that uses the distinct angular scaling of clusters and the frequency-dependent distortion ($g(x)$ in Equation (1.26) and see Figure 1.4):

$$\boldsymbol{\Phi}(\boldsymbol{k}) = \frac{1}{\sigma_f^2} \boldsymbol{P}^{-1}(\boldsymbol{k}) \cdot \boldsymbol{g_x} T(\boldsymbol{k}), \tag{1.27}$$

[1] The h denotes the Planck constant here.

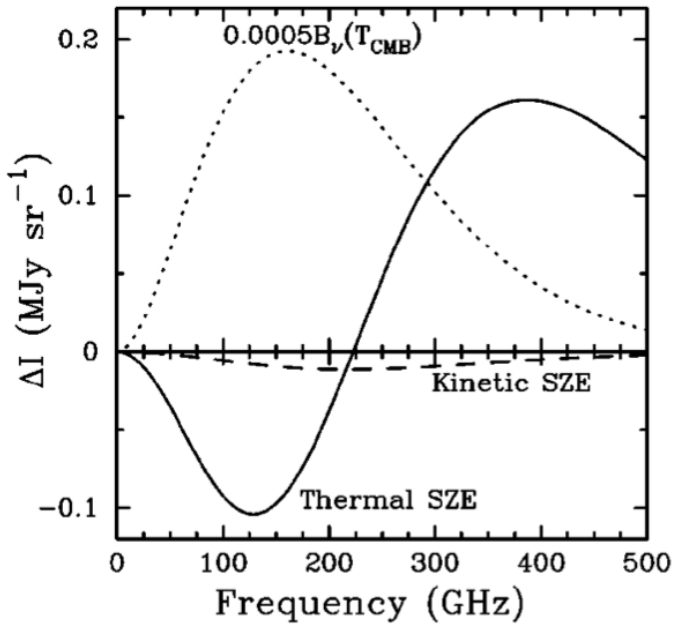

Figure 1.4: Illustration of the tSZE from Carlstrom et al. (2002). The solid line indicates the strength of tSZE at different frequencies for a typical cluster with temperature of 10 keV. The dotted line indicates the CMB radiation strength scaled by 0.0005. The dashed line indicates the kinematic SZE, which is caused by non-zero cluster velocity with respect to the CMB reference frame. (Reproduced with permission of Annual Reviews of Astronomy and Astrophysics.)

where $\boldsymbol{g_x}$ is a vector of $g(x)$ at observational frequencies, $T(\boldsymbol{k})$ is the Fourier transformation of the cluster SZE template, $\boldsymbol{P}$ is the noise power spectrum matrix, and σ_f is the normalisation factor

$$\sigma_f^2 \equiv \int \mathrm{d}^2\boldsymbol{k}[\boldsymbol{g_x}T(\boldsymbol{k})]^t \cdot P^{-1}(\boldsymbol{k}) \cdot [\boldsymbol{g_x}T(\boldsymbol{k})]. \tag{1.28}$$

In addition, it also models the Root Mean Square (RMS) of the filtered map.

For a multi-frequency map set $\boldsymbol{M}$ and a cluster SZE profile $y(\boldsymbol{\theta}) = y_0 T(\boldsymbol{\theta})$, we have the best estimation of y_0 as:

$$\hat{y}_0(\boldsymbol{\theta}_0) = \int \mathrm{d}^2\boldsymbol{\theta}\Phi^t(\boldsymbol{\theta} - \boldsymbol{\theta}_0) \cdot \boldsymbol{M}(\boldsymbol{\theta}). \tag{1.29}$$

Also y_0/σ_f servers as the Signal-to-Noise Ratio (SNR) of a cluster that matches the template T at position $\boldsymbol{\theta}_0$. And combining with the template, the physical quantities such as the integrated Y_{SZE} within a given radius can be estimated. Both the SNR and Y_{SZE} are used as the mass proxy for clusters.

1.2.4 Biases in Scaling Relations

Each mass proxy introduced above must be calibrated to the cluster mass, and accounting for biases is important in this process. The dynamical state of clusters is a source of scatter

in these relations. The projection of mass along the line-of-sight can bias the lensing signal. However beyond those physically motivated biases, there are other biases related to the selection of the cluster sample. Here we briefly introduce the Eddington bias and the Malmquist bias.

Mantz et al. (2010a) depict those two biases with the sketch in Figure 1.5. The Malmquist bias is purely due to the selection of a cluster sample by an observable instead of the mass. When the observable associated with the mass has scatter (and every known mass proxy does have scatter), a selection based on the observable will cut off the systems scattered lower but keep those scattered higher. So we artificially boost the mass–observable relation at low mass end.

In addition to that, the cluster masses are distributed according to the mass function (Equation (1.24)). So there are more clusters with low mass than high mass. As shown in the bottom-right panel of Figure 1.5, there are more low mass systems observed than the case where cluster masses are uniformly distributed (top-right panel). Both the Malmquist and Eddington biases must be accounted for when calibrating mass–observable relations. In Chapter 3 we will continue the discussion and present our analysis approach to calibrate the scaling relation with selection biases..

1.3 Organization

This thesis is organised as follows. In Chapter 2 we present the result of using red sequence galaxies to measure the redshifts of *Planck* cluster candidates within the Pan-STARRS footprint. In Chapter 3 we study the Sunyaev-Zel'dovich effect signatures of X-ray selected low mass clusters and groups with SPT data. In Chapter 4 we explore the adiabatic evolution of the CMB temperature by using SPT selected clusters.

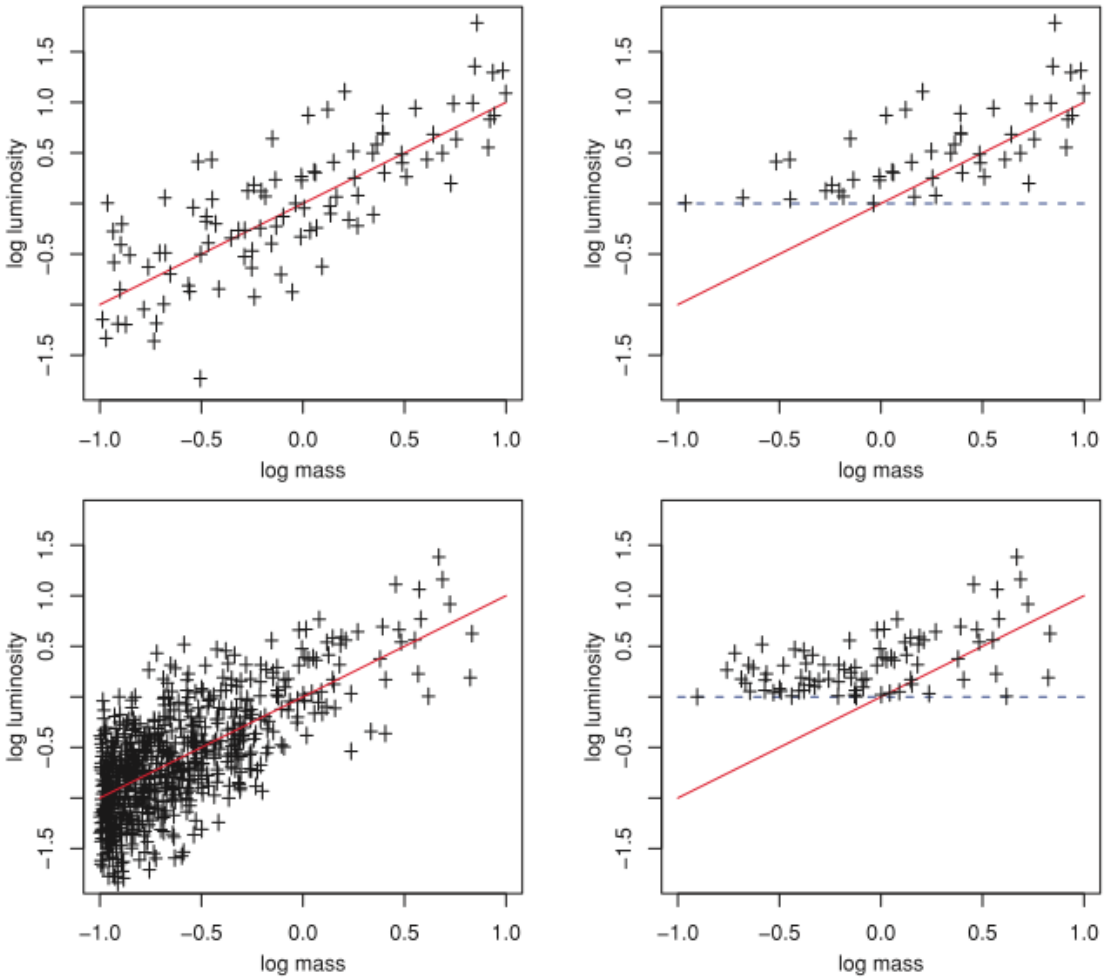

Figure 1.5: Illustration of selection biases reproduced from Fig. A1 in Mantz et al. (2010a). The top-left panel shows a uniformly distributed sample without selection. The top-right panel shows that a simple fit to the selected data will deviate from the true relation (red line). The bottom-left panel shows the case, where the sample is distributed according to the cluster mass function. And the bottom-right panel shows that after the selection, a simple fit is further biased due to the sample distribution.

Chapter 2

Optical Confirmation and Redshift Estimation of the Planck Cluster Candidates overlapping the Pan-STARRS Survey

J. Liu[1,2], C. Hennig[1,2], S. Desai[1,2], B. Hoyle[1], J. Koppenhoefer[3,1], J. J. Mohr[1,2,3], K. Paech[1], W. S. Burgett[4], K. C. Chambers[4], S. Cole[5], P. W. Draper[5], N. Kaiser[4], N. Metcalfe[5], J. S. Morgan[4], P. A. Price[7], C. W. Stubbs[6], J. L. Tonry[4], R. J. Wainscoat[4], C. Waters[4]
[1]Department of Physics, Ludwig-Maximilians-Universität, Scheinerstr. 1, 81679 München, Germany
[2]Excellence Cluster Universe, Boltzmannstr. 2, 85748 Garching, Germany
[3]Max-Planck-Institut für extraterrestrische Physik, Giessenbachstr. 85748 Garching, Germany [4]Institute for Astronomy, University of Hawaii at Manoa, Honolulu, HI 96822, USA
[5]Department of Physics, Durham University, South Road, Durham DH1 3LE, UK
[6]Department of Physics, Harvard University, Cambridge, MA 02138, USA
[7]Department of Astrophysical Sciences, Princeton University, Princeton, NJ 08544, USA

This chapter is submitted to MNRAS.

2.1 Abstract

We report results of a study of *Planck* Sunyaev-Zel'dovich effect (SZE) selected galaxy cluster candidates using the Panoramic Survey Telescope & Rapid Response System (Pan-STARRS) imaging data. We first examine 150 *Planck* confirmed galaxy clusters with spectroscopic redshifts to test our algorithm for identifying optical counterparts and measuring their redshifts; our redshifts have a typical accuracy of $\sigma_{z/(1+z)} \sim 0.022$ for this sample. We then examine an additional 237 *Planck* galaxy cluster candidates that have no redshift in the source catalogue. Of these 237 unconfirmed cluster candidates we are able to confirm 60 galaxy clusters and measure their redshifts. A further 83 candidates are so heavily contaminated by stars due to their location near the Galactic plane that we do not attempt to identify counterparts. For the remaining 94 candidates we find no optical counterpart but use the depth of the Pan-STARRS1 data to estimate a redshift lower limit $z_{\mathrm{lim}(10^{15})}$ beyond which we would not

have expected to detect enough galaxies for confirmation. Scaling from the already published *Planck* sample, we expect that ∼12 of these unconfirmed candidates may be real clusters.

2.2 Introduction

Massive clusters of galaxies sample the peaks in the dark matter density field, and analyses of their existence, abundance and distribution enable constraints on cosmological parameters and models (e.g. White et al., 1993; Eke et al., 1996; Vikhlinin et al., 2009b; Mantz et al., 2010b; Rozo et al., 2010; Williamson et al., 2011; Hoyle et al., 2012; Mana et al., 2013; Bocquet et al., 2014). Surveys at mm wavelengths allow one to discover galaxy clusters through their SZE, which is due to inverse Compton interactions of Cosmic Microwave Background (CMB) photons with the hot intracluster plasma (Sunyaev & Zel'dovich, 1970, 1972). Since the first SZE-discovered galaxy clusters were reported by the South Pole Telescope (SPT) collaboration (Staniszewski et al., 2009), large solid angle surveys have been completed, delivering many new galaxy clusters (Reichardt et al., 2013; Planck Collaboration, 2013a; Hasselfield et al., 2013).

The SZE observations alone do not enable one to determine the cluster redshift, and so additional followup data are needed. In previous X-ray surveys, it was deemed necessary to obtain initial imaging followed by measurements of spectroscopic redshifts for each cluster candidate (e.g. Rosati et al., 1998; Böhringer et al., 2004; Mehrtens et al., 2012). In ongoing SZE surveys, the efforts focus more on dedicated optical imaging (e.g. Song et al., 2012b; Planck Collaboration, 2013a) to identify the optical counterpart and measure photometric redshifts. In the best case one leverages existing public wide field optical surveys such as the Sloan Digital Sky Survey (York et al., 2000), the Red-Sequence Cluster Survey (Gladders & Yee, 2005) or the Blanco Cosmology Survey (Desai et al., 2012).

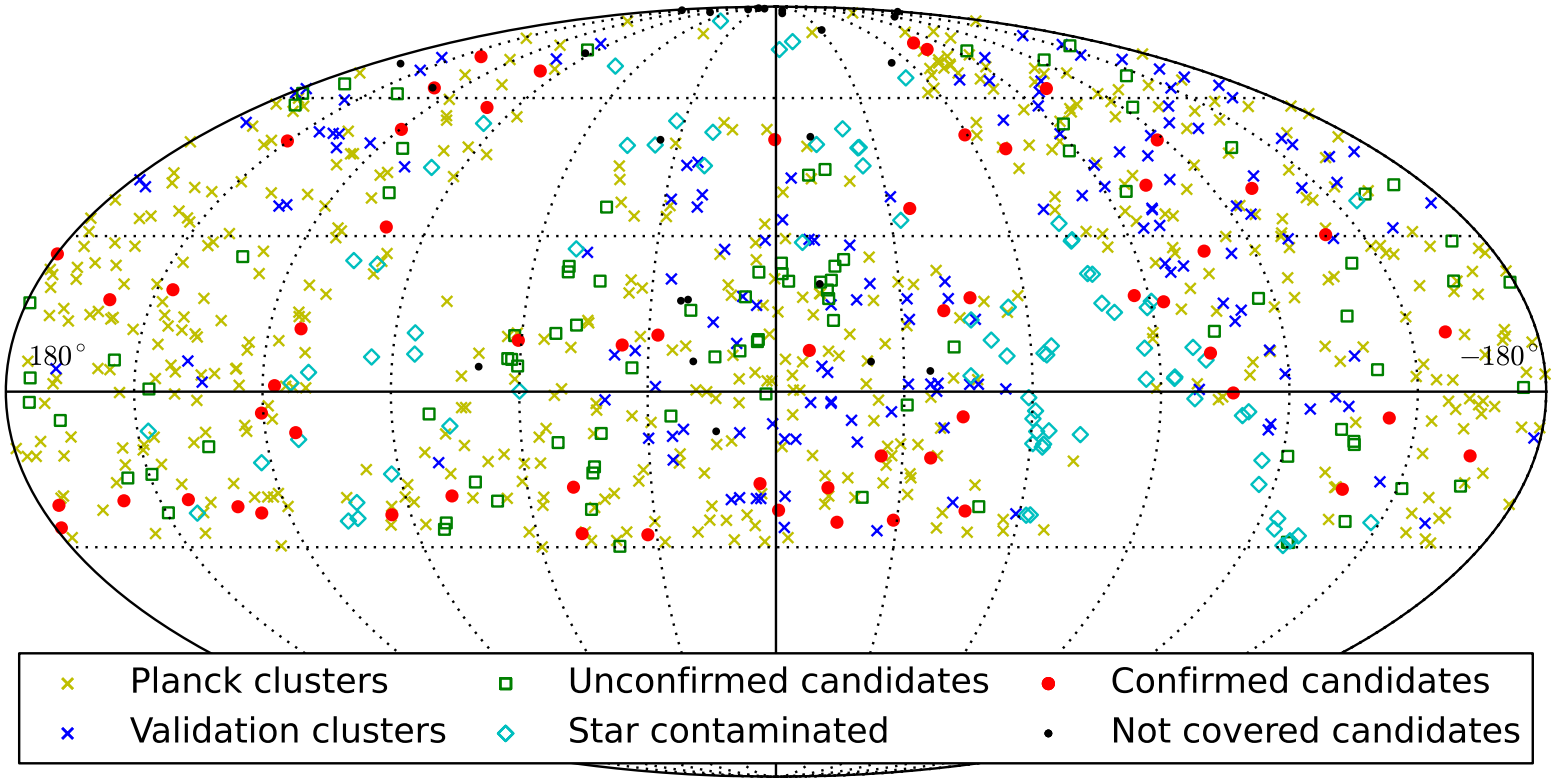

Figure 2.1: The sky distribution of *Planck* clusters and candidates within the PS1 region. The crosses are previously confirmed *Planck* clusters, and the blue crosses mark the validation sample we use in this analysis. For the remainder of the sample of previously unconfirmed *Planck* candidates, black dots mark those that are not fully covered by PS1 data, red circles are clusters we confirm (see Table 2.2), cyan diamonds are candidates that lie in areas of heavy star contamination, and green squares are candidates we do not confirm (see Table 2.3.)

In March 2013 the *Planck* Collaboration released an SZE source catalogue with 1227 galaxy cluster candidates from the first 15 months of survey data (Planck Collaboration, 2013a). Given the full-sky coverage of the *Planck* satellite, there is no single survey available to provide confirmation and redshift estimation for the full candidate list. Of this full sample, 683 SZE sources are associated with previously known clusters (e.g. Meta-Catalogue of X-ray detected Clusters of galaxies, Piffaretti et al. 2011; MaxBCG catalogue, Koester et al. 2007; GMBCG catalogue, Hao et al. 2010; AMF catalogue, Szabo et al. 2011; WHL12 catalogue ,Wen et al. 2012; and SZ catalogues from Williamson et al. 2011; Reichardt et al. 2013; Hasselfield et al. 2013) and 178 are confirmed as new clusters, mostly through targeted follow-up observations. The remaining 366 SZE sources are classified into three groups depending on the probability of their being a real galaxy cluster.

In this paper we employ proprietary Pan-STARRS imaging data and a blinded analysis (Klein & Roodman, 2005) to perform optical cluster identification and to measure photometric redshifts of *Planck* cluster candidates. For those candidates where no optical counterpart is identified, we provide redshift lower limits that reflect the limited depth of the optical imaging data.

This paper is organised as follows: we briefly describe the SZE source catalogue in § 2.3.1 and the optical Pan-STARRS data processing in § 2.3.2. In § 2.4 we provide the details of the photometric redshift (photo-z hereafter) estimation and cluster confirmation pipeline. Results of the photo-z performance and the confirmation of *Planck* candidates are presented in § 2.5.

2.3 Data Description

We briefly describe the *Planck* SZE source catalogue in § 2.3.1 and refer the reader to the cited papers for more details. In § 2.3.2 we then describe the Pan-STARRS optical data and calibration process we use to provide the images and calibrated catalogues needed for the cluster candidate follow up.

2.3.1 Planck SZE Source Catalogue

The *Planck* SZE source catalogue contains 366 unconfirmed cluster candidates, and it is available for download[1]. This catalogue is described in detail elsewhere (see Planck Collaboration, 2013a). In summary, the *Planck* SZE sources are the union of detections from three independent pipelines, which are compared extensively in Melin et al. (2012). The pipelines, which are optimized to extract the cluster SZE signal from the *Planck* CMB data, are drawn from two classes of algorithms, namely two Matched-Multi filter pipelines, which are multi-frequency matched filter approaches (Melin et al., 2006), and the PowellSnakes pipeline, which is a fast Bayesian multi-frequency detection algorithm (Carvalho et al., 2012).

The 'union sample' is the combination of detections from each of these three pipelines with a measured Signal-to-Noise Ratio (SNR) above 4.5. Detections are further merged if they are within an angular separation of ≤ 5 arcmin. The detection, merging and combination pipelines have been tested using simulations and achieve a purity of 83.7 per cent (Planck Collaboration, 2013a). With a sample of 1226 cluster candidates, we estimate that approximately 200 are noise fluctuations. Because a large number of candidates have already been confirmed, we expect only $(1 - 200/366) \sim 45$ per cent of the 366 unconfirmed candidates to be real clusters.

[1] `http://pla.esac.esa.int/pla/aio/planckProducts.html`.

The candidates in the union sample are grouped into three classification levels according to the likelihood of being a cluster. Class 1 is for high-reliability candidates that have a good detection in the SZE and are also associated with *ROSAT* All Sky Survey (RASS; Voges et al., 1999) and Wide-field Infrared Survey Explorer (WISE; Wright et al., 2010) detections. The Class 2 candidates meet at least one of the three criteria in Class 1. The Class 3 candidates correspond to low-reliability candidates that have poor SZE detections and no clear association with RASS or WISE detections. A total of 237 unconfirmed *Planck* cluster candidates (Class 1, 2 and 3) lie within the Pan-STARRS footprint with enough coverage (c.f. Figure 2.1 and § 2.3.2).

The union sample also contains redshifts for previously known and confirmed clusters. We create a validation sample by randomly selecting 150 of these clusters that fall within the Pan-STARRS footprint and have quoted *Planck* redshift uncertainties of < 0.001. We combine these 150 confirmed clusters with the sample of 237 cluster candidates for a total sample of 387 clusters and candidates. We subject all targets in our total sample to the same procedure. This blind analysis of our optical confirmation and photo-z estimation pipelines enables an important test of our methods as well as the characterisation of our photometric redshift uncertainties. Note that the heterogeneous nature of *Planck* confirmation may result in a different redshift and mass distribution of the validation sample from that of unconfirmed clusters, but we do not expect this to lead to any important bias. In what follows we refer to both confirmed clusters and cluster candidates within this total combined sample as 'candidates'.

For each candidate we use the following additional information given by each of the three individual SZE detection pipelines: the candidate position (Right Ascension α, Declination δ), the position uncertainty, the best-estimated angular size ($\theta_{\rm s}$), and the integrated SZE signal $Y_{\rm sz}$ from the $\theta_{\rm s}$–$Y_{\rm sz}$ likelihood plane provided with the *Planck* data products. Furthermore, we convert the size to an angular estimate of $\theta_{500} = c_{500}\theta_{\rm s}$, where the concentration is set to $c_{500} = 1.177$ as used in the cluster detection pipelines (Planck Collaboration, 2013a). This angular radius θ_{500} corresponds to the projected physical R_{500} within which the density is 500 times the critical density at the redshift of the cluster. In Figure 2.2 we show the $Y_{\rm sz} - \theta_{500}$ distribution of the combined sample used in this work.

2.3.2 PAN-STARRS1 Data

For each candidate we retrieve the single epoch detrended images from the PS1 data server and use those data to build deeper coadd images in each band. This involves cataloguing the single epoch images, determining a relative calibration, combining them into coadd images, cataloguing the coadds and then determining an absolute calibration for the final multi-band catalogues. We describe these steps further below.

Data Retrieval

The Pan-STARRS (Kaiser et al., 2002) data used in this work are obtained from a wide field 1.8 metre telescope situated on Haleakala, Maui in Hawaii. The PS1 telescope is equipped with a 1.4 gigapixel CCD covering a 7 deg^2 field of view, and it is being used in the PS1 survey to image the sky north of $\delta = -30°$. The 3π survey is so named because it covers 75 per cent of the celestial sphere. The PS1 photometric system is similar to the SDSS filter system with $g_{\rm P1}$, $r_{\rm P1}$, $i_{\rm P1}$, $z_{\rm P1}$, $y_{\rm P1}$ (where SDSS had u), and a wide band $w_{\rm P1}$ for use in the

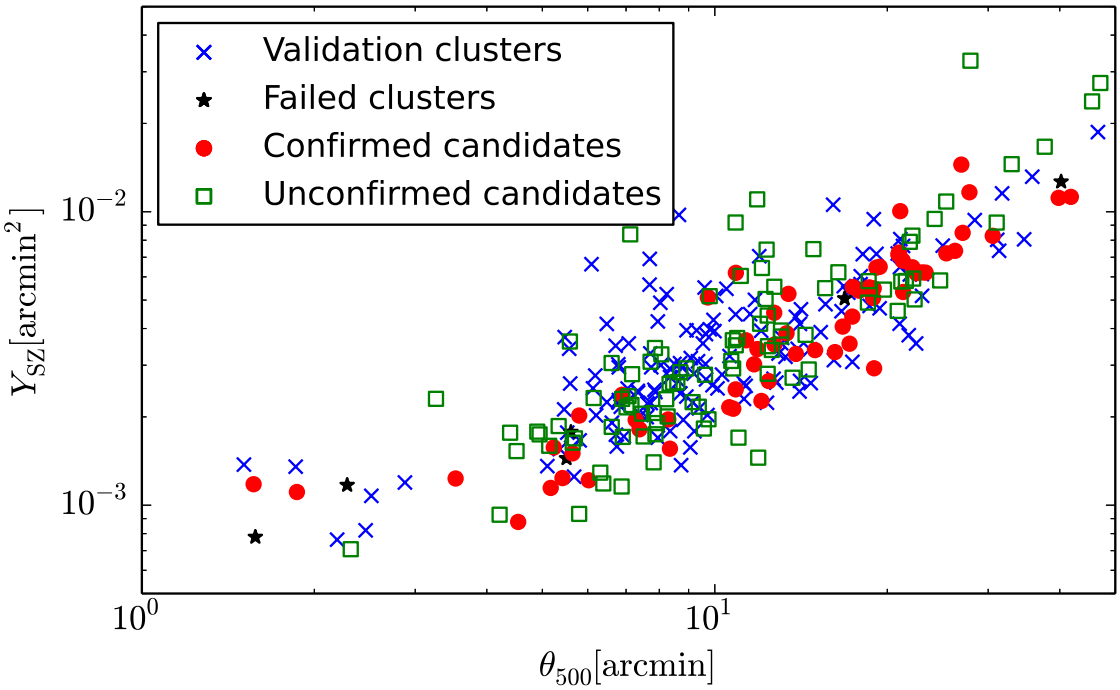

Figure 2.2: The Y_{sz}–θ_{500} distribution of *Planck* clusters and candidates in our sample. The *Planck* confirmed clusters are shown with blue crosses, and the six cases where our pipeline failed to confirm the systems are marked with black stars (see § 2.5 for more details). The *Planck* candidates with PS1 data are shown with red circles if we are able to measure a corresponding photometric redshift and with green squares if not.

detection of Near Earth Objects (Tonry et al., 2012). In this study we process data from the first four filters and denote them as *griz*.

We obtain single epoch, detrended, astrometrically calibrated and warped PS1 imaging data (Metcalfe et al., 2013) using the PS1 data access image server. We use 3PI.PV2 warps wherever available and 3PI.PV1 warps in the remaining area. We select those images that overlap the sky location of each candidate, covering a square sky region that is $\sim 1^\circ$ on a side. The image size ensures that a sufficient area is available for background estimation.

Single Epoch Relative Calibration

The subsequent steps we follow to produce the science ready coadd images and photometrically calibrated catalogues are carried out using the Cosmology Data Management system (CosmoDM), which has its roots in the Dark Energy Survey data management system (Ngeow et al., 2006; Mohr et al., 2008, 2012) and employs several AstrOMatic codes that have been developed by Emmanuel Bertin (Institut d'Astrophysique de Paris).

We build catalogues from the PS1 warped single epoch images using SExtractor (Bertin & Arnouts, 1996). The first step is to produce a model of the Point Spread Function (PSF) variations over each of the input single epoch images. This requires an initial catalogue containing stellar cutouts that are then built, using PSFEx (Bertin, 2011), into a position

dependent PSF model. With this model we then recatalog each image using model fitting photometry with the goal of obtaining high quality instrumental stellar photometry over each input image.

For each band, relative photometric calibration is performed using these catalogues; we compute the average magnitude differences of stars from all pairs of overlapping images and then determine the relative zeropoints using a least squares solution. The stars are selected from the single epoch catalogues using the morphological classifier `spread_model` (e.g. in particular $|$`spread_model`$| < 0.002$; see Desai et al., 2012; Bouy et al., 2013). We use the PSF fitting magnitude `mag_psf` for this relative calibration.

We test the accuracy of the single epoch model fitting relative photometry by examining the variance of multiple, independent measurements of stars. Figure 2.3 contains a histogram of the so-called repeatability of the single epoch photometry. These numbers correspond to the Root Mean Square (RMS) variation of the photometry of bright stars scaled by $1/\sqrt{2}$, because this is a difference of two measurements. We extract these measurements from the bright stars where the scatter is systematics dominated (i.e. the measurement uncertainties make a negligible contribution to the observed scatter). We measure this independently for each band and candidate and use the behaviour of specific candidate tiles relative to the ensemble to identify cases where the single epoch photometry and calibration need additional attention. The median single epoch repeatability scatter is 16, 18, 19, and 17 mmag in *griz*, respectively.

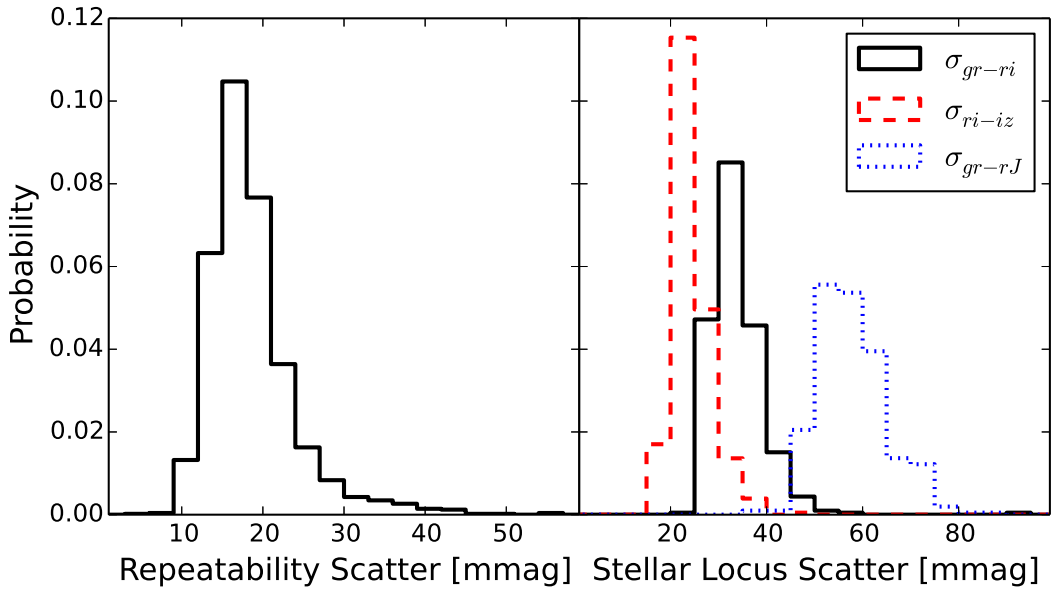

Figure 2.3: The left panel shows the histogram of single epoch repeatability scatter, extracted for bright stars in the full ensemble of candidates. All bands have similar distributions, and so only the combined distribution is shown. The median scatter is 16, 18, 19, and 17 mmag in *griz*, respectively. The right panel shows the histogram of the stellar locus scatter extracted from the full ensemble of 387 candidates. The median values of the scatter distributions for all candidates are 34, 24, and 57 mmag in *g*–*r* vs. *r*–*i*, *r*–*i* vs. *i*–*z* and *g*–*r* vs. *r*–*J* colour spaces.

As part of this process we obtain PSF Full Width Half Maximum (FWHM) size measurements for all single epoch images. The median FWHM for the full ensemble of imaging over all cluster candidates is $1\farcs34$, $1\farcs20$, $1\farcs12$, and $1\farcs09$ in *griz*, respectively.

Coaddition, Cataloguing and Absolute Calibration

The coadd images are then generated from the single-epoch images and associated relative zero points. For each candidate tile we generate both PSF homogenized and non-homogenized coadds. To create the homogenized coadds, we convolve the input warp images to a PSF described by a Moffat function with FWHM set to equal the median value in the single epoch warps overlapping that candidate. We homogenize separately for each band. We then combine these homogenized and non-homogenized warps using SWarp (Bertin et al., 2002) in a median combine mode. We create a χ^2 detection image (Szalay et al., 1999) from the homogenized coadds using both *i* and *z* bands. The PSF homogenized coadds are then catalogued using SExtractor in dual image mode with this χ^2 detection image. We use SExtractor in PSF correcting, model fitting mode. The non-homogenized coadds are only used for visual inspection and for creating pseudo-colour images of the candidates (see Figure 2.4). For a more detailed discussion of coadd homogenization on a different survey dataset, see Desai et al. (2012).

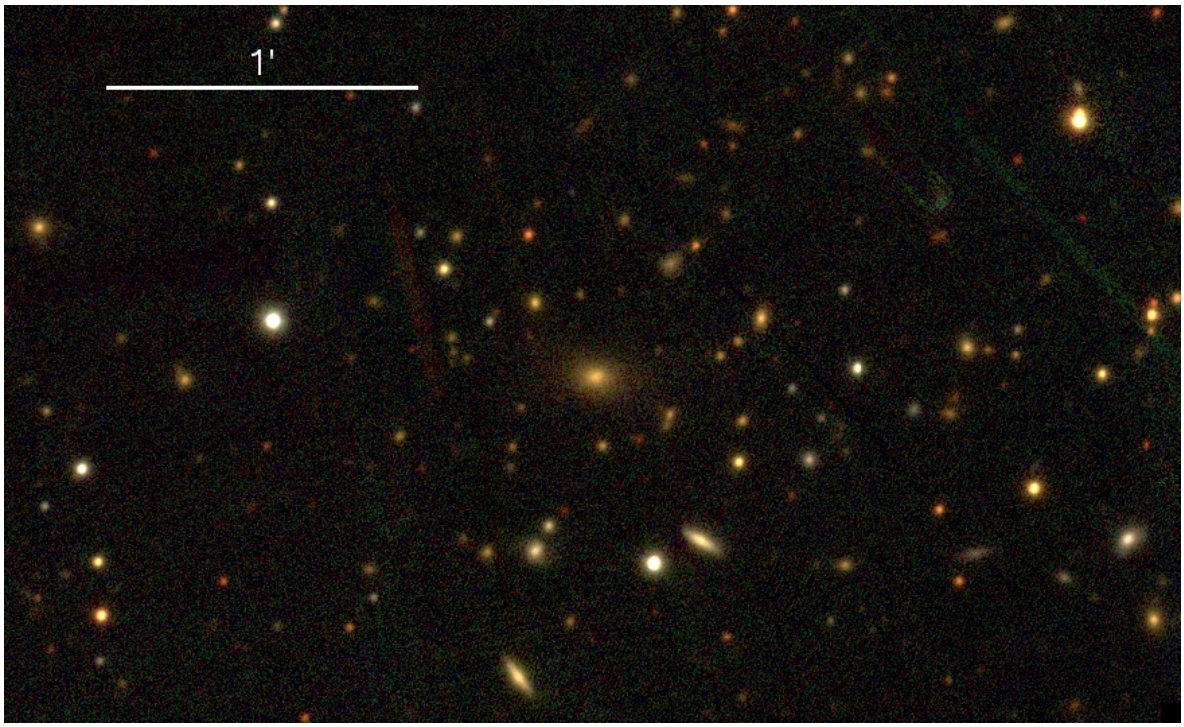

Figure 2.4: Example pseudo-colour image in the *gri* bands of cluster candidate 218. In this case the *Planck* SZE candidate centre is about 4 arcmin away from the BCG, which is at the centre of this image. This exemplifies an extreme case of the large offset between the *Planck* centre and the BCG.

We use the stellar locus together with the absolute photometric calibration from the 2MASS survey (Skrutskie et al., 2006) for the final, absolute photometric calibration for our

data (see also Desai et al., 2012, and references therein). For this process we adopt the PS1 stellar locus measured by Tonry et al. (2012).

In our approach we first apply extinction corrections to the relative photometry from the catalogues using the dust maps from Schlegel et al. (1998). This correction removes the overall Galactic extinction reddening, making the stellar locus more consistent as a function of position on the sky. As is clear from Figure 2.1, the *Planck* cluster candidates extend to low galactic latitude, and some lie in locations of extinction as high as $A_V = 1.8$ mags. Most of the targets with $A_V > 0.5$ mag also have very high stellar contamination, making it impossible for us to use the PS1 data for candidate confirmation. High et al. (2009) examined photometrically calibrated data lying in regions with a range of extinction reaching up to $A_V \sim 1$ mag, showing that within this range the stellar locus inferred shifts are equivalent to the Galactic extinction reddening corrections to within an accuracy of ∼20 mmag.

We then determine the best-fit shifts in *g*–*r* and *r*–*i* that bring our observed stellar sample to coincide with the PS1 locus. We repeat this procedure for *i*–*z* while using the *r*–*i* result from the previous step. This allows for accurate colour calibration for the PS1 bands used for the cluster photometric redshifts. To obtain the absolute zeropoint, we adjust the *g*–*r* vs. *r*–*J* locus until it coincides with the PS1 locus. This effectively transfers the ∼2 per cent 2MASS photometric calibration (Skrutskie et al., 2006) to our PS1 catalogues.

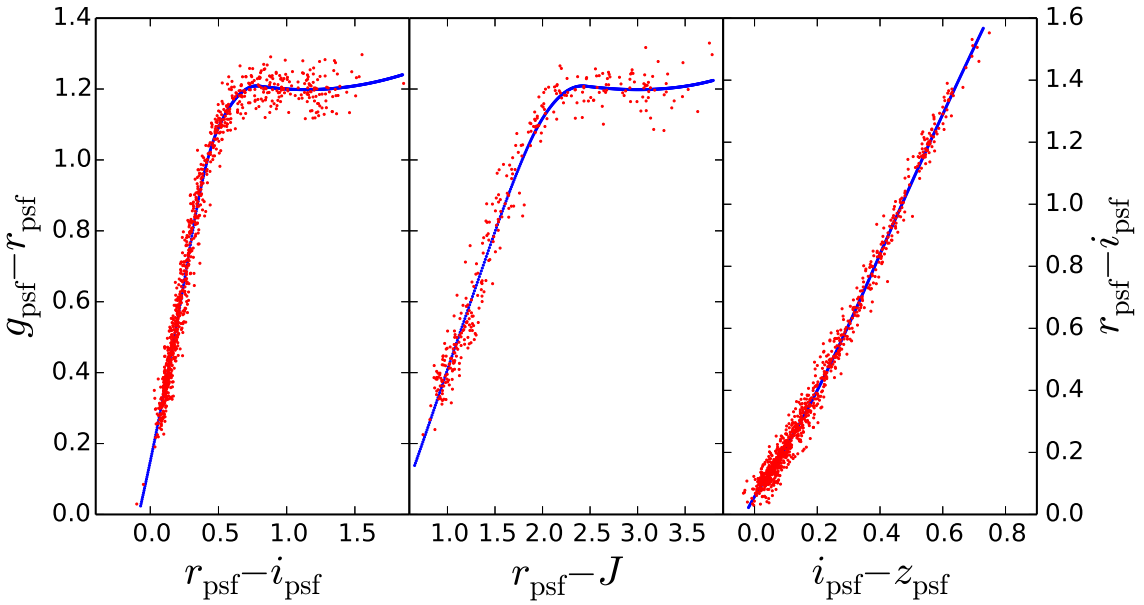

Figure 2.5: The stellar loci in three different colour-colour spaces for the *Planck* cluster 307 are shown. The blue line shows the PS1 stellar locus, and red points show PSF model fitting magnitudes of stars from our catalogues for this tile. We use the stellar locus for absolute photometric calibration. The scatter about the stellar locus provides a good test of photometric quality; for this cluster the values of the scatter in *g*–*r* vs. *r*–*i* (left), *g*–*r* vs. *r*–*J* (middle) and *r*–*i* vs. *i*–*z* (right) colour spaces are 29, 48 and 17 mmag, respectively.

An illustrative plot of the stellar loci for *Planck* cluster 307 is shown in Figure 2.5. The scatter of our model fitting photometry about the stellar locus provides a measure of the

accuracy of the coadd model fitting photometry. In the case of candidate 307 the scatter around the stellar locus in g–r vs. r–i, g–r vs. r–J, and r–i vs. i–z is 29, 48, and 17 mmag, respectively. In Figure 2.3 we show the histogram of scatter for the ensemble of candidates in each of these colour–colour spaces. The median scatter of the stellar locus is 34, 24, and 57 mmag in g–r vs. r–i, r–i vs. i–z, and g–r vs. r–J, respectively. These compare favourably with the scatter obtained from the SDSS and BCS datasets (Desai et al., 2012). Note that the shallow 2MASS photometry contributes significantly to the scatter in one colour-colour space, but in the others we restrict the stars to only those with photometric uncertainties <10 mmag (see Figure 2.3). We use the scatter measurements within each candidate tile together with the behaviour of the ensemble to identify any candidates that require additional attention. We note that the PS1 ubercal calibration method (Schlafly et al., 2012) has been able to achieve internal photometric precision of < 10 mmag in photometric exposures in g, r, and i and $\simeq 10$ mmag in z, but it has not been applied over the whole 3PI dataset yet.

We estimate a photometric 10 σ depth, above which the galaxy catalogue is nearly complete, in each coadd by calculating the mean magnitude of galaxies with `mag_auto` uncertainties of 0.1. In Figure 2.6 we show the histograms of the distribution of depths in each band; the median depths in *griz* are 20.6, 20.5, 20.4 and 19.6 (denoted by dotted lines). We note that the median depths are shallower than the limiting depths reported by the PS1 collaboration (Metcalfe et al., 2013), but this difference is mainly due to a different definition of the depth. We find that to this depth the magnitude measurements from `mag_auto` and the colour measurements using `det_model` are well suited for the redshift estimation analysis which we describe in § 2.4.2.

Variation in observing conditions leads to non uniform sky coverage across the PS1 footprint. One result is that the depth varies considerably from candidate to candidate; another is that not all candidates are fully covered in each of the bands of interest. Overall 388 cluster candidates have been fully covered. In Figure 2.1 we show the sky distribution of our full sample together with that of the *Planck* sample.

2.4 Method

In this section we describe the optical confirmation and redshift estimation technique that we apply to the PS1 galaxy catalogues (see § 2.4.1). Then in § 2.4.2 we describe the method we use – especially in candidates without optical counterparts – to estimate the redshift lower limit as a function of the field depth.

2.4.1 Confirmation and Redshift Estimation

We employ the red sequence galaxy overdensity associated with a real cluster to identify an optical counterpart for the *Planck* candidates and to estimate a photometric redshift; our method follows closely that of Song et al. (2012a), which has been applied within the South Pole Telescope (SPT) collaboration to confirm and measure redshifts for 224 SZE selected cluster candidates (Song et al., 2012b). A similar approach has been used to identify new clusters from optical multi-band surveys using only the overdensity of passive galaxies with similar colour (Gladders & Yee, 2005). We start with additional information from the SZE or X-ray about the sky location and, in principle, also a mass observable such as the SZE or X-ray flux that can be used at each redshift probed to estimate the cluster mass and

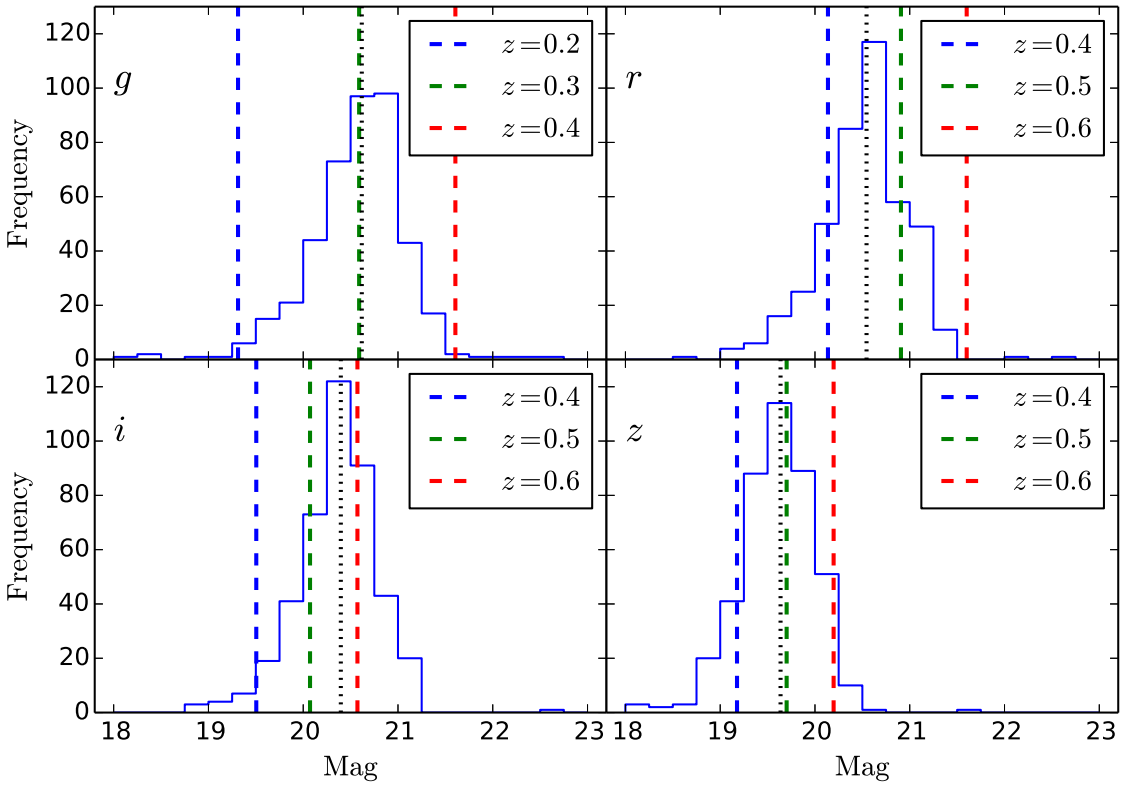

Figure 2.6: The distributions of *griz* band 10σ depths (`mag_auto`) for PS1 fields around each *Planck* candidate. The dashed lines mark the magnitudes of $L^\star$ galaxies at different redshifts. The dotted lines mark the median depths, which are 20.6, 20.5, 20.4 and 19.6 in *griz*, respectively. The PS1 data are typically deep enough for estimating cluster redshifts out to or just beyond $z = 0.5$ (see also Figure 2.8).

characterise the scale of the virial region within which the red sequence search is carried out (Hennig et al, in preparation). We describe the procedure below.

We model the evolutionary change in colour of cluster member galaxies across cosmic time by using a composite stellar population model initialised with an exponentially decaying starburst starting at redshift $z = 3$ with decay time $\tau = 0.4$ Gyr (Bruzual & Charlot, 2003). We introduce tilt into the red sequence of the passive galaxies by adopting 6 models with different metallicities adjusted to follow the observed luminosity–metallicity relation in Coma (Poggianti et al., 2001). Using the absolute PS1 filter transmission curves, which include atmospheric, telescope, and filter corrections (Tonry et al., 2012), as inputs for the package *EzGal* (Mancone & Gonzalez, 2012), we generate fiducial galaxy magnitudes in *griz* bands over a range of redshifts and within the range of luminosities $3L^\star \geq L \geq 0.3L^\star$, where $L^\star$ is the characteristic luminosity in the Schechter (1976) luminosity function.

We exclude faint galaxies by employing a minimum magnitude cut of $0.3L^\star$; to reduce the number of junk objects in the catalogue we remove all objects with a magnitude uncertainty > 0.3. In Song et al. (2012b) a fixed aperture is used to both select cluster galaxies and perform

background subtraction. In this work we use the *Planck* derived radius θ_{500} centred on the position of the candidate to separate galaxies into cluster and field components. Galaxies located between$(1.5–3)\theta_{500}$ are used to estimate background corrections. Each galaxy within the radial aperture θ_{500} is assigned two weighting factors. The first one is a Gaussian colour weighting corresponding to how consistent the colours of the galaxy are with the modelled red sequence at that redshift. This red likelihood, $\mathcal{L}_{\rm red}$, is calculated separately for each of the following colour combinations: *g*–*r* and *g*–*i*, which are suitable for low redshift ($z < 0.35$) estimation, and *r*–*i* and *r*–*z*, which are suitable for intermediate redshift ($0.35 < z < 0.7$) estimation. The second factor weights the galaxy depending on the radial distance to the cluster centre, $\mathcal{L}_{\rm pos}$, and for this function we adopt a projected NFW profile (Navarro et al., 1997) with concentration $c = 3$. In this way, all galaxies physically close to the cluster centre and with colours consistent with the red sequence at the redshift being probed are given higher weight. Conversely any galaxies in the cluster outskirts with colours inconsistent with the red sequence are given a small weight.

The method then scans a redshift range $0 < z < 0.7$ with an interval $\delta z = 0.01$ and iteratively recomputes the above weight factors using the modelled evolution of the red sequence. For each cluster candidate we construct histograms of the weighted number of galaxies as a function of redshift for each above-mentioned colour combination. The weighted number of galaxies is determined for each colour combination as the background subtracted sum of all galaxy weights at each given redshift.

For each cluster we identify the appropriate colour combination using a visual examination of the red sequence galaxies within the cluster centre and record the BCG position, if possible. The final photo-z is estimated by identifying the most significant peak in the background corrected likelihood histogram from all galaxies within θ_{500}. The associated photo-z uncertainty is determined from the width of a Gaussian fit to the peak with outliers at $> 3\sigma$ removed. Specifically, the photo-z uncertainty $\delta z_{\rm phot}$ is the standard deviation of the Gaussian divided by the square-root of the weighted galaxy number in the peak. The performance is presented in the following section. We note that, given the depth of the data (see Figure 2.6), we are unable to identify candidates with redshifts $z > 0.7$.

The optical confirmation and photo-z estimation break down if no significant peak is found in the likelihood histogram. In addition to the case where the candidate is not a cluster, there are three categories of failure that are possible: (1) those candidates with a *Planck* θ_{500} that is so small such that there are not enough red sequence galaxies within the search aperture, (2) those that have a radius θ_{500} above 30 arcminutes, in which case our standard $0.7^\circ \times 0.7^\circ$ coadd catalogue region typically does not contain enough remaining area to measure the background well, and (3) those candidates that have a relatively large offset between the visually confirmed cluster centre and the *Planck* position. Clusters with $\theta_{500} > 30''$ all lie at low redshift, where– given the sensitivity of the *Planck* SZE selection – we would expect these systems to have already have been confirmed by low redshift all sky surveys (e.g. Abell, 1958; Abell et al., 1989; Voges et al., 1999). For cases 1 and 2, we rerun the pipeline with a radius of 5 arcmin, which is the same as the *Planck* matching radius. For the 3rd case we recenter at the coordinates of the BCG if a BCG can be identified within the coadd region. With the approach described above, the uncertainties associated with the *Planck* candidate position and size have no significant impact on our confirmation and photo-z estimation. We demonstrate this with the validation sample in § 2.5.1.

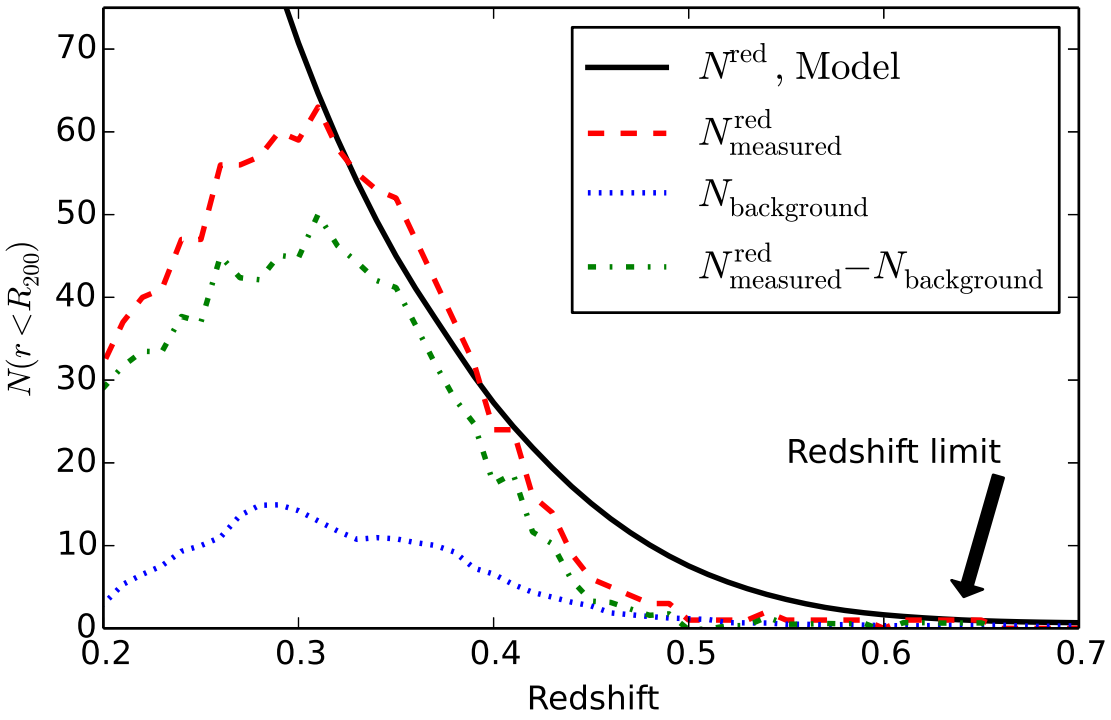

Figure 2.7: The observed number of red galaxies in the *Planck* confirmed cluster 442 at $z = 0.3436$. The red dashed line is the red sequence galaxy number within R_{200}; the blue dotted line is the background number corrected to the R_{200} area of the cluster; and the green dash-dot line is the difference between those two. The black line is the predicted number of red sequence galaxies $N^{\rm red}$, which increases towards lower redshift as more and more faint galaxies in the luminosity function slide above the imaging detection threshold. We use this function together with the background to estimate a redshift lower limit in cases where no optical counterpart is identified.

2.4.2 Redshift Lower Limits $z_{\rm lim(10^{15})}$

For clusters where there is no obvious over-density of red sequence galaxies, there are two possibilities: (1) the candidate is a noise fluctuation, or (2) the cluster is at high enough redshift that the PS1 imaging data is not deep enough to detect the cluster galaxy population. Given the contamination estimates provided by the *Planck* collaboration, we expect approximately half of our candidates to be noise fluctuations. However, of the 45 per cent that are real clusters we expect a small fraction of them to lie at redshifts too high to be followed up using the PS1 data. In particular, the observed redshift distribution of the 813 previously confirmed *Planck* clusters has 3 per cent of those clusters lying at $z > 0.60$, which is a reasonable expectation of the redshift limit to which we could expect to use PS1 data to confirm a cluster. Simple scaling suggests we should expect approximately 3 clusters to lie at $z > 0.6$ in our candidate sample. Thus, for each of these undetected systems we calculate the minimum redshift $z_{\rm lim(10^{15})}$ beyond which the candidate would be undetectable in our PS1 imaging.

To estimate the redshift lower limit we first measure the depth of the catalogue at the coordinates of the candidate (see Figure 2.6) and then predict, as a function of redshift, the statistical significance of the detectable galaxy overdensity above background. To do this we adopt a typical mass for a *Planck* cluster of $M_{200} = 1 \times 10^{15} M_{\odot}$ and use a model for the Halo Occupation Distribution (HOD) of red sequence galaxies in SZE selected clusters of this mass (Hennig et al, in preparation). That analysis uses a joint dataset consisting of 77 SPT selected clusters and Dark Energy Survey (DES) imaging of the galaxy populations for clusters with $M_{200} > 4 \times 10^{14} M_{\odot}$ extending over the redshift range $0 < z < 1.2$. The results are in good agreement with those from a sample of ~ 100 clusters studied in the local Universe (Lin et al., 2004).

The estimated number of detectable red cluster galaxies $N_i^{\rm red}(z)$ for candidate i at redshift z can be expressed as

$$N_i^{\rm red}(z) = \left[1 + V\phi_{\star}(z) \int_{y_{\rm L}}^{+\infty} y^{\alpha} e^{-y} {\rm d}y\right] \times f_{\rm r}(z), \tag{2.1}$$

where $\phi_{\star}(z)$ is the characteristic number density of galaxies, α is the faint end slope, $y = L/L^{\star}(z)$ where $L^{\star}(z)$ is taken from the passive evolution model used in this work, V is the virial volume, and $y_{\rm L}$ is the luminosity limit determined from the catalogue depth for the candidate. For these parameters we adopt values that are consistent with the Hennig et al (in preparation) results. Namely, we use $\phi_{\star}(z) = 3.6E(z)^2[{\rm Mpc}^{-3}{\rm mag}^{-1}]$ and $\alpha = -1.05(1+z)^{-2/3}$. The 1 comes from the fact that the BCG is not included in this scaling relation, but needs to be counted in the Halo Occupation Number (HON). We additionally multiply by the red fraction, $f_{\rm r}(z) = 0.8(1+z)^{-1/2}$, at the appropriate redshift. Finally, we apply a correction to relate the number of galaxies within R_{200} to the number of galaxies projected within R_{500}. For this correction we adopt an NFW distribution of galaxies with concentration $c_{200} = 3$.

The measured number of red galaxies is determined directly from the candidate catalogue as follows. We set a magnitude error cut of 0.3 and a magnitude limit of $0.3L^{\star}$ in analogy to the photo-z estimation and sum all galaxies with $\mathcal{L}_{\rm red} > 0.05$ projected within the R_{500} radius, which is converted from the typical *Planck* mass cluster ($M_{200} = 1 \times 10^{15} M_{\odot}$) using an NFW model with concentration c (Duffy et al., 2008). We set the centre of the candidate to be the visually identified BCG position if it is available, or, alternatively, we use the *Planck* candidate centre. The background number is extracted from the area beyond $3R_{500}$ and a correction for the differences in cluster search and background area is applied.

Given the individual catalogue depth, we estimate the redshift lower limit as the lowest redshift where the background galaxy population has at least a 5 per cent chance to be as large as that expected for a cluster of $M_{200} = 1 \times 10^{15} M_{\odot}$. That is, we require that the predicted cluster galaxy population be detectable above background at a minimum of $2\,\sigma$. We first calculate the HON from Equation (2.1) for all redshifts (black line in Figure 2.7); we then measure the number of red sequence galaxies in the background region and correct it for the difference in area between the cluster search and background region. Finally, we find the highest redshift such that the cluster would be detected with $2\,\sigma$ significance. The depths for all candidates are plotted in Figure 2.8 and reported for each unconfirmed candidate in Table 2.3; the median redshift lower limit for our data is $z_{\rm lim(10^{15})} = 0.60$.

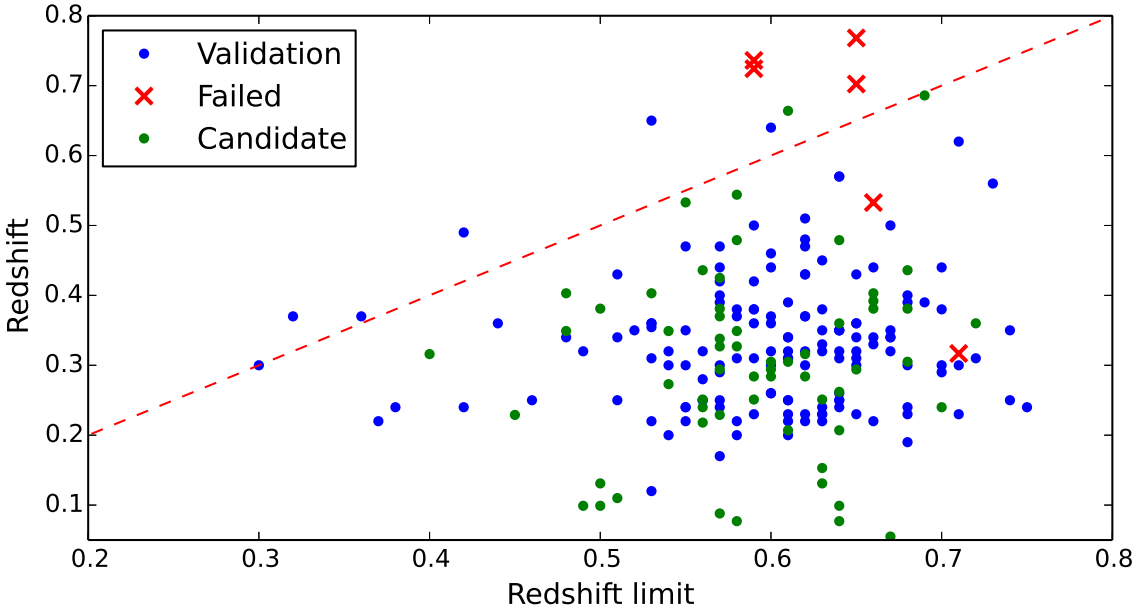

Figure 2.8: We plot the redshift lower limit $z_{\mathrm{lim}(10^{15})}$ for a cluster with mass $M_{200} = 1{\times}10^{15} M_{\odot}$ versus cluster photometric redshift for the clusters in the validation sample (blue points) and the clusters we have confirmed in PS1 (green points). Six red crosses mark the systems in the validation sample (with spectroscopic redshifts) that we failed to confirm; we discuss these in § 2.5.1. Clusters below the red dashed line have the required PS1 imaging depth to enable a robust redshift measurement. Those clusters above the line are marked as having shallow data in Figure 2.9.

2.5 Results

We apply our method to the entire sample of 388 candidates in a uniform manner. Thereafter, we examine the subset of candidates that are previously confirmed clusters to validate our method. Our approach of blinding the sample eliminates any possible confirmation bias and allows us to accurately estimate the failure rate and to test our photometric redshift uncertainties. We then discuss the remaining candidates, presenting new photometric redshifts where possible.

2.5.1 Validation Using Confirmed Planck Clusters

In Figure 2.8 we plot the redshift lower limit $z_{\mathrm{lim}(10^{15})}$ versus the measured redshift of the candidates (using spectroscopic redshifts for those previously confirmed clusters). We mark the successful validation clusters in blue, the validation clusters for which the redshift measurement failed in red, and the new candidates in green. The dashed red line indicates where the $z_{\mathrm{lim}(10^{15})}$ is equal to the cluster redshift. Candidates that lie below this line have PS1 data that are sufficiently deep given the actual cluster redshift that we expect to extract a robust photo-z. Candidates above the line would benefit from deeper imaging data, and for this reason we flag them as "shallow".

Beyond the redshift limit, we can reliably assign a redshift for some candidates, and this

Table 2.1: Photo-z comparison for Rozo et al. (2014) sample.

ID	*Planck*	SDSS	PS1	Rozo's comment
13	0.429	**0.325**	0.35	
97	0.361	**0.310**	0.29	
216	**0.336**	**0.359**	0.30	Mismatch
443	0.437	**0.221**	0.22	
484	0.317	-	-	Unconvincing
500	**0.280**	0.514	0.32	Bad photometry
527	0.385	-	0.32	Unconvincing
537	0.353	**0.287**	0.30	
865	0.278	**0.234**	0.24	
1216	**0.215**	-	0.24	RedMaPPer incompleteness

Note. The final correct redshift marked by Rozo et al. (2014) is written in bold.

is not surprising. The model we adopt in estimating the redshift lower limit $z_{\mathrm{lim}(10^{15})}$ assumes a particular cluster mass, and many *Planck* candidates are indeed even more massive. Also, our model does not account for the scatter in the expected number of red galaxies in a cluster at a particular redshift and mass. In general, we would expect the photo-z's for these systems to be less robust, and indeed, we find that these systems show larger photometric redshift errors than the rest of the candidates.

The blinded photo-z estimation method fails to recover 6 of the 150 *Planck* confirmed clusters in the validation sample. Four of these cases correspond to clusters with redshifts above 0.7, which are beyond the redshift lower limits $z_{\mathrm{lim}(10^{15})}$ estimated from the depths of the PS1 data. The other two failures are at redshifts below the estimated redshift lower limit. One of these is *Planck* 484, which is a low-z cluster which is physically offset from the SZE detection by more than 5 arcmin. In this case we repeat the analysis after recentering on the correct position and recover the *Planck* redshift. The last failure corresponds to the cluster *Planck* 556 which is at a redshift of $z \approx 0.71$. We note that in this case there is a low significance detection in the likelihood histogram, but we were not able to confirm it as a cluster. A possible explanation is that this system has a somewhat lower mass than the characteristic mass we adopt in estimating the redshift lower limit. Indeed, we find that both of these failed systems have relatively low values of Y_{sz}, suggesting that they are lower mass systems. Given the overall success (148/150) of the validation set, we are satisfied that if our depth estimate indicates we should be able to measure a cluster photometric redshift we will be able to do that with good reliability.

We also note that Rozo et al. (2014) present a comparison of the *Planck* redshifts with the RedMaPPer result based on SDSS data. We cross-match the validation sample used here with the $3\,\sigma$ outliers from table 1 of Rozo et al. (2014) and present the result in Table 2.1. Our results for the outliers are generally more consistent with the results from Rozo et al. (2014).

After estimating the redshifts for all candidates, we compare the photometric redshifts of the validation clusters with their spectroscopic redshifts and present this distribution in Figure 2.9. After removing the failures and the questionable clusters identified in Rozo et al. (2014), we are left with 136 *Planck* clusters. We measure the RMS scatter defined as $(z_{\mathrm{photo}} - z_{\mathrm{spec}})/(1 + z_{\mathrm{spec}})$ using the full spectroscopic cluster sample to be 0.023. We note that the

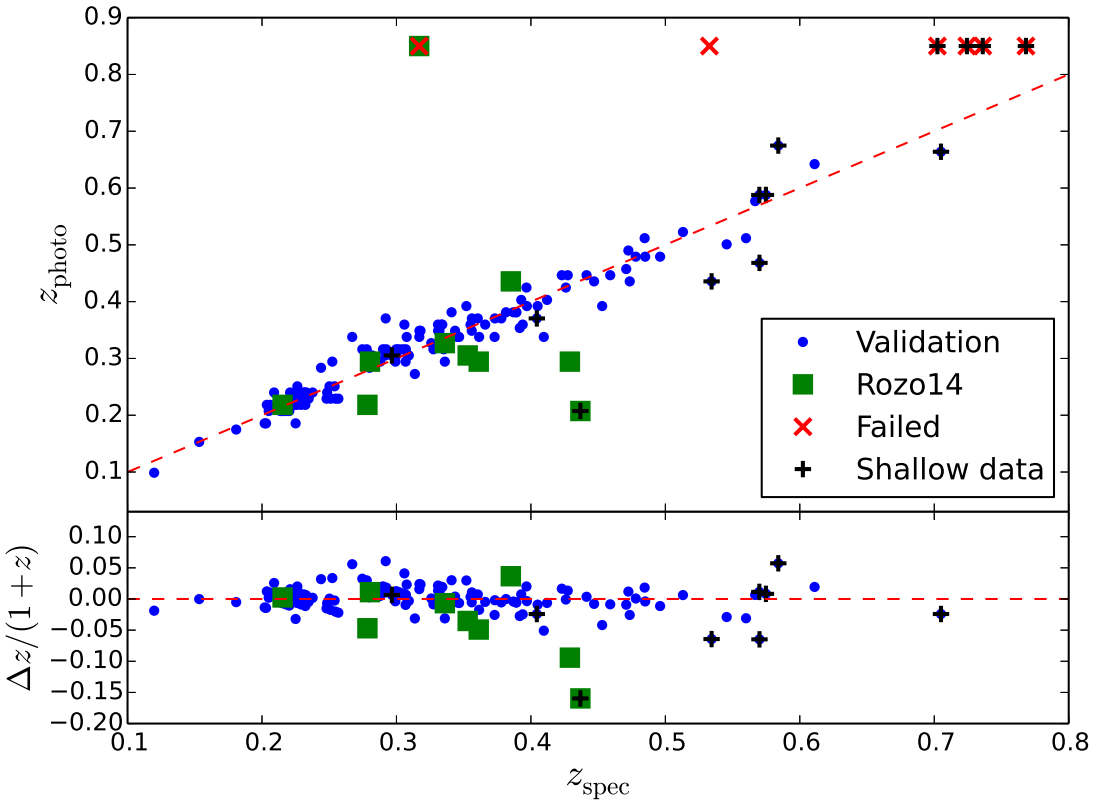

Figure 2.9: The photo-z measurements for *Planck* confirmed clusters plotted versus the spectroscopic redshifts (blue points). The red crosses mark the failures in our photo-z estimation. The black crosses mark the clusters whose redshifts are higher then the redshift limits, and the green squares marks the outliers examined in Rozo et al. (2014).

redshift error distribution has a slight bias (0.003) that can be characterized empirically by a linear model. We apply the bias correction to the measured candidate redshift values when quoting the final photo-z estimation. After applying this bias correction, we obtain an RMS value of 0.022. This value compares favorably with that of Song et al. (2012b) who measure an RMS scatter for three different photometric redshift estimation methods of between 0.028 and 0.024. We are satisfied that the measured RMS in this work demonstrates our ability to measure photometric redshifts for the *Planck* cluster candidates with the PS1 data.

Similar to Song et al. (2012b), we estimate the final photo-z uncertainty as the quadrature sum of the measurement uncertainty and an intrinsic or systematic uncertainty $\delta_{\rm sys}$: $\Delta^2 z_{\rm phot} = \delta^2_{z{\rm phot}} + \delta^2_{\rm sys}$. We find $\delta_{\rm sys} = 0.007$ by requiring that the reduced $\chi^2 = 1$ of the photometric redshifts about the spectroscopic redshifts for the validation ensemble.

2.5.2 Results from the Planck Candidates Sample

We are able to identify optical counterparts and measure redshifts for 60 of the full sample of 237 *Planck* candidates. The *Planck* ID, the BCG sky position ($\alpha_{\rm BCG}$, $\delta_{\rm BCG}$), the photometric

redshift measurement and the redshift lower limit $z_{\mathrm{lim}(10^{15})}$ are presented in Table 2.2. An additional 83 candidates are located so close to the Galactic plane (see Figure 2.1) that we can not reliably assign a redshift or a redshift lower limit due to the high stellar density. For the remaining 94 candidates, we are unable to identify an optical counterpart and we provide only redshift lower limits $z_{\mathrm{lim}(10^{15})}$ that reflect the depths of the catalogue at those candidate locations. This information together with the *Planck* ID is presented for each candidate in Table 2.3.

Nineteen of the confirmed candidates are in *Planck* Class 1 (c.f. § 2.3.1 for the *Planck* classification), whereas there are only three Class 1 candidates remaining in the 94 candidates. This shows that our algorithm has confirmed most of the reliable detections from the *Planck* catalogue. And the three remaining candidates may reside at redshifts beyond our redshift limits where deeper imaging is needed.

Using contamination estimates from the *Planck* collaboration (Planck Collaboration, 2013a) together with the number of total *Planck* candidates and previously confirmed clusters, we estimate that only 45 per cent of our sample (∼110) should be real clusters. If we take our confirmed sample of 60 clusters together with 45 per cent of the 83 candidates lying in fields with high stellar contamination, we have accounted for 98 of our estimates 110 expected real clusters. Thus, these numbers suggest that as many as 12 of our 94 unconfirmed candidates would likely turn out to be real clusters lying at redshifts beyond the redshift lower limits $z_{\mathrm{lim}(10^{15})}$ we present.

Note that because the contamination rate is higher in the *Planck* catalogue in regions of high Galactic dust (Planck Collaboration, 2013a), the number of potentially unconfirmed clusters in the 83 candidates close to the Galactic plane may be less than our estimate. This introduces additional uncertainty into our estimate of the expected number of unconfirmed candidates lying at $z > z_{\mathrm{lim}(10^{15})}$.

Table 2.2: Sky positions and redshifts of *Planck* candidates.

ID	z_{phot}	Δz_{phot}	α_{BCG}	δ_{BCG}	$z_{\mathrm{lim}(10^{15})}$
43	0.077	0.007	253.0509	−0.3377	0.58
59	0.284	0.013	313.5165	−22.8076	0.59
66	0.533	0.250	330.7982	−24.6406	0.55
70	0.284	0.020	257.9357	7.2559	0.62
83	0.425	0.022	344.8704	−25.1154	0.57
111	0.251	0.029	323.2163	−12.5426	0.59
116	0.479	0.037	266.7882	17.1839	0.58
126	0.240	0.021	316.1941	−4.7623	0.56
133	0.229	0.034	273.5555	18.2843	0.57
142	0.360	0.016	219.4179	30.2001	0.72
142*	0.170	0.010	219.4585	30.4253	0.72
143	0.240	0.007	252.5850	26.9726	0.70
149	0.544	0.070	335.0728	−12.1916	0.58
150	0.381	0.031	347.4625	−18.3324	0.57
157	0.218	0.046	359.2370	−22.7796	0.56
209	0.403	0.035	313.2155	17.9064	0.48
212	0.403	0.007	257.6559	40.4314	0.66

* Multiple detections.

Continued.

ID	$z_{\rm phot}$	$\Delta z_{\rm phot}$	$\alpha_{\rm BCG}$	$\delta_{\rm BCG}$	$z_{\rm lim(10^{15})}$
213	0.686	0.133	229.0082	39.7408	0.69
218	0.273	0.034	319.8591	15.3518	0.54
257	0.436	0.054	242.2561	50.0867	0.68
261	0.088	0.007	290.8001	48.2705	0.57
262	0.479	0.022	3.8511	−17.5108	0.64
282	0.316	0.021	324.4442	35.5975	0.40
289	0.099	0.007	300.8065	51.3474	0.49
305	0.207	0.012	352.1669	7.5801	0.61
314	0.262	0.026	257.4693	62.3689	0.64
375	0.099	0.034	283.0395	72.9927	0.64
383	0.360	0.028	284.2933	74.9421	0.64
420	0.229	0.018	0.3115	50.2756	0.45
509	0.284	0.031	140.0173	70.8205	0.60
522	0.077	0.007	27.8319	10.8141	0.64
529	0.110	0.007	99.4772	66.8518	0.51
543	0.131	0.046	129.9560	62.4101	0.50
553	0.349	0.031	100.1444	57.7460	0.54
554	0.305	0.019	36.2339	8.8299	0.60
554*	0.310	0.019	36.1653	8.8983	0.60
575	0.294	0.088	119.3808	52.6829	0.60
576	0.153	0.014	150.4115	50.0149	0.65
612	0.349	0.034	60.7362	9.7414	0.63
618	0.370	0.365	100.7427	31.7503	0.48
679	0.251	0.018	48.8412	−18.2062	0.57
682	0.381	0.036	112.5014	11.9483	0.63
699	0.381	0.086	146.1786	19.4666	0.50
701	0.316	0.045	179.8416	26.4511	0.66
723	0.327	0.027	117.2153	1.1111	0.62
725	0.305	0.028	32.2630	−27.5107	0.58
735	0.131	0.049	78.7192	−19.9555	0.61
736	0.664	0.007	48.7537	−27.3029	0.63
743	0.381	0.066	160.2901	17.5098	0.61
748	0.099	0.007	112.8076	−7.8093	0.68
752	0.294	0.013	120.4230	−4.0614	0.50
778	0.403	0.028	94.7096	−23.5784	0.57
828	0.251	0.044	126.6873	−23.2611	0.53
837	0.436	0.307	131.7742	−21.9784	0.56
860	0.338	0.020	142.9920	−20.6231	0.56
913	0.392	0.067	158.8869	−20.8495	0.57
978	0.327	0.036	175.3720	−21.6974	0.66
1001	0.349	0.025	178.5667	−26.1542	0.57
1080	0.207	0.137	195.4422	−12.0830	0.58
1159	0.055	0.007	201.6415	11.3018	0.64
1178	0.294	0.028	223.1756	−18.5844	0.67

* Multiple detections.

Continued.

ID	$z_{\rm phot}$	$\Delta z_{\rm phot}$	$\alpha_{\rm BCG}$	$\delta_{\rm BCG}$	$z_{\rm lim(10^{15})}$
1189	0.305	0.021	216.3013	−4.9427	0.60
1189*	0.330	0.021	216.3943	−5.0097	0.68

* Multiple detections.

Table 2.3: Unconfirmed *Planck* cluster candidates.

Planck ID	$z_{\rm lim(10^{15})}$	*Planck* ID	$z_{\rm lim(10^{15})}$	*Planck* ID	$z_{\rm lim(10^{15})}$	*Planck* ID	$z_{\rm lim(10^{15})}$
38	0.65	58	0.51	84	0.50	86	0.62
90	0.60	104	0.53	176	0.49	193	0.49
211	0.62	251	0.53	271	0.58	279	0.65
298	0.49	306	0.60	310	0.48	311	0.46
317	0.43	318	0.40	320	0.49	331	0.51
346	0.70	361	0.57	370	0.31	372	0.55
373	0.56	377	0.58	381	0.56	382	0.41
387	0.48	395	0.48	397	0.48	398	0.47
412	0.55	424	0.45	425	0.60	437	0.54
458	0.55	476	0.54	490	0.63	497	0.57
504	0.67	507	0.43	517	0.65	534	0.48
538	0.61	544	0.60	549	0.43	555	0.53
564	0.41	566	0.50	580	0.45	586	0.50
597	0.39	605	0.45	611	0.40	616	0.62
624	0.52	625	0.46	626	0.50	629	0.71
651	0.54	652	0.55	658	0.58	663	0.57
684	0.39	695	0.53	712	0.59	722	0.53
755	0.42	766	0.45	775	0.48	791	0.57
792	0.64	798	0.53	809	0.59	845	0.55
864	0.59	884	0.56	886	0.53	900	0.54
909	0.63	928	0.57	992	0.66	1070	0.61
1122	0.64	1132	0.59	1152	0.56	1171	0.28
1175	0.40	1198	0.60	1199	0.58	1212	0.59
1217	0.61	1221	0.55				

2.6 Conclusions

We study 237 unconfirmed *Planck* cluster candidates that overlap the PS1 footprint. We describe the production of science ready catalogues and present the distribution of measured depths and photometric quality for this ensemble of cluster candidates. We summarise our method for estimating cluster photometric redshifts and describe a method for estimating a redshift lower limit $z_{\rm lim(10^{15})}$ beyond which we would not expect to be able to have confirmed the cluster in the PS1 data. This method uses what we know about SZE selected massive clusters from SPT together with the measured depths of the PS1 catalogues.

Using these data products and methods, we measure photometric redshifts for 60 *Planck* candidates. The newly confirmed clusters span a redshift range $0.06 < z < 0.69$ with a median redshift $z_{\rm med} = 0.31$, which is consistent with the redshift distribution presented for the previously confirmed sample of *Planck* selected clusters. This sample of 60 newly confirmed clusters increases the total number of new, *Planck* discovered clusters from 178 to 238, bringing the total *Planck* cluster sample – including those discovered in previous surveys – to 921 (Planck Collaboration, 2013a).

We exclude 83 of the remaining candidates because of high stellar contamination due to their position close to the Galactic plane. For these systems we cannot obtain reliable photometric redshifts or estimate redshift lower limits with the current data. We are unable to find optical counterparts or estimate photometric redshifts for the last 94 candidates in our sample. For each of these we present a redshift lower limit $z_{\rm lim(10^{15})}$, but the majority of these systems are expected to be noise fluctuations.

Using contamination estimates from the *Planck* collaboration (Planck Collaboration, 2013a) we estimate that ∼12 of the 94 unconfirmed candidates could turn out to be real clusters lying at redshifts beyond the redshift lower limits $z_{\rm lim(10^{15})}$ we present. Confirming these systems will require short exposures on 4-m or 6.5-m class telescopes. Additional *Planck* candidates can be obtained by mining the newly available DES data in the southern celestial hemisphere. The DES depths are adequate to identify the optical counterparts and measure redshifts for high mass clusters out to $z \sim 1.2$ (Hennig et al, in preparation).

Acknowledgments

The Munich group at LMU is supported by the DFG through TR33 “The Dark Universe” and the Cluster of Excellence “Origin and Structure of the Universe”. The data processing has been carried out on the computing facilities of the Computational Center for Particle and Astrophysics (C2PAP), which is supported by the Cluster of Excellence. We want to thank H. H. Head from Austin Peay state university, with whom we initiated this project. Also we would like to thank J. Dietrich and D. C. Gangkofner at LMU for helpful discussions.

The Pan-STARRS1 Surveys (PS1) have been made possible through contributions of the Institute for Astronomy, the University of Hawaii, the Pan-STARRS Project Office, the Max-Planck Society and its participating institutes, the Max Planck Institute for Astronomy, Heidelberg and the Max Planck Institute for Extraterrestrial Physics, Garching, The Johns Hopkins University, Durham University, the University of Edinburgh, Queen’s University Belfast, the Harvard-Smithsonian Center for Astrophysics, the Las Cumbres Observatory Global Telescope Network Incorporated, the National Central University of Taiwan, the Space Telescope Science Institute, the National Aeronautics and Space Administration under Grant No. NNX08AR22G issued through the Planetary Science Division of the NASA Science Mission Directorate, the National Science Foundation under Grant No. AST-1238877, the University of Maryland, and Eotvos Lorand University (ELTE).

Chapter 3

Analysis of Sunyaev-Zel'dovich Effect Mass-Observable Relations using South Pole Telescope Observations of an X-ray Selected Sample of Low Mass Galaxy Clusters and Groups

J. Liu[1,2], J. Mohr[1,2,3], A. Saro[1,2], K. A. Aird[4], M. L. N. Ashby[5], M. Bautz[6], M. Bayliss[7,5], B. A. Benson[8,9,10], L. E. Bleem[9,11,12], S. Bocquet[1,2], M. Brodwin[13], J. E. Carlstrom[9,10,11,12,14], C. L. Chang[9,14,12], I. Chiu[1,2], H. M. Cho[15], A. Clocchiatti[16], T. M. Crawford[9,10], A. T. Crites[9,10,17], T. de Haan[18], S. Desai[1,2], J. P. Dietrich[1,2], M. A. Dobbs[18], R. J. Foley[5,19,20], D. Gangkofner[1,2], E. M. George[21], M. D. Gladders[9,10], A. H. Gonzalez[22], N. W. Halverson[23], C. Hennig[1,2], J. Hlavacek-Larrondo[24,25], G. P. Holder[18], W. L. Holzapfel[21], J. D. Hrubes[4], C. Jones[5], R. Keisler[9,11], A. T. Lee[21,26], E. M. Leitch[9,10], M. Lueker[21,17], D. Luong-Van[4], M. McDonald[6], J. J. McMahon[27], S. S. Meyer[9,14,11,10], L. Mocanu[9,10], S. S. Murray[5], S. Padin[9,10,17], C. Pryke[28], C. L. Reichardt[21,29]A. Rest[30], J. Ruel[7], J. E. Ruhl[31], B. R. Saliwanchik[31], J. T. Sayre[31], K. K. Schaffer[9,14,32], E. Shirokoff[21,17], H. G. Spieler[26], B. Stalder[5], Z. Staniszewski[31,17], A. A. Stark[5], K. Story[9,11], R. Šuhada[1], K. Vanderlinde[33,34], J. D. Vieira[19,20], A. Vikhlinin[5], R. Williamson[9,10,17], O. Zahn[21,35], A. Zenteno[1,36]

[1]Department of Physics, Ludwig-Maximilians-Universität, Scheinerstr. 1, 81679 München, Germany

[2]Excellence Cluster Universe, Boltzmannstr. 2, 85748 Garching, Germany

[3]Max-Planck-Institut für extraterrestrische Physik, Giessenbachstr. 85748 Garching, Germany

[4]University of Chicago, 5640 South Ellis Avenue, Chicago, IL 60637

[5]Harvard-Smithsonian Center for Astrophysics, 60 Garden Street, Cambridge, MA 02138

[7]Department of Physics, Harvard University, 17 Oxford Street, Cambridge, MA 02138

[6]Kavli Institute for Astrophysics and Space Research, Massachusetts Institute of Technology, 77 Massachusetts Avenue, Cambridge, MA 02139

[8]Center for Particle Astrophysics, Fermi National Accelerator Laboratory, Batavia, IL, USA 60510

[9]Kavli Institute for Cosmological Physics, University of Chicago, 5640 South Ellis Avenue,

Chicago, IL 60637
[10]Department of Astronomy and Astrophysics, University of Chicago, 5640 South Ellis Avenue, Chicago, IL 60637
[11]Department of Physics, University of Chicago, 5640 South Ellis Avenue, Chicago, IL 60637
[12]Argonne National Laboratory, 9700 S. Cass Avenue, Argonne, IL, USA 60439
[13]Department of Physics and Astronomy, University of Missouri, 5110 Rockhill Road, Kansas City, MO 64110
[14]Enrico Fermi Institute, University of Chicago, 5640 South Ellis Avenue, Chicago, IL 60637
[15]NIST Quantum Devices Group, 325 Broadway Mailcode 817.03, Boulder, CO, USA 80305
[16]Departamento de Astronomia y Astrosifica, Pontificia Universidad Catolica,Chile
[17]California Institute of Technology, 1200 E. California Blvd., Pasadena, CA 91125
[18]Department of Physics,McGill University, 3600 Rue University, Montreal, Quebec H3A 2T8, Canada
[19]Astronomy Department, University of Illinois at Urbana-Champaign,1002 W. Green Street,Urbana, IL 61801 USA
[20]Department of Physics, University of Illinois Urbana-Champaign,1110 W. Green Street,Urbana, IL 61801 USA
[21]Department of Physics, University of California, Berkeley, CA 94720
[22]Department of Astronomy, University of Florida, Gainesville, FL 32611
[23]Department of Astrophysical and Planetary Sciences and Department of Physics, University of Colorado,Boulder, CO 80309
[24]Kavli Institute for Particle Astrophysics and Cosmology, Stanford University, 452 Lomita Mall, Stanford, CA 94305-4085, USA
[25]Department of Physics, Stanford University, 452 Lomita Mall, Stanford, CA 94305-4085, USA
[26]Physics Division, Lawrence Berkeley National Laboratory, Berkeley, CA 94720
[27]Department of Physics, University of Michigan, 450 Church Street, Ann Arbor, MI, 48109
[28]Physics Department, University of Minnesota, 116 Church Street S.E., Minneapolis, MN 55455
[29]School of Physics, University of Melbourne, Parkville, VIC 3010, Australia
[30]Space Telescope Science Institute, 3700 San Martin Dr., Baltimore, MD 21218
[31]Physics Department, Center for Education and Research in Cosmology and Astrophysics, Case Western Reserve University, Cleveland, OH 44106
[32]Liberal Arts Department, School of the Art Institute of Chicago, 112 S Michigan Ave, Chicago, IL 60603
[33]Dunlap Institute for Astronomy & Astrophysics, University of Toronto, 50 St George St, Toronto, ON, M5S 3H4, Canada
[34]Department of Astronomy & Astrophysics, University of Toronto, 50 St George St, Toronto, ON, M5S 3H4, Canada
[35]Berkeley Center for Cosmological Physics, Department of Physics, University of California, and Lawrence Berkeley National Labs, Berkeley, CA 94720
[36]Cerro Tololo Inter-American Observatory, Casilla 603, La Serena, Chile

This chapter is submitted to MNRAS.

3.1 Abstract

We use 95 GHz, 150 GHz, and 220 GHz observations from the South Pole Telescope (SPT) to examine the Sunyaev-Zel'dovich effect (SZE) signatures of a sample of 46 X-ray selected groups and clusters drawn from ~ 6 deg^2 of the *XMM-Newton* Blanco Cosmology Survey (XMM-BCS). These systems extend to redshift $z = 1.02$, have characteristic masses $\sim 3\times$ lower than clusters detected directly in the SPT data and probe the SZE signal to the lowest X-ray luminosities ($\geq 10^{42}$ erg s^{-1}) yet; these sample characteristics make this analysis complementary to previous studies.

We develop an analysis tool that combines the SZE information for the full ensemble of X-ray-selected clusters. Using X-ray luminosity as a mass proxy, we extract selection-bias corrected constraints on the SZE significance- and Y_{500}-mass relations. The SZE significance-mass relation is in good agreement with an extrapolation of the relation obtained from high mass clusters. However, the fit to the Y_{500}-mass relation at low masses, while in good agreement with the extrapolation from high mass SPT clusters, is in tension at 2.8σ with the constraints from the *Planck* sample. We examine the tension with the *Planck* relation, discussing sample differences and biases that could contribute.

We also present an analysis of the radio galaxy point source population in this ensemble of X-ray selected systems. We find 18 of our systems have 843 MHz Sydney University Molonglo Sky Survey (SUMSS) sources within 2 arcmin of the X-ray centre, and three of these are also detected at significance >4 by SPT. Of these three, two are associated with the group brightest cluster galaxies (BCGs), and the third is likely an unassociated quasar candidate. We examine the impact of these point sources on our SZE scaling relation analyses and find no evidence of biases. We also examine the impact of dusty galaxies using constraints from the 220 GHz data. The stacked sample provides $2.8\,\sigma$ significant evidence of dusty galaxy flux, which would correspond to an average underestimate of the SPT Y_{500} signal that is (17 ± 9) per cent in this sample of low mass systems. Finally, we explore the impact of future data from SPTpol and XMM-XXL, showing that it will lead to a factor of four to five tighter constraints on these SZE mass-observable relations.

3.2 Introduction

The Sunyaev-Zel'dovich effect (Sunyaev & Zel'dovich, 1970, 1972, SZE), is a spectral distortion of the Cosmic Microwave Background (CMB) arising from interactions between CMB photons and hot, ionised gas. Surveys of galaxy clusters using the SZE have opened a new window on the Universe by providing samples of hundreds of massive galaxy clusters with well-understood selection over a broad redshift range. Both space- and ground-based instruments, including the *Planck* satellite (Tauber et al., 2010), the South Pole Telescope (SPT; Carlstrom et al., 2011), and the Atacama Cosmology Telescope (ACT; Fowler et al., 2007), have released catalogs of their SZE selected clusters. The cluster samples have provided new cosmological constraints (Reichardt et al., 2013; Hasselfield et al., 2013; Planck Collaboration, 2013c) and have enabled important evolution studies of cluster galaxies and the intracluster medium over a broad range of redshift (e.g., Zenteno et al., 2011; Semler et al., 2012; McDonald et al., 2013).

Understanding the relationship between the SZE observable and cluster mass is important for both cosmological applications and astrophysical studies. Among observables, the inte-

grated Comptonization from the SZE has been shown by numerical simulations (Motl et al., 2005; Nagai et al., 2007) to be a good mass proxy with low intrinsic scatter. Cluster mass estimates derived from X-ray observations of SZE selected clusters have largely confirmed this expectation (Andersson et al., 2011; Planck Collaboration, 2011). A related quantity, the SPT signal-to-noise ξ, is linked to the underlying virial mass of the cluster by a power law with log-normal scatter at the ~ 20 per cent level (Benson et al., 2013, hereafter B13).

Probing the SZE signature of low mass clusters and groups is also important, although it is much more challenging with the current generation of experiments. These low mass clusters and groups are far more numerous and are presumably important environments for the transformation of galaxies from the field to the cluster. Studies of their baryonic content show that low mass clusters and groups are not simply scaled-down versions of the more massive clusters (e.g., Mohr et al., 1999; Sun et al., 2009; Laganá et al., 2013). This breaking of self-similarity in moving from the cluster to the group mass scale is likely due to processes such as star formation and Active Galactic Nucleus (AGN) feedback.

The *Planck* team has recently studied this low mass population by stacking the *Planck* maps around samples of X-ray selected clusters in the nearby universe (Planck Collaboration, 2011, hereafter P11). They show that the SZE signal is consistent with the self-similar scaling relation based on the X-ray luminosity over a mass range spanning 1.4 orders of magnitude.

Here we pursue a study of the SZE signatures of low mass clusters extending over a broad range of redshift. We use the South Pole Telescope Sunyaev-Zel'dovich survey (SPT-SZ) data with the XMM-BCS over 6 deg^2 from which a sample of 46 X-ray groups and clusters have been selected (Šuhada et al., 2012, hereafter S12). The SPT-SZ data enable us to extract cluster SZE signal with high angular resolution and low instrument noise, making the most of this small sample.

The paper is organised as follows. In § 3.3, we describe the data used from the XMM-BCS and the extraction of the SZE signature from the SPT-SZ maps. In § 3.4, we introduce the calibration method for the mass-observable scaling relation, and we apply it to the cluster sample in § 3.5. We also discuss possible systematic effects and present a discussion of the point source population associated with our sample. We conclude in § 3.6 with a prediction of the improvement based on future surveys.

The cosmological model parameters adopted in this paper are the same as the ones used for the X-ray measurement from the XMM-BCS project (S12): $(\Omega_{\rm M}, \Omega_\Lambda, H_0) = (0.3, 0.7, 70\,{\rm km\ s^{-1}Mpc^{-1}})$. The amplitude of the matter power spectrum, which is needed to estimate bias corrections in the analysis, is fixed to $\sigma_8 = 0.8$.

3.3 Data Description and Observables

In this analysis, we adopt an X-ray selected sample of clusters, described in § 3.3.1, together with published $L_{\rm X}$-mass scaling relations to examine the corresponding SPT-SZ significance- and Y_{500}-mass relations. The SPT-SZ observable ξ is measured by a matched filter approach, which we discuss in § 3.3.2 and § 3.3.3. The estimation of Y_{500} is described in § 3.3.4.

3.3.1 X-ray Catalog

The XMM-BCS project consists of an X-ray survey mapping 14 deg^2 area of the southern hemisphere sky that overlaps the *griz* bands Blanco Cosmology Survey (Desai et al., 2012, BCS) and the mm-wavelength SPT-SZ survey (Carlstrom et al., 2011). S12 analyse the initial

6 deg^2 core area, construct a catalog of 46 galaxy clusters and present a simple selection function. Here we present a brief summary of the characteristics of that sample. The cluster physical parameters from Table 2 (S12) are repeated in Table 3.4 with the same IDs.

The initial cluster sample was selected via a source detection pipeline in the 0.5–2 keV band. The spatial extent of the clusters leads to the need to have more counts to reach a certain detection threshold than are needed for point sources. S12 modelled the extended source sensitivity as an offset from the point source limit; the cluster sample is approximately a flux-limited sample with $f_{\rm min} = 1 \times 10^{-14}$erg s^{-1}cm^{-2}.

The X-ray luminosity $L_{\rm X}$ was measured in the detection band (0.5–2.0 keV) within a radius of θ_{500}, which is iteratively determined using mass estimates from the $L_{\rm X}$-mass relation and is defined such that the interior density is 500 times the critical density of the Universe at the corresponding redshift. This luminosity was converted to a bolometric luminosity and to a 0.1–2.4 keV band luminosity using the characteristic temperature for a cluster with this 0.5–2.0 keV luminosity and redshift. The core radius, $R_{\rm c}$, of the beta model is calculated using (see equation 1 in S12):

$$R_{\rm c} = 0.07 \times R_{500} \Big(\frac{T}{1 \text{ keV}} \Big)^{0.63}, \tag{3.1}$$

where T is X-ray temperature determined through the $L_{\rm X} - T$ relation. The redshifts of the sample are primarily photometric redshifts extracted using the BCS optical imaging data. The optical data and their processing and calibration are described in detail elsewhere (Desai et al., 2012). The photometric redshift estimator has been demonstrated on clusters with spectroscopic redshifts and on simulations (Song et al., 2012a) and has been used for redshift estimation within the SPT-SZ collaboration (Song et al., 2012b). The typical photometric redshift uncertainty in this XMM-BCS sample is $\langle \Delta z/(1+z) \rangle = 0.023$, which is determined using a subsample of 12 clusters ($z < 0.4$) with spectroscopic redshifts. This value is consistent with the uncertainty $\langle \Delta z/(1+z) \rangle = 0.017$ we obtained on the more massive main sample SPT-SZ clusters.

The X-ray luminosities and photometric redshifts of the sample are shown in Figure 3.1 in black squares and the approximate flux limit of the sample is shown as a red curve. For comparison, we also include a high mass SPT-SZ cluster sample (blue triangles) with published X-ray properties (Andersson et al., 2011).

In the analysis that follows we use the X-ray luminosity as the primary mass estimator for each cluster. We adopt the $L_{\rm X}$-mass scaling relation used in S12, which is based on the hydrostatic mass measurements in an ensemble of 31 nearby clusters observed with *XMM-Newton* (REXCESS, Pratt et al., 2009):

$$L_{\rm X} = L_0 \Big(\frac{M_{500{\rm c}}}{2 \times 10^{14} M_\odot} \Big)^{\alpha_{\rm LM}} E(z)^{7/3}, \tag{3.2}$$

where $H(z) = H_0 E(z)$. The intrinsic scatter in $L_{\rm X}$ at fixed mass is modelled as lognormal distributions with widths $\sigma_{L_{\rm X}}$, and the observational scatter is given in S12.

This scaling relation includes corrections for Malmquist and Eddington biases. Both biases are affected by the intrinsic scatter and the skewness of the underlying sample distribution. In general, the bias on the true mass is $\Delta \ln M \propto \gamma \sigma^2_{\ln M}$, where ${\rm d}n(M)/{\rm d}\ln M \propto M^\gamma$ is the slope of the mass distribution and $\sigma_{\ln M}$ is the scatter in mass at fixed observable (for more discussion, we refer the reader to Stanek et al., 2006; Vikhlinin et al., 2009a; Mortonson et al.,

Table 3.1: $L_{\rm X}$-mass relations with different luminosity bands (Equation (3.2)).

Type	$L_0[10^{44}\mathrm{erg\ s^{-1}}]$	$\alpha_{\rm LM}$	$\sigma_{\ln L_{\rm X}}$
0.5–2.0 keV	0.48 ± 0.04	1.83 ± 0.14	0.412 ± 0.071
0.1–2.4 keV	0.78 ± 0.07	1.83 ± 0.14	0.414 ± 0.071
Bolometric	1.38 ± 0.12	2.08 ± 0.13	0.383 ± 0.061

2011). Typically γ is negative, and the result is that mass inferred from an observable must be corrected to a lower value than that suggested by naive application of the scaling relation.

The scaling relation parameters for different X-ray bands are listed in Table 3.1. We find the choice of luminosity bands has negligible impact on the parameter estimation given the current constraint precision. In addition, we investigate using the $L_{\rm X}$-mass scaling relations from *Chandra* observations (Vikhlinin et al., 2009a; Mantz et al., 2010a). These studies draw upon higher mass cluster samples than the REXCESS sample, and therefore we adopt the Pratt et al. (2009) relation for our primary analysis. We discuss the impact of changing the $L_{\rm X}$-mass scaling relation in § 3.5.3.

3.3.2 SPT Observations

The SPT (Carlstrom et al., 2011) is a 10-metre diameter, millimetre-wavelength, wide field telescope that was deployed in 2007 and has been used since then to make arcminute-resolution observations of the CMB over large areas of the sky. The high angular resolution is crucial to detecting the SZE signal from high-redshift clusters. The SPT-SZ survey (e.g., Story et al., 2013), completed in 2011, covers a 2500 deg^2 region of contiguous sky area in three bands – centred at 95, 150, and 220 GHz – at a typical noise level of $< 18\mu$K per one-arcminute pixel in the 150 GHz band.

The details of the SPT-SZ observation strategy, data processing and mapmaking are documented in Schaffer et al. (2011); we briefly summarise them here. The SPT-SZ survey data were taken primarily in a raster pattern with azimuth scans at discrete elevation steps. A high-pass filter was applied to the time-ordered data to remove low-frequency atmospheric and instrumental noise. The beams, or angular response functions, were measured using observations of planets and bright AGNs in the field. The main lobe of the beam for a field observation is well-approximated as a Gaussian with a Full Width Half Maximum (FWHM) of 1.6, 1.2, and 1.0 arcmin at 95, 150, and 220 GHz, respectively. The final temperature map was calibrated by the Galactic H II regions RCW38 and MAT5a (c.f. Vanderlinde et al., 2010). The SPT-SZ maps used in this work are from a 100 deg^2 field centred at $(\alpha, \delta) = (23^\circ\ 30', -55^\circ)$ and consist of observations from the 2008 and 2010 SPT-SZ observing seasons. The characteristic depths are 37, 12 and 35 μK-arcmin at 95, 150 and 220 GHz, respectively.

3.3.3 SPT-SZ Cluster Significance

The process of determining the SPT-SZ significance for our X-ray sample is very similar to the process of finding clusters in SPT-SZ maps, but there are certain key differences, which we highlight below. Clusters of galaxies are extracted from SPT-SZ maps through their distinct angular scale- and frequency-dependent imprint on the CMB. We adopt the multi-frequency matched filter approach (Melin et al., 2006) to extract the cluster signal. The matched filter

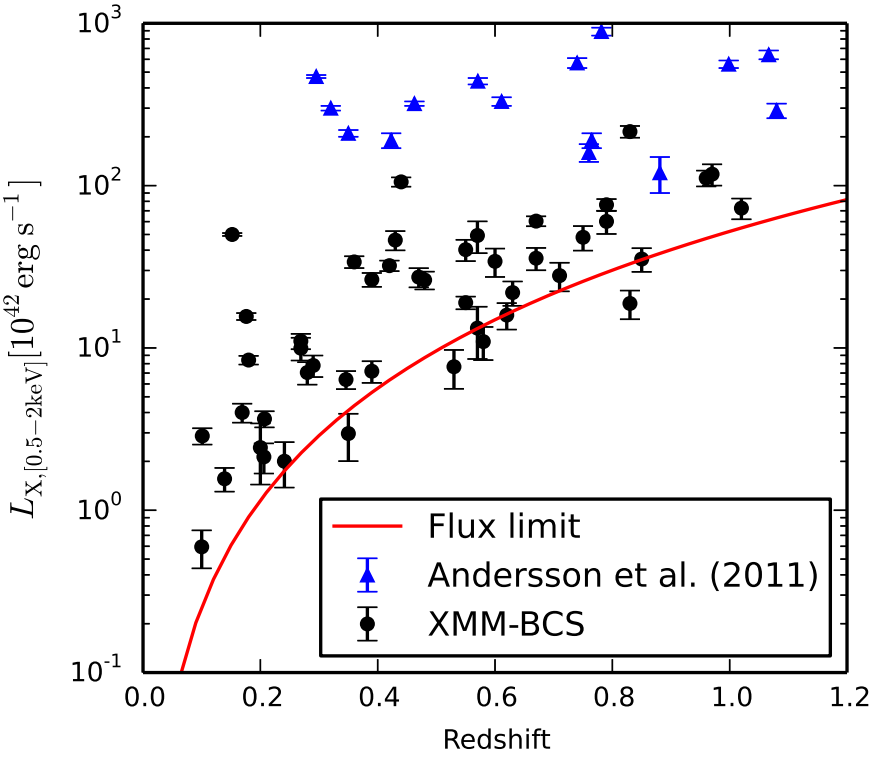

Figure 3.1: The luminosity-redshift distribution of the XMM-BCS clusters from S12 (black dots) and the SPT-SZ clusters from Andersson et al. (2011, blue triangles). The X-ray sample is selected with a flux cut that varies somewhat across the field. The red line is the corresponding luminosity sensitivity determined by the median flux limit in the 0.5 - 2.0 keV band. The SPT-SZ sample is more massive and approximately mass limited.

is designed to maximise the given signal profile while suppressing all noise sources. A detailed description appears elsewhere (Vanderlinde et al., 2010; Williamson et al., 2011). Here we provide a summary. The SZE introduces a spectral distortion of the CMB at given frequency ν as:

$$\Delta T_{\rm CMB}(\boldsymbol{\theta}, \nu) = y(\boldsymbol{\theta}) g(\nu) T_{\rm CMB}, \tag{3.3}$$

where $g(\nu)$ is the frequency dependency and the Compton-y parameter $y(\boldsymbol{\theta})$ is the SZE signature at direction $\boldsymbol{\theta}$, which is linearly related to the integrated pressure along the line-of-sight. To model the SZE signal $y(\boldsymbol{\theta})$, two common templates are adopted: the circular β model (Cavaliere & Fusco-Femiano, 1976) and the Arnaud profile (Arnaud et al., 2010). The cluster profiles are convolved with the SPT beams to get the expected signal profiles. The map noise assumed in constructing the filter includes the measured instrumental and atmospheric noise and sources of astrophysical noise, including the primary CMB. Point sources are identified in a similar manner within each band independently, using only the instrument beams as the source profile (Vieira et al., 2010).

Once SPT-SZ maps have been convolved with the multi-frequency matched filter, clusters are extracted with a simple peak-finding algorithm, with the primary observable ξ defined

as the maximum signal-to-noise of a given peak across a range of filter scales. The SPT-SZ significance ξ is a biased estimator that links to the underlying ζ as $\langle\xi\rangle = \sqrt{\zeta^2 + 3}$, because it is the maximum value identified through a search in sky position and filter angular scale (Vanderlinde et al., 2010). The observational scatter of ξ around ζ is a unit-width Gaussian distribution corresponding to the underlying RMS noise of the SPT-SZ filtered maps.

In this work, we use the same method to define an SPT-SZ significance for each X-ray selected cluster, but with two important differences: 1) We measure the SPT-SZ significance at the X-ray location, and 2) we use a cluster profile shape informed from the X-ray data. We define this SPT-SZ significance as $\xi_{\rm X}$, which is related to the unbiased SPT-SZ significance ζ as:

$$\zeta = \langle\xi_{\rm X}\rangle, \tag{3.4}$$

where the angle brackets denote the average over many realizations of the experiment. The observational scatter of $\xi_{\rm X}$ around ζ is also a unit-width Gaussian distribution. Therefore $\xi_{\rm X}$ is an unbiased estimator of ζ, under the assumption that the true X-ray position and profile are identical to the true SZE position and profile – a reasonable assumption – given that both the X-ray and the SZE signatures are reflecting the intracluster medium properties of the clusters. Note, however, that in the midst of a major merger the different density weighting of the X-ray and SZE signatures can lead to offsets (Molnar et al., 2012).

We model the relationship between ζ and the cluster mass through

$$\zeta = A_{\rm SZ}^{\rm SPT}\Big(\frac{M_{\rm 500c}}{4.3\times10^{14}M_{\odot}}\Big)^{B_{\rm SZ}}\Big[\frac{E(z)}{E(0.6)}\Big]^{C_{\rm SZ}}, \tag{3.5}$$

where the intrinsic scatter on ζ is described by a log-normal distribution of width $D_{\rm SZ}$ (B13; Reichardt et al., 2013). We use $A_{\rm SZ}^{\rm SPT}$ to denote the amplitude of the original SPT-SZ scaling relation. The differences in the depths of the SPT-SZ fields results in a re-scaling of the SPT-SZ cluster significance in spatially filtered maps. For the field we study here, the relation requires a factor of 1.38 larger normalisation compared to the value in Reichardt et al. (2013).

For the massive SPT-SZ clusters (with $\xi > 4.5$), the ζ-mass relation is best parametrized as shown in Table 3.2 with $C_{\rm SZ} = 0.83 \pm 0.30$ and $D_{\rm SZ} = 0.21 \pm 0.09$ (B13). In our analysis, we examine the characteristics of the lower mass clusters within the SPT-SZ survey. To avoid a degeneracy between the scaling relation amplitude and slope, we shift the pivot mass to $1.5 \times 10^{14}\ M_{\odot}$, near the median mass of our sample and term the associated amplitude $A_{\rm SZ}$. At this pivot mass, with the normalisation factor mentioned previously, the equivalent amplitude parameter for the main SPT-SZ sample corresponds to $A_{\rm SZ} = 1.50$. In Table 3.2 we also note the priors we adopt in our analysis of the low mass sample. For our primary analysis we adopt flat priors on the amplitude and slope parameters and fix the redshift evolution and scatter at the values obtained by B13.

3.3.4 Integrated Y_{500}

To facilitate the comparison of our sample with cluster physical properties reported in the literature, we also convert the $\xi_{\rm X}$ to Y_{500}, which is the integration of the Compton-y parameter within a spherical volume with radius θ_{500}. The central y_0 is linearly linked to $\xi_{\rm X}$ in the matched filter approach (Melin et al., 2006), with the corresponding Arnaud profile or β profile as the cluster template. The characteristic radii (θ_{500} and $R_{\rm c}$) are based on the X-ray measurements (S12), because the SZE observations are too noisy to constrain the profile accurately.

The projected circular β profile for the filter is:

$$y_{\rm cyl}^{(\beta)}(r) \propto (1 - r^2/R_{\rm c}^2)^{-(3\beta-1)/2}, \tag{3.6}$$

where β is fixed to 1, consistent with higher signal to noise cluster studies (Plagge et al., 2010). And the spherical Y_{500} within the θ_{500} is

$$Y_{500}^{(\beta)} = y_0 \times \pi R_{\rm c}^2 \ln(1 + \theta_{500}^2/R_{\rm c}^2) \times f(\theta_{500}/R_{\rm c}), \tag{3.7}$$

where $f(x)$ corrects the cylindrical result to the spherical value for the β profile as:

$$f(x) = 2\frac{\ln(x + \sqrt{1+x^2}) - x/\sqrt{1+x^2}}{\ln(1+x^2)}. \tag{3.8}$$

The $Y_{500}^{\rm (A)}$ for the Arnaud profile is calculated similarly except that the projected profile is calculated numerically within $5\theta_{500}$ along the line-of-sight direction:

$$y_{\rm cyl}^{\rm (A)}(r) \propto \int_{-5\theta_{500}}^{5\theta_{500}} P\Big(\frac{\sqrt{r^2+z^2}}{\theta_{500}}\Big) {\rm d}z, \tag{3.9}$$

where the pressure profile has the form

$$P(x) \propto (c_{500}x)^{-\gamma_{\rm A}}[1 + (c_{500}x)^{\alpha_{\rm A}}]^{(\gamma_{\rm A}-\beta_{\rm A})/\alpha_{\rm A}}, \tag{3.10}$$

with $[c_{500}, \gamma_{\rm A}, \alpha_{\rm A}, \beta_{\rm A}] = [1.177, 0.3081, 1.0510, 5.4905]$ (Arnaud et al., 2010). The integration up to $5\theta_{500}$ includes more than 99 per cent of the total pressure contribution. The spherical Y_{500} for the Arnaud profile is:

$$Y_{500}^{\rm (A)} = 2\pi y_0 \int_0^{R_{500c}} y_{\rm cyl}^{\rm (A)}(r) r {\rm d}r / 1.203, \tag{3.11}$$

where the numerical factor 1.203 is the ratio between cylindrical integration and spherical integration for the adopted Arnaud profile parameters.

Measurements of Y_{500} are sensitive to the assumed profile. The Arnaud profile depends only on θ_{500}, while the β profile depends on both θ_{500} and $R_{\rm c}$ and therefore Y_{500} is sensitive to the ratio $R_{\rm c}/\theta_{500}$. We find that with $R_{\rm c}/\theta_{500} = 0.2$ the β and Arnaud profiles provide Y_{500} measurements in good agreement; this ratio is consistent with the previous SZE profile study using high mass clusters (Plagge et al., 2010). Interestingly, the X-ray data indicate a characteristic ratio of 0.11 ± 0.03 for our sample, and a shift in the $R_{\rm c}/\theta_{500}$ ratio from 0.2 to 0.1 leads to a $\sim$40 per cent decrease in Y_{500}. Given that the *Planck* analysis to which we compare is carried out using the Arnaud profile, we adopt that profile for the analysis in Section 3.5.4 below.

The Y_{500}-mass scaling relation has been modelled using a representative local X-ray cluster sample (Arnaud et al., 2010) and further studied in the SZE (Andersson et al., 2011, P11) as

$$Y_{500} = A_{\rm Y}\Big(\frac{M_{500}}{1.5\times10^{14}M_\odot}\Big)^{B_{\rm Y}} E(z)^{2/3}\Big[\frac{D_{\rm A}(z)}{500{\rm Mpc}}\Big]^{-2}, \tag{3.12}$$

where $D_{\rm A}(z)$ is the angular-diameter distance and the intrinsic scatter on Y_{500} is described by a log-normal distribution of width $\sigma_{\log {\rm Y}} = 0.21$. The observational scatter of Y_{500} is propagated from the scatter of $\xi_{\rm X}$. In § 3.5, we fit this relation to the observations.

3.4 Method

In this section, we describe the method we developed to fit the SZE-mass scaling relations of the low mass cluster population selected through the XMM-BCS and observed by the SPT. In principle, we could use our cluster sample observed in X-ray and SZE to simultaneously constrain the cosmology and the scaling relations, in the so-called self-calibration approach (Majumdar & Mohr, 2004). However, self-calibration requires a large sample. Without this, we take advantage of strong, existing cosmology constraints (e.g., Planck Collaboration, 2013b; Bocquet et al., 2014) and knowledge of the $L_{\rm X}$-mass scaling relation (e.g. Pratt et al., 2009). We focus only on the SZE-mass scaling relations, exploring the SZE characteristics of low mass galaxy clusters and groups. In § 3.4.1 we present the method and in § 3.4.2 we validate it using mock catalogs.

3.4.1 Description of the Method

The selection biases on scaling relations include the Malmquist bias and the Eddington bias, which are manifestations of scatter and population variations associated with the selection observable. Several methods have previously been developed (e.g., Vikhlinin et al. 2009a; Mantz et al. 2010b; B13; Bocquet et al. 2014) to account for the sampling biases when fitting scaling relation and cosmological parameters simultaneously. In this analysis, we use a likelihood function that can be derived from the one presented in B13. For a detailed discussion we refer the reader to Appendix 3.7.1; here we present an overview of the key elements of this likelihood function.

The likelihood function $\mathcal{L}(\boldsymbol{r}_{\rm SZ})$ we use to constrain the SZE-mass relations is the product of the individual conditional probabilities to observe each cluster with SZE observable Y_i (e.g., SPT-SZ significance $\xi_{\rm X}$ or Y_{500}), given the cluster has been observed to have an X-ray observable L_i and redshift z_i:

$$\mathcal{L}(\boldsymbol{r}_{\rm SZ}) = \Pi_i \; P(Y_i|L_i, z_i, \boldsymbol{c}, \boldsymbol{r}_{\rm X}, \boldsymbol{r}_{\rm SZ}, \Theta_{\rm X}), \tag{3.13}$$

where i runs over the cluster sample, $\boldsymbol{r}_{\rm SZ}$ contains the parameters describing the SZE mass-observable scaling relation that we wish to study, $\boldsymbol{c}$ contains the cosmological parameters, $\boldsymbol{r}_{\rm X}$ contains the parameters describing the X-ray mass-observable scaling relation, and the survey selection in X-ray is encoded within $\Theta_{\rm X}$. Note that the redshifts are assumed to be accurate such that the X-ray luminosity ($L_{\rm X}$) is used instead of the true survey selection observable, which is the X-ray flux.

As noted above, given the size of our dataset we adopt fixed cosmology $\boldsymbol{c}$ and X-ray scaling relation parameters $\boldsymbol{r}_{\rm X}$ to focus on the SZE-mass scaling relation. In § 3.5 we examine the sensitivity of our results to the current uncertainties in cosmology and the X-ray scaling relation and find them to be unimportant for our analysis. Within this context, the conditional probability density function for cluster i can be written as the ratio of the expected number of clusters $\mathrm{d}N$ with observables Y_i, L_i and z_i within infinitesimal volumes $\mathrm{d}Y$, $\mathrm{d}L$ and $\mathrm{d}z$:

$$P(Y_i|L_i, z_i, \boldsymbol{r}_{\rm SZ}, \Theta_{\rm X}) = \frac{\mathrm{d}N(Y_i, L_i, z_i|\boldsymbol{r}_{\rm SZ}, \Theta_{\rm X})}{\mathrm{d}N(L_i, z_i|\Theta_{\rm X})}, \tag{3.14}$$

where we have dropped the cosmology $\boldsymbol{c}$ and X-ray scaling relation parameters $\boldsymbol{r}_{\rm X}$ because they are held constant. Typically, the survey selection $\Theta_{\rm X}$ is a complex function of the redshift and X-ray flux, but in the above expression it is simply the probability that a

cluster with X-ray luminosity L_i and redshift z_i is observed (i.e. $\mathrm{d}N\left(Y_i, L_i, z_i|\boldsymbol{r}_{\mathrm{SZ}}, \Theta_{\mathrm{X}}\right) = \Theta_{\mathrm{X}}(L_i, z_i)\mathrm{d}N(Y_i, L_i, z_i|\boldsymbol{r}_{\mathrm{SZ}})$); in Equation (3.14) this same factor appears in both the numerator and denominator, and therefore it cancels out. Thus, studying the SZE properties of an X-ray selected sample does not require detailed modelling of the selection. If the selection were based on both L and Y, then there would be no cancellation, because the selection probability in the numerator would be just $\Theta(L_i, Y_i, z_i)$ while in the denominator it would have to be marginalised over the unobserved Y as $\int \Theta(Y, L_i, z_i)\mathrm{d}Y$ (see Equation (3.27)).

With knowledge of the cosmologically dependent mass function $n(M, z) \equiv \mathrm{d}N(M, z|\boldsymbol{c})/\mathrm{d}M\mathrm{d}z$ (Tinker et al., 2008), the ratio of the expected number of clusters can be written as:

$$P(Y_i|L_i, z_i, \boldsymbol{r}_{\mathrm{SZ}}) = \frac{\int \mathrm{d}M P(Y_i, L_i|M, z_i, \boldsymbol{r}_{\mathrm{SZ}})\, n(M, z_i)}{\int \mathrm{d}M P(L_i|M, z_i)\, n(M, z_i)}. \tag{3.15}$$

We emphasise that there is a residual dependence on the X-ray selection in our analysis in the sense that we can only study the SZE properties of the clusters that have sufficient X-ray luminosity to have made it into the sample. This effectively limits the mass range over which we can use the X-ray selected sample to study the SZE properties of the clusters.

To constrain the scaling relation in the presence of both observational uncertainties and intrinsic scatter, we further expand the conditional probability density functions in Equation (3.15):

$$\begin{aligned} P(Y_i, L_i|M, z_i, \boldsymbol{r}_{\mathrm{SZ}}) = \iint \mathrm{d}Y_{\mathrm{t}}\mathrm{d}L_{\mathrm{t}}\ & P(Y_i, L_i|Y_{\mathrm{t}}, L_{\mathrm{t}}) \\ & \times P(Y_{\mathrm{t}}, L_{\mathrm{t}}|M, z_i, \boldsymbol{r}_{\mathrm{SZ}}), \end{aligned} \tag{3.16}$$

$$P(L_i|M, z_i) = \int \mathrm{d}L_{\mathrm{t}}\ P(L|L_{\mathrm{t}})P(L_{\mathrm{t}}|M, z_i), \tag{3.17}$$

where, as above, Y_i and L_i are the observed values, and Y_{t} and L_{t} are the true underlying observables related to mass through scaling relations that have intrinsic scatter. The first factor in each integral represents the measurement error, and the second factor describes the relationship between the pristine observables and the halo mass. Improved data quality affects the first factor, but cluster physics dictates the form of the second. These second factors are fully described by the power law mass-observable relations in Equations (3.2), (3.5), and (3.12) together with the adopted log-normal scatter.

We use this likelihood function under the assumption that there is no correlated scatter in the observables; in § 3.4.2 we use mock samples that include correlated scatter to examine the impact on our results.

3.4.2 Validation with Mock Cluster Catalogs

We use mock samples of clusters to validate our likelihood and fitting approach and to explore our ability to constrain different parameters. Specifically, we generate ten larger mock surveys of 60 deg^2, with a similar flux limit of 1×10^{-14}erg s^{-1}cm^2 and $z > 0.2$. Each mock catalog contains ~ 400 clusters, or approximately eight times as many as in the observed sample. The ξ_{X} of the sample spans $-2.2 \leq \xi_{\mathrm{X}} \leq 7.8$ with a median value of 1.4. We include both the intrinsic scatter and observational uncertainties for both the L_{X} and the ξ_{X} in the mock catalog. The intrinsic scatter is lognormal distributed with values given as $\sigma_{\ln L_{\mathrm{X}}}$ (D_{SZ}). The observational uncertainties in L_{X} and ξ_{X} are modelled as normal distributions. The standard

deviation used for $L_{\rm X}$ is proportional to $\sqrt{L_{\rm X}}$ to mimic the Poisson distribution of photon counts, while the standard deviation for $\xi_{\rm X}$ is 1.

Here we focus on recovering the four SPT-SZ ζ-mass relation parameters from the mock catalog; the fiducial values for these parameters are the B13 best-fitting values. We scan through the parameter space using a fixed grid. The following results contain 41 bins in each parameter direction. Given the limited constraining power, we validate the parameters using two different sets of priors. In the first set we adopt flat priors on $A_{\rm SZ}$, $B_{\rm SZ}$, and $C_{\rm SZ}$ with fixed $D_{\rm SZ}$. In the second set we adopt flat positive priors on $A_{\rm SZ}$, $B_{\rm SZ}$, and $D_{\rm SZ}$ with fixed $C_{\rm SZ}$. All other relevant parameters are fixed, including the $L_{\rm X}$-mass scaling and the cosmological model.

Our tests show good performance of the method. Using ten mock samples that are each ten times larger than our observed sample, and fitting for 3 parameters in each mock, we recover the parameters to within the marginalised $1\,\sigma$ statistical uncertainty 70 per cent of the time and to within $2\,\sigma$ for the rest. Figure 3.2 illustrates our ζ-mass parameter constraints from one mock sample. Note that the constraints on $C_{\rm SZ}$ and $D_{\rm SZ}$ are both weak and exhibit no significant degeneracy with the other two SPT-SZ scaling parameters. We take this as motivation to fix $C_{\rm SZ}$ and $D_{\rm SZ}$ and focus on the amplitude $A_{\rm SZ}$ and slope $B_{\rm SZ}$ in the analysis of the observed sample. We have repeated this testing in the case of the Y_{500}-mass relation, and we see no difference in behavior.

We also investigate the sensitivity of our method when a correlation between intrinsic scatter in the X-ray and $\xi_{\rm X}$ is included. Cluster observables can be correlated through an analysis approach. For example, if one uses the $L_{\rm X}$ as a virial mass estimate, then when $L_{\rm X}$ scatters up by 40 per cent, it leads to a 5 per cent increase in radius, and 8 per cent increase in Y_{500} if the underlying SZE brightness distribution is described by the Arnaud et al. (2010) profile. In comparison, the intrinsic scatter of Y_{500} about mass is about 20 per cent, which in this example would still dominate over the correlated component of the scatter. Correlated scatter in different observable-mass relations can also reflect underlying physical properties of the cluster that impact the two observables in a similar manner.

We find that even with a correlation coefficient $\rho = 0.5$ between the intrinsic scatter of the two observables, the change in constraints extracted using a no correlation assumption is small. Thus, our approximation does not lead to significant bias in the analysis of this sample. This result is also consistent with the fact that by extending Equations (3.16) and (3.17) to include multi-dimensional log-normal scatter distributions, we find the constraint on correlated scatter in the mock catalog to be very weak. We therefore do not include the possibility of correlated scatter when studying the real sample.

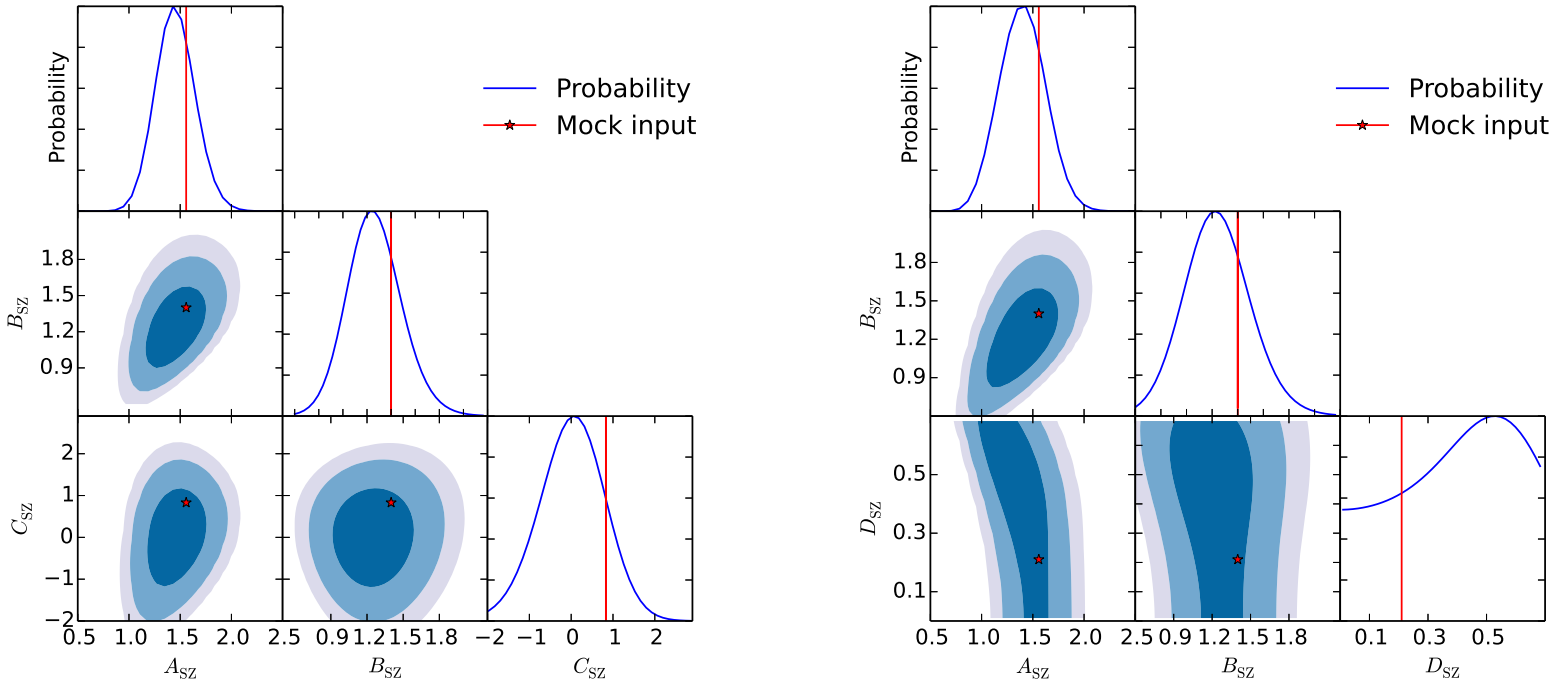

Figure 3.2: Constraints on the ζ-mass relation from an analysis of the mock catalog. The left panel constrains A_{SZ}, B_{SZ}, and C_{SZ} with fixed D_{SZ}. And the right panel shows the result by fixing C_{SZ} instead of D_{SZ}. The red lines and stars denote the input values of the scaling relation parameters of the mock catalog. Histograms in each case show the recovered projected likelihood distribution for each parameter. Joint constraints for different pairs of parameters are shown in blue with different shades indicating the 1, 2, and $3\,\sigma$ levels.

3.5 Results

In this section, we present the observed relationship between the SZE significance ξ_X at the position of the X-ray selected cluster and the predicted value given the measured X-ray luminosity of the system. Thereafter, we test – and rule out – the null hypothesis that the SZE signal at the locations of the X-ray selected clusters is consistent with noise. We then present constraints on the SPT-SZ ζ-mass and Y_{500}-mass relations. We end with a discussion of possible systematics and a presentation of the point source population for this X-ray selected group and cluster sample.

3.5.1 SPT Significance Extraction

We extract the ξ_X from the SPT-SZ multi-frequency-filtered map at the location of each XMM-BCS selected cluster as described in § 3.3. In the primary analysis, we adopt three matched-filtered maps from the SPT-SZ data, one each for β-model profiles with $R_c = 0.25$, 0.5, and 0.75 arcmin, and we extract the value of ξ_X for each cluster from the map that most closely matches the X-ray-derived R_c value for that cluster. The ξ_X is extracted at the X-ray-derived cluster position. The measured ξ_X values are presented in Table 3.4. We have also tried extracting SPT-SZ significance by making a matched-filtered map for every cluster, using a filter with the exact X-ray-derived value of R_c, and the change in the results is negligible.

We have also investigated the dependence of ξ_X on the assumed cluster profile. We repeated the analysis described above using the Arnaud profile and a β profile with $\beta = 2/3$. The resulting changes in the extracted values of ξ_X are less than 3 per cent of the measurement uncertainty on the individual ξ_X values. A similar lack of sensitivity to the assumed cluster profile is seen in the $\xi > 5$ SPT-SZ derived cluster samples.

The cluster with the strongest detection in the SPT-SZ maps is illustrated in Figure 3.3, which contains a pseudo-colour optical image with SPT-SZ signal-to-noise contours in white. The SPT-SZ significance, ξ, of this cluster is 6.23 corresponding to maximum signal-to-noise in the filtered map (SPT-CLJ2316-5453, Bleem et al. in prep.), whereas the ξ_X is 4.58 at the X-ray position with R_c of 0.367 arcmin. This reduction in signal to noise is expected because there is noise in the SZE map, and the SPT-SZ cluster is selected to lie at the peak ξ.

3.5.2 Testing the Null Hypothesis

To gain a sense of the strength of the SZE detection of the ensemble of XMM-BCS clusters, we test the measured significance around SZE null positions. This null catalog consists of the same number of clusters as the XMM-BCS sample where the X-ray luminosities and redshifts are maintained, but the SPT-SZ significances ξ_X are measured at random positions. We then carry out a likelihood analysis of this null catalog. When fixing the slope B_{SZ} of the scaling relation, we find that the normalisation factor A_{SZ} is constrained to be < 0.56 at 99 per cent confidence level for the null sample. Because this constraint on the amplitude is small compared to the expected normalisation for the XMM-BCS sample, we have essentially shown that there should be sufficient signal to noise to detect the SZE signature of the cluster ensemble.

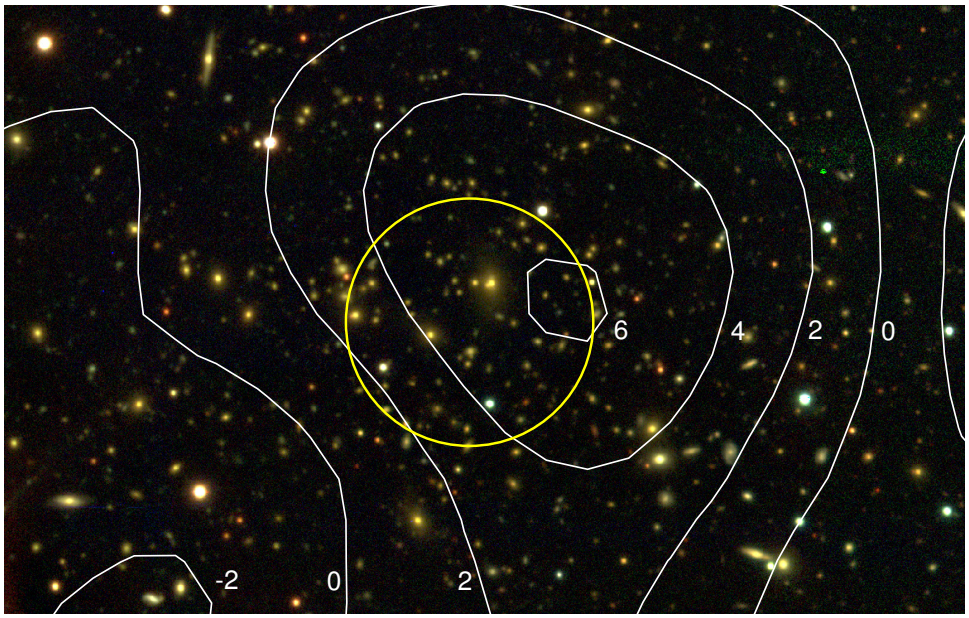

Figure 3.3: BCS optical pseudo-colour image of cluster 044 in *gri* bands. The yellow circle (1.5 arcmin diameter) centred at the X-ray peak indicates the rough size of the SPT beam (1.2 arcmin FWHM in 150 GHz and 1.6 arcmin in 95 GHz). The SPT-SZ filtered map is overlaid with white contours, which are marked with the significance levels. The offset between the X-ray centre and the SZE peak is 0.75 arcmin, and the BCG for this system lies near those two centres.

3.5.3 SPT ζ-mass Relation

We explore the SZE signature of low mass clusters by constraining the $A_{\rm SZ}$ and $B_{\rm SZ}$ parameters with the approach described and tested above. The X-ray luminosity-mass scaling relation, Equation (3.2), is directly adopted with the additional observational uncertainties of each cluster that are listed in Table 3.4 (bolometric luminosities presented in S12).

We present results for four different subsets of our sample: 1) the full sample without removal of any cluster; 2) the sample excluding any cluster with a point source detected at $>4\,\sigma$ in any SPT observing band within a 4 arcmin radius of the X-ray cluster (see Table 3.4), hereafter SPT-NPS sample; 3) the SPT-NPS clusters with redshift larger than 0.3, hereafter SPT-NPS($z > 0.3$), which is the best match to the selection of the SPT-SZ high mass sample in B13 and 4) the sample without any Sydney University Molonglo Sky Survey (SUMSS, Bock et al., 1999; Mauch et al., 2003) point sources in 4 arcmin radius. We discuss further the astrophysical nature and impact of point sources in § 3.5.6.

In Figure 3.4, we illustrate the ζ-mass relation obtained by plotting the observed $\xi_{\rm X}$ versus the expected $\langle\zeta(L_{\rm X}, z)\rangle$, estimated using Equation (3.13). Here we use the best fit scaling relation from the SPT-NPS (black points only). Note that the typical bias correction on the mass is about 10 percent at the high mass end.

We explore the likelihood as a function of $A_{\rm SZ}$ and $B_{\rm SZ}$ and show the parameter constraints for the three samples in Table 3.2, and we show the likelihood distribution of the SPT-NPS sample in Figure 3.5. We also show marginalised single parameter probability distributions, which we use to calculate the 68 per cent confidence region for each parameter. This confidence

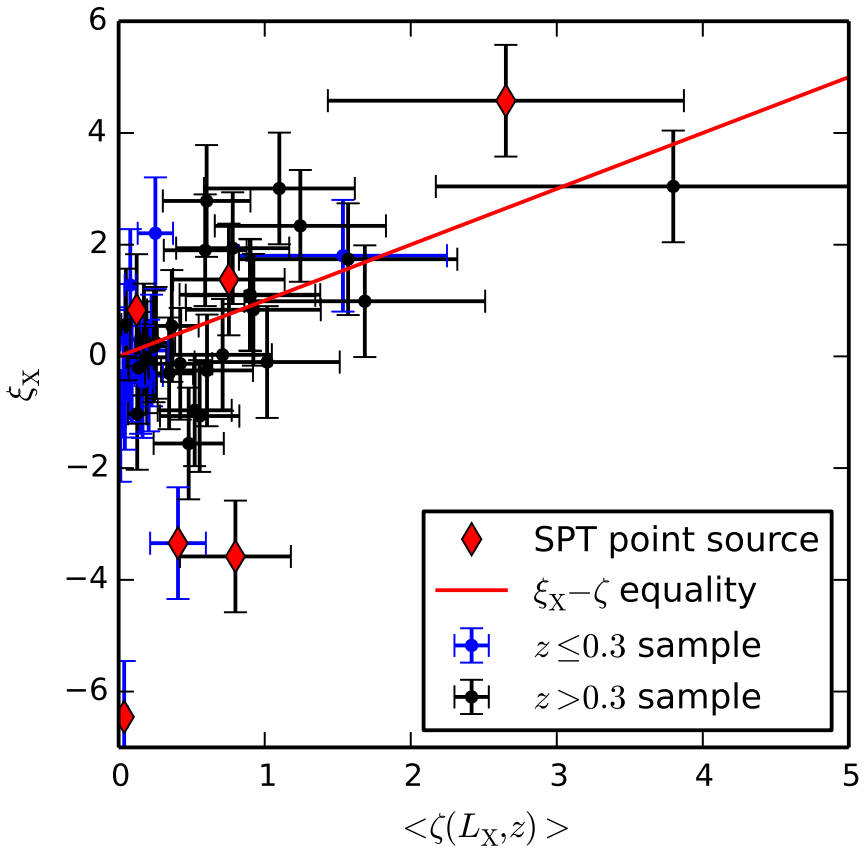

Figure 3.4: The measured significance ξ_X versus the expected SPT-SZ $\langle\zeta(L_X, z)\rangle$, where the best-fitting relation from the SPT-NPS sample and sampling bias corrections are applied. Overplotted is the line of equality. Clusters close to SPT point sources are marked with red diamonds.

region along with the modal value is reported in Table 3.2. For comparison, the constraints from the B13 analysis are shown in red.

All three low mass subsamples show similar normalisation to the extrapolated high mass SPT-SZ sample, but there is a preference for larger slopes. The SPT-NPS sample is the best for comparison to the SPT-SZ high mass sample used in B13; this is because the SPT point sources have been removed to mimic the SPT cluster catalog selection and because there is no measurable difference between the SPT-NPS samples with or without the redshift cut.

The fact that we find consistent results with or without a low-redshift cut may at first be surprising, given that analyses of the high-mass SPT-SZ cut all clusters below z=0.3. In the SPT-SZ high mass sample, the low redshift clusters are cut because the angular scales of these clusters begin to overlap the scales where there is significant CMB primary anisotropy, making extraction with the matched filter approach using two frequencies difficult. However the XMM-BCS clusters are low mass systems with corresponding R_c less than 1 arcmin even at low redshift. So we are able to recover the same scaling relation with or without the low

Table 3.2: Constraints on the SZE ζ-mass relation parameters.

	$A_{\rm SZ}$	$B_{\rm SZ}$
SPT High Mass (B13)	1.50 ± 0.34	1.40 ± 0.16
Prior	$[0.1 - 5]$	$[0.1 - 6]$
Full sample	$1.38^{+0.46}_{-0.36}$	$2.80^{+0.66}_{-0.63}$
SPT-NPS	$1.37^{+0.48}_{-0.38}$	$2.14^{+0.86}_{-0.66}$
SPT-NPS ($z > 0.3$)	$1.37^{+0.60}_{-0.46}$	$2.31^{+1.31}_{-0.86}$
SPT-No-SUMSS	$1.42^{+0.58}_{-0.43}$	$2.14^{+0.91}_{-0.71}$

redshift clusters.

The fully marginalised posterior probability distributions for $B_{\rm SZ}$ can be used to quantify consistency between the two datasets. We do this for any pair of the distributions $P_i\,(\theta)$ by first calculating the probability density distribution of the difference $\Delta\theta$:

$$P(\Delta\theta) = \int {\rm d}\theta P_1(\theta) P_2(\theta - \Delta\theta). \tag{3.18}$$

We then calculate the likelihood p that the origin ($\Delta\theta = 0$) lies within this distribution as

$$p = \int_S {\rm d}\Delta\theta \; P(\Delta\theta) \tag{3.19}$$

where S is the space where $P(\Delta\theta) < P(\Delta\theta = 0)$. We then convert this p value to an equivalent N-σ significance within a normal distribution.

Overall, there is no strong statistical evidence that the low mass clusters behave differently than expected by simply extrapolating the high mass scaling relation to low mass; the slope parameter $B_{\rm SZ}$ of the SPT-SZ high mass and SPT-NPS samples differs by only $1.4\,\sigma$ (Table 3.2). The full sample has a $2.6\,\sigma$ higher $B_{\rm SZ}$ than the SPT-SZ high mass sample (Benson et al., 2013). This steeper slope is presumably due to the contaminating effects of the SPT point sources. We find three outliers below the $L_{\rm X}$-$\xi_{\rm X}$ distribution (Figure 3.4) that are all contaminated by SPT point sources. We list the separation between the cluster centres and the nearest SPT point source in Table 3.4.

It is clear from Figure 3.4 and from the results for the full sample that including X-ray-selected clusters that are associated with point sources strong enough to be detected in SPT-SZ data can bias the derived SZE-mass relation. This is not an issue for SPT and surveys of similar or higher angular resolution, in which the strong point sources can be easily detected and avoided. Point sources below the detection threshold of the SZE survey data do remain a potential issue – we discuss this and the effect of point sources on our results more generally in § 3.5.5.

In addition to the X-ray bolometric luminosities, we test the luminosities based on two other bands (0.5–2.0 keV and 0.1–2.4 keV) as predictors of the cluster mass. After applying the appropriate $L_{\rm X}$-mass relations listed in Table 3.1 we find that the changes to the parameter estimates are small. The largest change is on the slope of the SPT-SZ ζ-mass relation, but the difference is less than $0.2\,\sigma$. Thus, the choice of X-ray luminosity band is not important to our analysis.

Our results show some dependence on the assumed $L_{\rm X}$-mass scaling relation. Adopting the Vikhlinin et al. (2009a) scaling relation has no significant impact on our results. However,

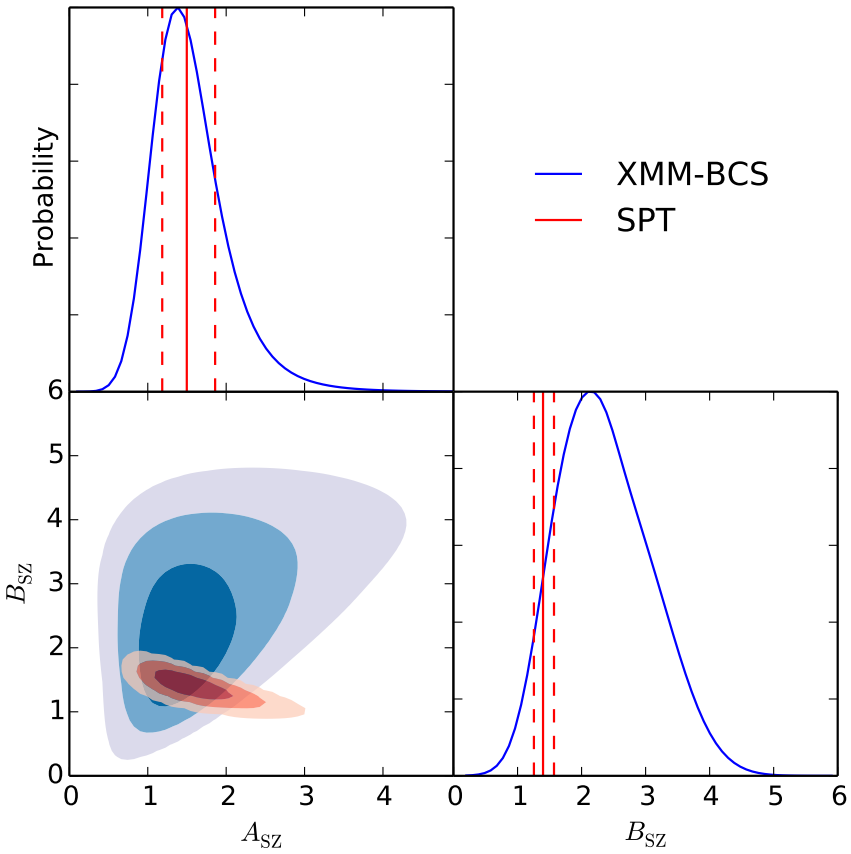

Figure 3.5: Constraints on the SPT-SZ ζ-mass relation parameters A_{SZ} and B_{SZ} for the non-point source sample (SPT-NPS). The different shading indicates 1, 2, and 3σ confidence regions. The constraints from the SPT-SZ high mass clusters (B13) are shown in red with 68 per cent confidence regions marked with dashed lines. The amplitudes for low and high mass clusters are compatible, but the slope is higher for low mass systems by about $1.4\,\sigma$.

with the Mantz et al. (2010a) L_X-mass relation, the slope decreases to $B_{SZ} \sim 1.57$ from 2.14, which makes the SPT-NPS sample almost a perfect match to the high mass SPT-SZ scaling relation. This shift is not surprising, because the Mantz et al. (2010a) L_X-mass relation has a very different slope from Pratt et al. (2009) (1.63 vs. 2.08, respectively). This causes clusters with a $L_X < 1 \times 10^{44}$ erg s^{-1}to have significantly lower estimated masses when assuming the Mantz et al. (2010a) relation (20 per cent on average and ~ 40 per cent at the low mass end). We expect the Pratt et al. (2009) relation to be more appropriate for our analysis, because the Mantz et al. (2010a) relation was calibrated from higher mass clusters, using only clusters with $L_X > 2.5 \times 10^{44}$ erg s^{-1}, above the majority of XMM-BCS clusters. Also we note the change of ξ_X caused by the updated $\theta_{500}(L_X)$ is negligible, which has been shown also in Saliwanchik et al. (2013).

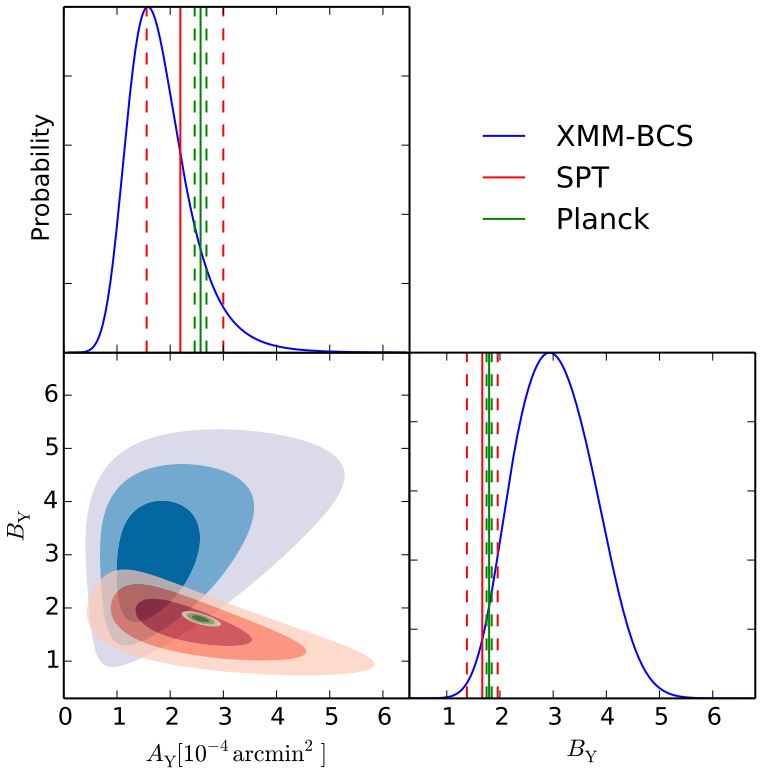

Figure 3.6: Constraints on the Y_{500}-mass relation parameters A_Y and B_Y for the non-point source sample (SPT-NPS). The SPT-NPS constraints are shown in blue and different shades show the 1, 2, and 3 σ levels. The red is for the SPT-SZ result (Andersson et al., 2011), and the green is the best fit from the *Planck* analysis (P11). Marginalised constraints for each parameter are shown in blue with best fit and 1 σ confidence regions marked by solid and dashed lines, respectively.

3.5.4 SZE Y_{500}-mass Relation

We measure the Y_{500}-mass relation, using the SPT-NPS sample. A similar fitting approach is used to account for the selection bias and with the same shifted pivot mass in Equation (3.12) of $1.5 \times 10^{14}\ M_\odot$. The best fit parameters and uncertainties are presented in Table 3.3 along with the results from Andersson et al. (2011) and P11, which are adjusted to use our lower pivot mass. The Y_{500} is based on the Arnaud profile and the L_X is based on the X-ray luminosity measured within the 0.1–2.4 keV band, which facilitates the comparison with the P11 result. The impact from different profiles is discussed later in this section.

Figure 3.6 shows the joint parameter and fully marginalised constraints for A_Y and B_Y. The shaded regions denote the 1, 2, and 3 σ confidence regions as in Figure 3.5 with blue for the SPT-NPS, red for the SPT-SZ sample (Andersson et al., 2011), and green for the *Planck* sample (P11). This figure shows that the low mass SPT-NPS sample has rather weak constraints that are shifted with respect to the high mass SPT-SZ sample and the *Planck* sample.

Table 3.3: Constraints on the Y_{500}-mass relation.

Parameter	$A_{\rm Y}[10^{-4}{\rm arcmin}^2]$	$B_{\rm Y}$
SPT-NPS	$1.59^{+0.63}_{-0.48}$	$2.94^{+0.77}_{-0.74}$
SPT-No-SUMSS	$1.72^{+1.01}_{-0.66}$	$3.29^{+0.84}_{-0.96}$
SPT	2.19 ± 0.63	1.67 ± 0.29
Planck	2.57 ± 0.11	1.78 ± 0.05

We quantify the consistency between any pair of the two-parameter distributions $P_i\,(\boldsymbol{\theta})$ by calculating a p value in a manner similar to that in Equation (3.18) with the null hypothesis $\boldsymbol{\Delta\theta} = 0$. Using this approach, we calculate that the SPT-NPS sample is roughly consistent with the high mass SPT-SZ sample (a $1.4\,\sigma$ difference) but is in tension with the *Planck* result (a $2.8\,\sigma$ difference).

Also shown in Figure 3.6 are the fully marginalised single parameter constraints. These distributions indicate that the normalisation differs by 0.8σ ($1.6\,\sigma$), and the slope parameter differs by $1.7\,\sigma$ ($1.7\,\sigma$) for the SPT-SZ (*Planck*) sample. Alternatively, we fix $B_{\rm Y} = 1.67$ (1.78) to limit the impact of the large uncertainty on the slope on the constraint of the normalisation. In this case, we find $A_{\rm Y} = 1.33^{+0.34}_{-0.31}$ ($1.37^{+0.36}_{-0.32}$) and the discrepancy on $A_{\rm Y}$ is $1.5\,\sigma$ ($3.1\,\sigma$) for the SPT-SZ (*Planck*) sample. As in the ζ-mass relation, there is no strong statistical evidence that the SPT-SZ clusters at low mass behave differently than those at high mass. Tighter constraints on the high mass SPT-SZ scaling relation will be helpful to understand the tension.

The tension with the *Planck* sample is intriguing; here we discuss several possible issues that could contribute. One difference is in the mass ranges probed in the two studies. In P11, the *Planck* team studies the relation between X-ray and SZE properties of 1600 clusters from the Meta-Catalogue of X-ray detected Clusters of galaxies (MCXC, Piffaretti et al., 2011) that span two decades in luminosity (10^{43} erg s$^{-1} \lesssim L_{500,[0.1\,-\,2.4\ {\rm keV}]}E(z)^{-7/3} \lesssim 2\times10^{45}$ erg s^{-1}). In contrast, our sample spans the range 10^{42}erg s$^{-1} \lesssim L_{500,[0.1\,-\,2.4\ {\rm keV}]}E(z)^{-7/3} \lesssim 10^{44}$ erg s^{-1} extending into the galaxy group regime. Thus, it is interesting to probe for any mass trends in the discrepancy. In Figure 3.7, we show our measurements along with the *Planck* relation with fixed slope and redshift evolution as listed in Table 4 in P11 (solid black line). At the luminous (massive) end, our sample matches well with the *Planck* result (cyan points are taken from Figure 4 in P11). Beyond the *Planck* sample at the faint end, we find the preference for lower Y_{500} relative to the *Planck* relation.

In the *Planck* analysis, an $L_{\rm X}$-mass relation without Malmquist bias correction is used (Pratt et al., 2009). They argue that based on the similarity between the REXCESS and MCXC samples, there is no bias correction needed. In our analysis, we use the Malmquist bias-corrected relation and our likelihood corrects for selection bias. Using the non-corrected relation (Pratt et al., 2009) has very little impact. Interestingly, if we adopt the Mantz et al. (2010a) relation, the tension between our result and the *Planck* result disappears mainly due to the lower masses predicted by the relation as discussed in § 3.5.3.

However, given that the *Planck* analysis adopted the Pratt et al. (2009) relation, it is with this same relation that the most meaningful comparisons can be made.

Second, the *Planck* relation is dominated by the high mass clusters, and their measurements at the low luminosity end (marked by cyan points in Figure 3.7) also tend to fall below their best fit relation. The lowest luminosity *Planck* point has a Y_{500} that is 68 per cent ($2\,\sigma$

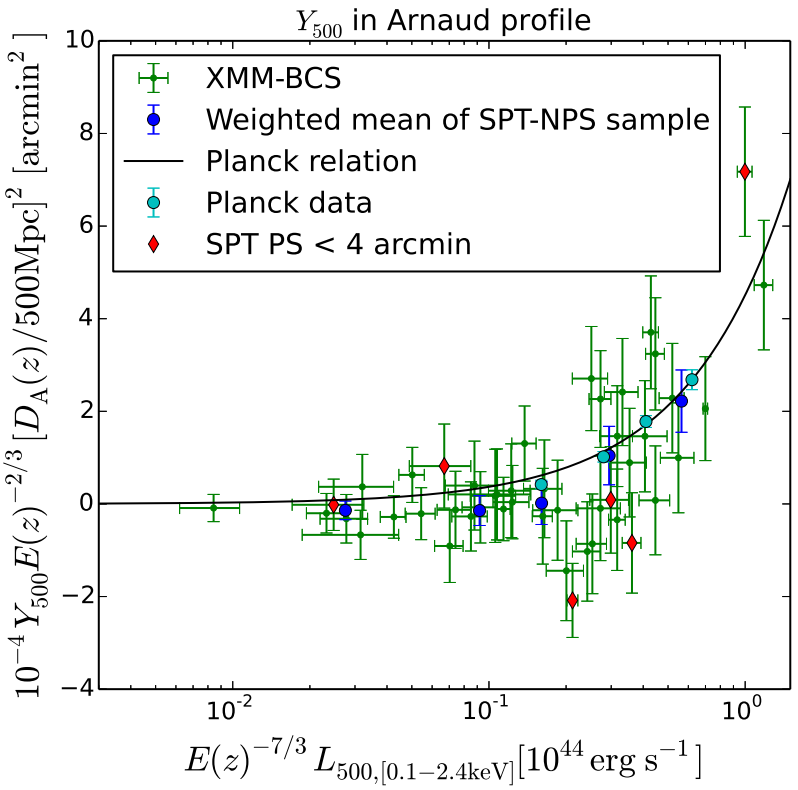

Figure 3.7: Comparison with the *Planck* $Y_{500} - L_{\rm X}$ relation. The green dots are XMM-BCS clusters with $1\,\sigma$ uncertainty on $\xi_{\rm X}$ and measured uncertainties on $L_{\rm X}$ converted from the 0.5–2 keV band. Blue points are inverse variance weighted means of ensembles of the XMM-BCS sample. The black line is the *Planck* SZE relation from table 4 in P11 with the last four binned data points from figure 4 (P11) in cyan. Consistent with our parameter constraints in Figure 3.6, our measurements prefer a lower value than the *Planck* relation. Clusters close to SPT point sources are marked with red diamonds.

offset) of the value of the best fit model at the same X-ray luminosity. Interestingly, the best fit normalisation of the SPT-NPS sample is 53 per cent of the *Planck* model normalisation. In this sense, the tension between the two low mass samples is less than the tension between our sample and the best-fitting *Planck* relation.

Third, we note the redshift dependence of Y_{500}-mass relation could lead to a different normalisation because the SPT-XBCS sample is on average at higher redshift than the *Planck* sample. In P11, they show a weak redshift evolution of Y_{500}, where the index of $E(z)$ term is -0.007 ± 0.518. When they fit with the redshift evolution fixed to the self-similar expectation (2/3), it changes the Y_{500} normalisation by -5 per cent (0.451/0.476), because $E(z)$ is larger than 1 for $z > 0$. In comparison, if we assume an index of 0 for $E(z)$ it will increase our Y_{500} normalisation by 19 per cent compared to the $E(z)^{2/3}$ case (XMM-BCS sample has a mean redshift of 0.48). In this sense, there is some systematic uncertainty in the tension between the two samples that depends on the true redshift evolution of the Y_{500}-mass relation. If the

samples evolve self-similarly, then the *Planck* normalisation should be reduced by 5 per cent.

Finally, the comparison to *Planck* is complicated because of differences between the SPT and *Planck* instruments and datasets and also differences between the analyses. Our analysis of SPT-SZ data calculates the SZE signal exclusively at frequencies below the SZE null (95 GHz and 150 GHz), where the SZE signal is negative, while *Planck* also includes information from frequencies above the 220 GHz SZE null, where the signal is positive. Thus, contamination from sources like radio galaxies with steeply falling spectra, which primarily affect the lowest-frequency bands in both instruments, would tend to bias both the *Planck* and SPT-SZ relations in the same way. But there are other possible sources of contamination such as dusty star-forming galaxies that are much brighter at higher frequencies. A population of star-forming galaxies associated with clusters could artificially increase the *Planck* measured Y_{500}, but could only negatively bias the SPT-SZ measurements. Indeed, we present $2.8\,\sigma$ significant evidence for dusty galaxy flux in our cluster ensemble in § 3.5.6 below.

In summary, there are several potential contributing factors to the 2.8σ tension between the two results. None of them provide a convincing explanation for the offset, suggesting that it may well be a statistical fluctuation. What is needed next is a larger sample with higher quality data to probe this tension and – if the tension persists – to provide insights into the underlying causes of the discrepancy.

3.5.5 Potential Systematics

In the likelihood approach, we fix the cosmological parameters and assume no redshift uncertainty to improve the efficiency of the calculation. We test both of these assumptions and find that neither significantly impacts the analysis. Specifically, the mass function used for correcting the sampling bias is adopted from a fixed cosmology $(\Omega_{\rm M}, \Omega_\Lambda, H_0) = (0.3, 0.7, 70\ \text{km s}^{-1}\text{Mpc}^{-1})$. When we alter these to the recent WMAP results for ΛCDM (Komatsu et al., 2011), we find a negligible impact.

We test the importance of possible photometric redshift biases by shifting the redshifts of all clusters up (or down) by $1\,\sigma$. We update $L_{\rm X}$ appropriately for the new redshifts, and we find a small ($0.5\,\sigma$) shift in the normalisation and no change to the slope. Therefore, redshift biases at this level would not significantly bias the analysis.

3.5.6 Point Source Population

As already noted (see Section 3.5.3), there is a tendency for the systems with the most negative $\xi_{\rm X}$ to be those with nearby SPT point sources (see Figure 3.4). In this section, we explore this association in more detail, testing whether it is biasing our constraints on the SZE mass–observable relations. For the purposes of our analysis, an object is identified as an SPT point source if it appears as a $4\,\sigma$ detection in a single frequency point-source filtered SPT-SZ map in any of the three bands (95, 150, or 220 GHz). An area within a 4 arcmin radius around each point source is defined, and all X-ray selected clusters within that region are flagged. There are six clusters flagged in our sample, and these are denoted with red diamonds in the figures presented above. Given the number densities of the SPT point sources (6 deg^{-2} in this field) and the X-ray selected clusters together with the association radius, we estimate a 36 per cent chance that these point sources are random associations with the clusters.

If we consider a smaller 2 arcmin association radius between the X-ray centre and the SPT point source location, we still find four associations: three of which correspond to the

most negative ξ_X in Figure 3.4, and the fourth is detected only at 220 GHz by SPT (and therefore is likely a dusty galaxy). With the smaller association radius the probability of a random association drops to 7 per cent, providing $\sim 2\,\sigma$ evidence that these point sources are physically associated with the X-ray selected groups.

To further study the point source issue, we cross-match our cluster sample with radio sources detected at 843 MHz by the SUMSS. The survey covers the whole sky at $\delta \leq -30^\circ$ with $|b| > 10^\circ$ down to limiting source brightness of 6 mJy beam^{-1}. For the cross-matching, we utilise the latest version 2.1 of the catalog[1] and a similar matching radius of 2 arcmin. This threshold is much larger than the SUMSS positional uncertainty, which has a median value of ~ 2.3 arcsec.

Within 2 arcmin of the X-ray centres, we find a total of 19 SUMSS point sources matching 18 clusters from our sample. In comparison, given the number density of SUMSS sources (31.6 deg^{-2}, Mauch et al., 2003), the number density of our clusters, and our association radius, we would expect to find ~ 5 clusters randomly overlapping with point sources in the 6 deg^2 survey; there is a 3×10^{-4} per cent chance of explaining the associations as random superpositions. Thus, our small sample provides clear evidence of physical associations between low frequency radio point sources and X-ray selected groups and clusters; this is consistent with previous findings (Best et al., 2005; Lin & Mohr, 2007) that low frequency radio sources are associated with cluster galaxies in both optically and X-ray selected cluster samples. As expected, given the tendency for radio galaxies to have steeply falling spectra as a function of frequency, only a small fraction (3 out of 19) of these low frequency radio galaxies are detectable at SPT frequencies.

We use the BCS data (Desai et al., 2012) to examine the optical counterparts of the six SPT point sources that lie within 4 arcmin of our X-ray selected group and cluster sample. We do this by first associating the SPT point sources with a SUMSS source, which in general is only possible for the radio galaxies and not the dusty galaxies (Vieira et al., 2010). For our sample, three of the SPT point sources within 4 arcmin of the X-ray selected groups and clusters have SUMSS counterparts. All three of these have strongly negative ξ_X (see Figure 3.4). For two of the three point sources, the optical counterpart is the group BCG. In the third case the SPT point source corresponds to a quasar candidate (MRC 2319-550; Wright & Otrupcek, 1990) and does not appear to be a cluster member. The three remaining SPT point sources do not have SUMSS counterparts and are likely dusty galaxies; the SZE signatures ξ_X of those systems are not obviously impacted. Thus we confirm that in two of our 46 low mass systems there are associated radio galaxies bright enough to be detected at SPT frequencies.

Based on the prediction from Lin et al. (2009), we would have expected that radio sources completely fill in the Y_{SZ} signal (100 per cent contamination) at a redshift of 0.1 (or a redshift of 0.6) in approximately 2.5 (or 0.5) percent of clusters with similar mass ($M_{200} = 10^{14} M_\odot$). For our 46 cluster sample, we would have expected this to happen for 1.15 (or 0.23) clusters, consistent with the two clusters we find associated with radio galaxies detected as point sources by SPT-SZ. We also expect a 20 per cent level Y_{SZ} contamination on 9 (2) per cent of the sample. This predicted contamination is significantly smaller than our current uncertainties on the Y_{SZ} normalisation, and therefore cannot be tested in this analysis.

We repeat the SZE-mass relation analysis while excluding the half of the clusters with SUMSS point source associations. We find that the results are qualitatively similar using

[1] `http://www.physics.usyd.edu.au/sifa/Main/SUMSS`

either the SPT-NPS or SPT-No-SUMSS sample (see Tables 3.2 and 3.3), although the uncertainties increase; this is consistent with the expectation that the level of the effect is too small to be measured with our sample. As already shown in Tables 3.2 and 3.3, our analysis shows no statistically significant difference in the SZE-mass relations when excluding or including the systems with nearby SPT point sources.

As pointed out in § 3.5.4, the dusty star-forming galaxies would have a net negative biasing impact on the SPT-SZ measurement. We examine the contamination from the dusty galaxies, which are not bright enough to be directly detectable in the 150 GHz and 95 GHz bands. To do this we measure the specific intensities at 220 GHz in a single frequency adaptive filter that uses cluster profiles at the locations of our X-ray selected cluster sample. In the SPT-NPS sample, the evidence for dusty galaxies is significant at the $2.8\,\sigma$ level. We then convert the 220 GHz intensities to temperature fluctuations at 150 GHz and 95 GHz by assuming the intensity follows $I \propto \nu^{3.6}$ for dusty sources (Shirokoff et al., 2011). These are then converted to the corresponding values of Y_{500}. Dividing then by the expected Y_{500} for a cluster of this redshift and X-ray luminosity, we then estimate the inverse variance weighted mean contamination to be 32 ± 18 per cent and 7 ± 4 per cent at 150 GHz and 95 GHz, respectively. Together, this contamination would lead the SPT-SZ observed Y_{500} signature to be biased low by $\sim (17 \pm 9)$ per cent. This fractional contamination depends on the mass and redshift of the cluster together with the typical star formation activity.

This level of contamination is consistent with a recent study of $\sim$ 550 galaxy clusters selected via optical red-sequence techniques. Using *Herschel* and SPT mm-wave data to jointly fit an SZE+dust spectral model, Bleem (2013) finds the contamination at 150 GHz to be 40 ± 30 per cent for low-richness optical groups ($M_{200} \sim 1 \times 10^{14} M_{\odot}$). The fractional contamination declines as a function of optical richness and is measured to be 5 ± 5 per cent for the richest 3 per cent of clusters in the sample sample ($M_{200} \sim 3$–$6 \times 10^{14} M_{\odot}$). A larger sample size combined with deeper mm-wave data will improve our ability to estimate the contamination from dusty galaxies in clusters and groups.

In summary, this small sample of 46 X-ray selected groups and low mass clusters provides high significance evidence of having physically associated low frequency SUMSS radio galaxies. For the SPT point source sample within 2 arcmin, there is less than $2\,\sigma$ statistical evidence of physical association, but two of the sources have optical counterparts that are in the groups. Although we would expect physically associated high frequency radio galaxies to bias the SZE mass-observable relation, our analysis provides no evidence of this impact. We use the 220 GHz SPT-SZ data in this sample to estimate that the Y_{500} measured by the SPT is biased $\sim 17 \pm 9$ per cent low. A larger sample from a broader survey (through XMM-XXL or eROSITA, for example) or a deeper SZE survey would both help to improve our understanding of the impact of point sources.

3.6 Conclusions

Using data from the SPT-SZ survey, we have explored the SZE signatures of low mass clusters and groups selected from a uniform *XMM-Newton* X-ray survey. The cluster and group sample from the XMM-BCS has a well understood selection, and previously published calibrations of the $L_{\rm X}$-mass relation allow us to estimate the masses of each of these systems. Although these systems have masses that are too low for them to have been individually detected within the SPT-SZ survey, we are able to use the ensemble to constrain the underlying relationship

between the halo mass and the SZE signature for low mass systems.

Our method corrects for the Eddington bias and shows that there is no Malmquist like bias effect on the SZE mass-observable relation within this X-ray selected sample. We test our likelihood using a large mock sample, and we show with the current sample size we can at most extract constraints from two scaling relation parameters: the power law amplitude $A_{\rm SZ}$ and slope $B_{\rm SZ}$ (see Equations 3.5 and 3.12).

We separate the sample of 46 groups and clusters into three subsamples: (1) the full sample, (2) the point source-free sample, for which we exclude systems with point sources detected at significance >4 at either 95, 150, or 220 GHz in the SPT-SZ data within 4 arcmin radius of the X-ray centre, and (3) the point source-free sample, with clusters at $z < 0.3$ excluded. We find that, due to the point source contamination in three of the lowest $\xi_{\rm X}$ groups, the full sample exhibits a steep slope ($B_{\rm SZ} = 2.80^{+0.66}_{-0.63}$) that is in tension at $2.6\,\sigma$ with the high mass SPT sample ($B_{\rm SZ} = 1.40 \pm 0.16$). The point source free subsample has a slope ($B_{\rm SZ} = 2.14^{+0.86}_{-0.66}$) that is in rough agreement with the slope of the high mass SPT sample (1.4σ difference). We find no evidence that the low redshift clusters deviate from the scaling relation of the point source free sample.

We also measure the Y_{500}-mass relation for our sample and compare it to the results from the SPT-SZ high mass clusters and the *Planck* sample. Our low mass sample exhibits a preference for lower normalisation and steeper slope than the other two samples, but the uncertainties are large (see Figure 3.6 and Table 3.3). Within the SPT samples, there is no statistically significant evidence for differences in the scaling relation as one moves from high to low masses. On the other hand, the *Planck* sample exhibits a $2.8\,\sigma$ significant tension with our sample. As shown in Figure 3.7, the lowest X-ray luminosity portion of our sample has lower Y_{500} than expected from the *Planck* relation. We discuss a range of possible explanations for this tension (Section 3.5.4), in particular contamination from dusty sources. Given the significance level of the tension the appropriate next step is to enlarge the sample to better quantify the differences in the SZE signatures of low and high mass clusters and the possible differences between *Planck* and SPT.

We examine radio point source contamination. Cross-matching our X-ray selected groups and clusters with the SUMSS catalog, we find that 18 of 46 members have associated 843 MHz SUMSS point sources within 2 arcmin. This represents highly significant evidence of physical association between our sample and low frequency point sources. At higher frequencies, we find four systems with associated SPT detected point sources; three of these also have SUMSS counterparts. Two of these three point sources have optical counterparts that lie within the X-ray group, and the third is a quasar candidate that is likely unassociated with the group. Having two out of 46 groups or clusters with physically associated bright, high frequency point sources is consistent with the expectations from Lin et al. (2009). The predicted contamination from undetected radio point sources (Lin & Mohr, 2007; Lin et al., 2009) in the remainder of the sample is significantly smaller than our measurement uncertainty on the Y_{500} normalisation, and so we cannot test these predictions here.

We also examine the impact of undetected dusty galaxies. Using the SPT-SZ 220 GHz band, we find $2.8\,\sigma$ significant evidence of a flux excess due to dusty galaxies. Extrapolating to lower frequencies, we estimate that the measured Y_{500} signature is biased low by $\sim (17 \pm 9)$ per cent in this ensemble of low mass clusters and groups. Given the different frequency coverage of *Planck* and SPT, it is not clear that the *Planck* bias due to dusty galaxy flux would be the same. If flux from dusty galaxies would induce a smaller negative bias or even a positive bias in *Planck* Y_{500} measurements, then that would reduce the tension between the *Planck*

Y_{500}–mass relation and ours.

Finally, the receiver on the SPT was upgraded in 2012. The SPTpol camera provides sensitivity to CMB polarization and, more importantly for SZE work, increased sensitivity to CMB temperature fluctuations. The final SPTpol maps are expected to cover 500 square degrees of sky to noise levels of ~ 5 and $\sim 9\mu$K – arcmin at 150 and 95 GHz (Austermann et al., 2012). Meanwhile, the XXL survey (Pierre et al., 2011) has increased the survey area that has a characteristic 10 ks *XMM-Newton* exposure from 6 deg^2 to 25 deg^2. This should enable an interesting new insight into possible differences in the SZE signatures of low and high mass clusters. We make a forecast with a mock catalog that consists of 144 clusters within redshift range 0.2–1.2 and a bolometric flux limit of 1×10^{-14} erg s^{-1}cm^{-2}. Analysing this sample with the appropriate SPTpol increase in depth indicates that with the future sample we can tighten the fractional error on $A_{\rm SZ}$ to 6 per cent compared to our current result of 30 per cent. On $B_{\rm SZ}$ the uncertainty shrinks from 34 to 8 per cent. These improvements should enable a more revealing comparison of the SZE signatures of low and high mass clusters and perhaps also enable a detailed study of potential contamination of the SZE signal by associated radio or dusty galaxies.

Acknowledgments

We acknowledge the support of the DFG through TR33 "The Dark Universe" and the Cluster of Excellence "Origin and Structure of the Universe". Some calculations have been carried out on the computing facilities of the Computational Center for Particle and Astrophysics (C2PAP). The South Pole Telescope is supported by the National Science Foundation through grant PLR-1248097. Partial support is also provided by the NSF Physics Frontier Center grant PHY-1125897 to the Kavli Institute of Cosmological Physics at the University of Chicago, the Kavli Foundation and the Gordon and Betty Moore Foundation grant GBMF 947. This work is also supported by the U.S. Department of Energy. Galaxy cluster research at Harvard is supported by NSF grants AST-1009012 and DGE-1144152. Galaxy cluster research at SAO is supported in part by NSF grants AST-1009649 and MRI-0723073. The McGill group acknowledges funding from the National Sciences and Engineering Research Council of Canada, Canada Research Chairs program, and the Canadian Institute for Advanced Research.

3.7 Appendix

3.7.1 Likelihood function

We start from the full likelihood function based on B13 to constrain both the cosmological model and the scaling relations as (note that the observables are different from the ones used in B13):

$$\ln\ \mathcal{L}(\boldsymbol{c}, \boldsymbol{r}_{\rm SZ}, \boldsymbol{r}_{\rm X}, \Theta) = \sum_i \ln \frac{{\rm d}N(Y_i, f_i, z_i|\boldsymbol{c}, \boldsymbol{r}_{\rm SZ}, \boldsymbol{r}_{\rm X}, \Theta)}{{\rm d}Y{\rm d}f{\rm d}z} - \iiint \frac{{\rm d}N(Y, f, z|\boldsymbol{c}, \boldsymbol{r}_{\rm SZ}, \boldsymbol{r}_{\rm X}, \Theta)}{{\rm d}Y{\rm d}f{\rm d}z}{\rm d}Y{\rm d}f{\rm d}z, \tag{3.20}$$

where i runs over the cluster sample, Y_i is the SZE signal (i.e. $\xi_{\rm X}$ or Y_{500}), f_i is the X-ray flux, and z_i is the redshift. $\boldsymbol{r}_{\rm SZ}$ represents the SZE scaling relation, $\boldsymbol{r}_{\rm X}$ represents the X-

ray scaling relation, and Θ describes the sample selection. $\mathrm{d}N(Y_i, f_i, z_i|\boldsymbol{c}, \boldsymbol{r}_{\rm SZ}, \boldsymbol{r}_{\rm X}, \Theta)$ is the expected number of clusters within a three-dimensional cell $\mathrm{d}Y\mathrm{d}f\mathrm{d}z$, and the second term is the integral of the differential cluster number density over all Y, f and z.

Given the limited sample size, we focus on the SZE-mass scaling relation, keeping the cosmological $\boldsymbol{c}$ and the X-ray scaling relation $\boldsymbol{r}_{\rm X}$ fixed. In addition, we assume the redshift measurements have insignificant uncertainties. Within this context, the X-ray flux is equivalent to the X-ray luminosity L.

The differential number density of clusters can be expressed as:

$$\begin{aligned}&\frac{\mathrm{d}N(Y, L, z|\boldsymbol{c}, \boldsymbol{r}_{\rm SZ}, \boldsymbol{r}_{\rm X}, \Theta)}{\mathrm{d}Y\mathrm{d}L\mathrm{d}z}\\ &\quad = P(Y|L, z, \boldsymbol{c}, \boldsymbol{r}_{\rm SZ}, \boldsymbol{r}_{\rm X}, \Theta)\,\frac{\mathrm{d}N(L, z|\boldsymbol{c}, \boldsymbol{r}_{\rm SZ}, \boldsymbol{r}_{\rm X}, \Theta)}{\mathrm{d}L\mathrm{d}z},\end{aligned} \tag{3.21}$$

where the first factor is the conditional probability of Y given observables L and z with other model parameters, and we are using the relation $\mathrm{d}N/\mathrm{d}Y = P(Y)N$. The second factor is the differential number density of clusters as a function of L and z.

The full likelihood can be split into three parts:

$$\begin{aligned}\ln\mathcal{L}(\boldsymbol{c}, \boldsymbol{r}_{\rm SZ}, \boldsymbol{r}_{\rm X}, \Theta) = &\sum_i \ln P(Y_i|L_i, z_i, \boldsymbol{c}, \boldsymbol{r}_{\rm SZ}, \boldsymbol{r}_{\rm X}, \Theta)\\ &+\sum_i \ln\frac{\mathrm{d}N(L_i, z_i|\boldsymbol{c}, \boldsymbol{r}_{\rm SZ}, \boldsymbol{r}_{\rm X}, \Theta)}{\mathrm{d}L\mathrm{d}z}\\ &-\iiint\frac{\mathrm{d}N(Y, L, z|\boldsymbol{c}, \boldsymbol{r}_{\rm SZ}, \boldsymbol{r}_{\rm X}, \Theta)}{\mathrm{d}Y\mathrm{d}L\mathrm{d}z}\mathrm{d}Y\mathrm{d}L\mathrm{d}z.\end{aligned} \tag{3.22}$$

If the sample selection is based on the X-ray only, then we have:

$$\mathrm{d}N\left(L_i, z_i|\boldsymbol{c}, \boldsymbol{r}_{\rm SZ}, \boldsymbol{r}_{\rm X}, \Theta_{\rm X}\right) = \Theta_{\rm X}(L_i, z_i)\mathrm{d}N(L_i, z_i|\boldsymbol{c}, \boldsymbol{r}_{\rm X}), \tag{3.23}$$

where $\Theta_{\rm X}$ is simply the probability that a cluster with X-ray luminosity L_i and redshift z_i is observed. In addition,

$$\int P(Y|L, z, \boldsymbol{c}, \boldsymbol{r}_{\rm SZ}, \boldsymbol{r}_{\rm X}, \Theta_{\rm X})\mathrm{d}Y = 1, \tag{3.24}$$

which simply means that, because there is only X-ray selection $\Theta_{\rm X}$, any cluster that makes it into the sample due to its X-ray properties will always have a corresponding value Y. Using this condition together with Equation (3.21) allows us to write the third term in Equation (3.22) as:

$$\begin{aligned}&\iiint\frac{\mathrm{d}N(Y, L, z|\boldsymbol{c}, \boldsymbol{r}_{\rm SZ}, \boldsymbol{r}_{\rm X}, \Theta_{\rm X})}{\mathrm{d}Y\mathrm{d}L\mathrm{d}z}\mathrm{d}Y\mathrm{d}L\mathrm{d}z\\ &= \iint\frac{\mathrm{d}N(L, z|\boldsymbol{c}, \boldsymbol{r}_{\rm X}, \Theta_{\rm X})}{\mathrm{d}L\mathrm{d}z}\mathrm{d}L\mathrm{d}z.\end{aligned} \tag{3.25}$$

Note that by adopting Equations (3.23) and (3.25), the last two terms in Equation (3.22) have no remaining dependence on Y and depend only on cosmology $\boldsymbol{c}$, the X-ray-mass scaling relation $\boldsymbol{r}_{\rm X}$ and the X-ray sensitive selection $\Theta_{\rm X}$. Thus, within the context of a fixed cosmology and X-ray scaling relation these two terms are constant and do not contribute to constraining

the SZE scaling relation $\boldsymbol{r}_{\rm SZ}$. Thus, for the final likelihood that we use in this analysis, we obtain

$$\ln \mathcal{L}(\boldsymbol{r}_{\rm SZ}) = \sum_i \ln P(Y_i|L_i, z_i, \boldsymbol{c}, \boldsymbol{r}_{\rm X}, \boldsymbol{r}_{\rm SZ}, \Theta_{\rm X}). \tag{3.26}$$

The derivation of the likelihood is correct even in the presence of correlated scatter between L and Y.

However if the selection were based on both L and Y, then Equation (3.26) would no longer be equivalent to the full likelihood. For instance Equation (3.23) would need to be extended as:

$$\mathrm{d}N\left(L_i, z_i|\boldsymbol{c}, \boldsymbol{r}_{\rm SZ}, \boldsymbol{r}_{\rm X}, \Theta\right) = \int \mathrm{d}Y \Theta(Y, L_i, z_i) \mathrm{d}N(Y, L_i, z_i|\boldsymbol{c}, \boldsymbol{r}_{\rm X}, \boldsymbol{r}_{\rm SZ}). \tag{3.27}$$

And therefore detailed modelling of the selection would be required to calculate the likelihood and constrain the scaling relation parameters.

3.7.2 XMM-BCS Cluster Sample

Table 3.4: SPT ξ_X of XMM-BCS sample.

ID	$L_{X,500,bol}$ [10^{42} erg/s]	$\Delta L_{X,500,bol}$ [10^{42} erg/s]	Redshift	Redshift uncertainty	R_c [arcmin]	ξ_X	SPT point source separation [arcmin] and SN	SUMSS point source separation [arcmin]
011	345.2	51.6	0.97	0.10	0.185	0.99	-	-
018	66.3	6.5	0.39	0.04	0.239	1.90	-	0.92
032	684.0	56.8	0.83	0.07	0.272	3.04	-	1.70, 2.30, 3.97
033	209.0	17.6	0.79	0.05	0.189	2.34	-	-
034	16.0	2.5	0.28	0.02	0.197	-0.38	-	-
035	91.0	14.3	0.67	0.05	0.164	2.78	-	0.10, 1.56
038	16.3	2.5	0.39	0.05	0.147	-0.20	-	1.85
039	19.4	1.2	0.18	0.04	0.315	-0.34	-	2.91
044	310.5	20.5	0.44	0.02	0.367	4.58	3.87 4.84	0.22
069	124.9	21.5	0.75	0.07	0.165	1.38	3.40 6.34	3.42
070	137.9	2.8	0.152	0.001	0.726	1.80	-	-
081	93.1	15.4	0.85	0.12	0.133	-1.56	-	-
082	53.6	9.2	0.63	0.05	0.144	0.55	-	-
088	122.1	16.7	0.43	0.04	0.271	-0.10	-	2.96
090	25.4	5.8	0.58	0.02	0.120	0.30	-	-
094	26.3	2.9	0.269	0.001	0.243	2.20	-	1.48
109	196.9	28.8	1.02	0.09	0.145	1.09	-	0.19
110	68.8	9.3	0.47	0.06	0.205	-1.07	-	0.10
126	82.0	6.1	0.42	0.02	0.240	0.03	-	1.22
127	8.4	1.0	0.207	0.001	0.207	1.28	-	-
132	319.3	35.7	0.96	0.17	0.182	1.74	-	-
136	86.8	7.3	0.36	0.02	0.282	-3.58	1.11 5.84	1.00
139	8.7	1.2	0.169	0.001	0.252	-0.17	-	0.44
150	37.7	1.8	0.176	0.001	0.403	-3.34	0.13 4.23	0.05, 2.29
152	3.4	0.6	0.139	0.001	0.219	-0.45	-	-
156	166.0	11.7	0.67	0.06	0.202	3.01	-	-

Continued.

ID	$L_{X,500,bol}$ [10^{42} erg/s]	$\Delta L_{X,500,bol}$ [10^{42} erg/s]	Redshift	Redshift uncertainty	R_c [arcmin]	ξ_X	SPT point source separation [arcmin] and SN	SUMSS point source separation [arcmin]
158	104.2	15.6	0.55	0.03	0.205	1.94	-	-
210	45.0	9.0	0.83	0.09	0.105	0.18	-	-
227	14.5	1.8	0.346	0.001	0.157	-1.03	-	0.06
245	38.1	7.1	0.62	0.03	0.130	0.24	-	1.38
275	17.8	2.7	0.29	0.03	0.198	-0.46	-	2.12
287	31.1	11.0	0.57	0.04	0.131	-0.02	-	-
288	89.0	17.4	0.60	0.04	0.180	-0.25	-	0.62
357	66.3	8.3	0.48	0.06	0.198	-0.97	-	-
386	17.7	4.8	0.53	0.05	0.115	0.83	0.417 4.53*	-
430	4.5	0.9	0.206	0.001	0.167	-0.67	-	-
444	69.1	13.8	0.71	0.05	0.141	-0.13	-	-
457	1.1	0.3	0.100	0.001	0.201	-1.24	-	-
476	6.2	0.7	0.101	0.001	0.365	-0.12	-	1.03
502	47.2	4.2	0.55	0.05	0.156	-0.30	-	-
511	23.4	3.7	0.269	0.001	0.233	0.11	-	0.15, 2.37
527	160.8	26.2	0.79	0.06	0.172	0.83	-	3.96
528	6.4	2.1	0.35	0.02	0.117	0.57	-	-
538	5.1	2.1	0.20	0.02	0.179	0.30	-	-
543	134.5	29.6	0.57	0.03	0.217	1.10	-	-
547	4.1	1.3	0.241	0.001	0.140	-6.45	0.20 6.75	0.12, 2.89

*Detected in 220 GHz

Chapter 4

Constraints on the CMB Temperature Evolution using Multi-Band Measurements of the Sunyaev Zel'dovich Effect with the South Pole Telescope

A. Saro[1,2], J. Liu[1,2], J. J. Mohr[1,2,3], K. A. Aird[4], M. L. N. Ashby[5], M. Bayliss[5,6], B. A. Benson[7,8,9], L. E. Bleem[8,10,11], S. Bocquet[1,2], M. Brodwin[12], J. E. Carlstrom[8,9,10,11,13], C. L. Chang[8,9,11], I. Chiu[1,2], H. M. Cho[14], A. Clocchiatti[15], T. M. Crawford[8,13], A. T. Crites[8,13], T. de Haan[16], S. Desai[1,2], J. P. Dietrich[1,2], M. A. Dobbs[16], K. Dolag[1,2], J. P. Dudley[16], R. J. Foley[17,18], D. Gangkofner[1,2], E. M. George[19], M. D. Gladders[8,13], A. H. Gonzalez[20], N. W. Halverson[21], C. Hennig[1,2], J. Hlavacek-Larrondo[22,23], W. L. Holzapfel[19], J. D. Hrubes[4], C. Jones[5], R. Keisler[8,10], A. T. Lee[19,24], E. M. Leitch[8,13], M. Lueker[19,25], D. Luong-Van[4], A. Mantz[8], D. P. Marrone[26], M. McDonald[27], J. J. McMahon[28], J. Mehl[8,13], S. S. Meyer[8,9,10,13], L. Mocanu[8,13], T. E. Montroy[29], S. S. Murray[5], D. Nurgaliev[6], S. Padin[8,13,25], A. Patej[6], C. Pryke[30], C. L. Reichardt[19], A. Rest[31], J. Ruel[6], J. E. Ruhl[29], B. R. Saliwanchik[29], J. T. Sayre[29], K. K. Schaffer[8,9,32], E. Shirokoff[19,25], H. G. Spieler[24], B. Stalder[5], Z. Staniszewski[29], A. A. Stark[5], K. Story[8,10], A. van Engelen[16], K. Vanderlinde[33,34], J. D. Vieira[17,25], A. Vikhlinin[5], R. Williamson[8,13], O. Zahn[19], A. Zenteno[1,2]

[1]Department of Physics, Ludwig-Maximilians-Universität, Scheinerstr. 1, 81679 München, Germany

[2]Excellence Cluster Universe, Boltzmannstr. 2, 85748 Garching, Germany

[3]Max-Planck-Institut für extraterrestrische Physik, Giessenbachstr. 85748 Garching, Germany

[4]University of Chicago, 5640 South Ellis Avenue, Chicago, IL 60637

[5]Harvard-Smithsonian Center for Astrophysics, 60 Garden Street, Cambridge, MA 02138

[6]Department of Physics, Harvard University, 17 Oxford Street, Cambridge, MA 02138

[7]Center for Particle Astrophysics, Fermi National Accelerator Laboratory, Batavia, IL, USA 60510

[8]Kavli Institute for Cosmological Physics, University of Chicago, 5640 South Ellis Avenue, Chicago, IL 60637

[9]Enrico Fermi Institute, University of Chicago, 5640 South Ellis Avenue, Chicago, IL 60637

[10] Department of Physics, University of Chicago, 5640 South Ellis Avenue, Chicago, IL 60637
[11]Argonne National Laboratory, 9700 S. Cass Avenue, Argonne, IL, USA 60439
[12]Department of Physics and Astronomy, University of Missouri, 5110 Rockhill Road, Kansas City, MO 64110
[13]Department of Astronomy and Astrophysics, University of Chicago, 5640 South Ellis Avenue, Chicago, IL 60637
[14]NIST Quantum Devices Group, 325 Broadway Mailcode 817.03, Boulder, CO, USA 80305
[15]Departamento de Astronomia y Astrosifica, Pontificia Universidad Catolica,Chile
[16]Department of Physics,McGill University, 3600 Rue University, Montreal, Quebec H3A 2T8, Canada
[17]Astronomy Department, University of Illinois at Urbana-Champaign,1002 W. Green Street,Urbana, IL 61801 USA
[18]Department of Physics, University of Illinois Urbana-Champaign,1110 W. Green Street,Urbana, IL 61801 USA
[19]Department of Physics, University of California, Berkeley, CA 94720
[20]Department of Astronomy, University of Florida, Gainesville, FL 32611
[21]Department of Astrophysical and Planetary Sciences and Department of Physics, University of Colorado,Boulder, CO 80309
[24]Physics Division, Lawrence Berkeley National Laboratory, Berkeley, CA 94720
[25]California Institute of Technology, 1200 E. California Blvd., Pasadena, CA 91125
[26]Steward Observatory, University of Arizona, 933 North Cherry Avenue, Tucson, AZ 85721
[27]Kavli Institute for Astrophysics and Space Research, Massachusetts Institute of Technology, 77 Massachusetts Avenue,Cambridge, MA 02139
[28]Department of Physics, University of Michigan, 450 Church Street, Ann Arbor, MI, 48109
[29]Physics Department, Center for Education and Research in Cosmology and Astrophysics, Case Western Reserve University, Cleveland, OH 44106
[30]Physics Department, University of Minnesota, 116 Church Street S.E., Minneapolis, MN 55455
[31]Space Telescope Science Institute, 3700 San Martin Dr., Baltimore, MD 21218
[32]Liberal Arts Department, School of the Art Institute of Chicago, 112 S Michigan Ave, Chicago, IL 60603
[33]Dunlap Institute for Astronomy & Astrophysics, University of Toronto, 50 St George St, Toronto, ON, M5S 3H4, Canada
[34]Department of Astronomy & Astrophysics, University of Toronto, 50 St George St, Toronto, ON, M5S 3H4, Canada

This chapter is a reproduction of the publication Saro et al. (2014).

4.1 Abstract

The adiabatic evolution of the temperature of the Cosmic Microwave Background (CMB) is a key prediction of standard cosmology. We study deviations from the expected adiabatic evolution of the CMB temperature of the form $T(z) = T_0(1+z)^{1-\alpha}$ using measurements of the spectrum of the Sunyaev Zel'dovich Effect with the South Pole Telescope (SPT). We present a method for using the ratio of the Sunyaev Zel'dovich signal measured at 95 and 150 GHz in the SPT data to constrain the temperature of the CMB. We demonstrate that

this approach provides unbiased results using mock observations of clusters from a new set of hydrodynamical simulations. We apply this method to a sample of 158 SPT-selected clusters, spanning the redshift range $0.05 < z < 1.35$, and measure $\alpha = 0.017^{+0.030}_{-0.028}$, consistent with the standard model prediction of $\alpha = 0$. In combination with other published results, we find $\alpha = 0.005 \pm 0.012$, an improvement of $\sim 10\%$ over published constraints. This measurement also provides a strong constraint on the effective equation of state in models of decaying dark energy $w_{\rm eff} = -0.994 \pm 0.010$.

4.2 Introduction

The existence of the cosmic microwave background is a fundamental prediction of the Hot Big Bang Theory. The intensity spectrum of the CMB radiation locally has been measured by the COBE FIRAS instrument and found to have a nearly exact blackbody spectrum with a temperature of $T_0 = 2.72548 \pm 0.00057$ K (Fixsen et al. 2009).

A second fundamental prediction of the hot Big Bang theory is that the CMB temperature must evolve over cosmic time. Specifically, it is expected to evolve as $T(z) = T_0(1 + z)$ (Tolman, 1934), under the assumption that the CMB photon fluid reacts adiabatically to the expansion of the Universe as described by general relativity and electromagnetism. Deviations from the adiabatic evolution of $T(z)$ would imply either a violation of the hypothesis of local position invariance, and therefore of the equivalence principle, or that the number of photons is not conserved. In the former case, this could be associated with variations of dimensionless coupling constants like the fine-structure constant (see, e.g., Martins 2002, Murphy et al. 2003, Srianand et al. 2004). The latter case is a consequence of many physical processes predicted by non-standard cosmological models, such as decaying vacuum energy density models, coupling between photons and axion-like particles, and modified gravity scenarios. (e.g., Matyjasek, 1995; Overduin & Cooperstock, 1998; Lima et al., 2000; Puy, 2004; Jaeckel & Ringwald, 2010; Jetzer & Tortora, 2011). In all of these models, energy has to be slowly injected or removed from the CMB without distorting the Planck Spectrum sufficiently to violate constraints from FIRAS (Avgoustidis et al., 2012).

Observational tests of non-standard temperature evolution typically are parametrized by very simple models for the deviation. In particular, we consider here the scaling law proposed by Lima et al. (2000):

$$T(z) = T_0(1 + z)^{1-\alpha}, \tag{4.1}$$

with α being a free constant parameter[1]. This is the phenomenological parametrization that has been most widely studied by previous authors; deviations of α from zero would result as a consequence of one of the scenarios described above, such as the non-conservation of photon number.

To date, two different observables have been used to determine $T(z)$. At intermediate redshifts ($z \lesssim 1.5$), $T(z)$ can be determined from measurements of the spectrum of the Sunyaev-Zel'dovich effect (SZE) (Sunyaev & Zel'dovich 1972), a technique first suggested by Fabbri et al. (1978); Rephaeli (1980). The first attempt to measure $T(z)$ using the spectrum of the SZE was reported in Battistelli et al. (2002) using multi-frequency observations of the clusters A2163 and Coma. Luzzi et al. (2009) reported results from the analysis of a sample

[1]In previous literature this parameter has been referred to with the Greek letter α or β. To avoid confusion with the variable $\beta = v/c$ defined in Equation (4.2), we use α.

of 13 clusters with $0.23 \leq z \leq 0.546$. Adopting a flat prior on $\alpha \in [0, 1]$, they provided constraints $\alpha = 0.024^{+0.068}_{-0.024}$, consistent with standard adiabatic evolution.

At high redshift ($z \gtrsim 1$), the CMB temperature can be determined from quasar absorption line spectra which show atomic or molecular fine structure levels excited by the photo-absorption of the CMB radiation. If the system is in thermal equilibrium with the CMB, then the excitation temperature of the energy states gives the temperature of the black-body radiation (e.g., Srianand et al., 2000; Molaro et al., 2002; Srianand et al., 2008). For example, Noterdaeme et al. (2011) have reported on a sample of five carbon monoxide absorption systems up to $z \sim 3$ where the CMB temperature has been measured. They used their sample, in combination with low redshift SZE measurements to place constraints on the phenomenological parameter $\alpha = -0.007 \pm 0.027$. This also allowed them to put strong constraints on the effective equation of state of decaying dark energy models $w_{\rm eff} = -0.996 \pm 0.025$. Recently, Avgoustidis et al. (2012) extended this analysis by including constraints inferred from differences between the angular diameter and luminosity distances (the so-called distance-duality relation), which is also affected in models in which photons can be created or destroyed. They also showed that by releasing the positive prior assumption on α the same cluster sample studied in Luzzi et al. (2009) constrains $\alpha = 0.065 \pm 0.080$.

More recently, Muller et al. (2013) fit molecular absorption lines towards quasars to measure the CMB temperature with an accuracy of a few percent at $z = 0.89$. Combining their data with the data presented in Noterdaeme et al. (2011) they were able to further constrain $\alpha = 0.009 \pm 0.019$.

Constraints on the CMB redshift evolution can be significantly improved by including measurements of the SZE spectrum from experiments, such as the SPT and Planck, with much larger cluster samples. For instance, de Martino et al. (2012) forecast the constraining power of Planck to measure α. Using only clusters at $z < 0.3$, they predicted that Planck could measure α with an accuracy $\sigma_\alpha = 0.011$. Recently, Hurier et al. (2014) analysed a sample of 1839 galaxy clusters observed with Planck. The cluster sample they adopted also included the SPT sample that we analyse here, although it did not contribute significantly to their main results. They were able to constrain $\alpha = 0.009 \pm 0.017$ by stacking the 813 confirmed SZE detected clusters of the Planck catalog (Planck Collaboration, 2013a) in different redshift bins, with only one cluster in each of their highest redshift bins $z = 0.8$ and $z = 1$. In combination with other available constraints (Luzzi et al., 2009; Noterdaeme et al., 2011; Muller et al., 2013), they limit deviations from adiabatic temperature evolution of the Universe to be $\alpha = 0.006 \pm 0.013$.

In this work, we present constraints on the temperature evolution of the CMB using SZE spectral measurements at the 95 and 150 GHz bands from the South Pole Telescope. The SPT is a 10m millimetre-wave telescope operating at the South Pole (Carlstrom et al., 2011) that has recently completed a 2500 deg^2 multi-frequency survey of the southern extragalactic sky. Here we focus on the SZE selected cluster sample that lies within a 720 deg^2 subregion where optical follow-up and redshift measurements are complete (Song et al., 2012b; Reichardt et al., 2013).

4.3 Method

Inverse Compton scattering of the CMB photons by the hot intracluster medium induces secondary CMB temperature anisotropies in the direction of clusters of galaxies. Neglecting

relativistic corrections, the thermal SZE (tSZE) and kinematic SZE (kSZE) contribution to the temperature anisotropy in the direction $\hat{n}$ of a cluster at a frequency ν can be approximated by (Sunyaev & Zeldovich 1980):

$$\Delta T(\hat{n}, \nu) \simeq T_0(\hat{n})[G(\nu) y_c(\hat{n}) - \tau\beta]. \tag{4.2}$$

Here $T_0(\hat{n})$ is the current CMB temperature at the direction $\hat{n}$, β is the line of sight velocity of the cluster in the CMB frame in units of the speed of light c and τ is the optical depth. The Comptonization parameter y_c is related to the integrated pressure along the line of sight $y_c = (k_B \sigma_T / m_e c^2) \int n_e T_e dl$ (where n_e and T_e are respectively the electron density and temperature). In the non-relativistic regime and for adiabatic expansion, $G(x) = x \coth(x/2) - 4$, where the reduced frequency x is given by $x = h\nu(z)/k_B T(z) = h\nu_0(1+z)/[k_B T_0(1+z)] \equiv x_0$ and is independent of redshift, $\nu(z)$ is the frequency of a CMB photon scattered by the intra-cluster medium and $T(z)$ is the black body temperature of the CMB at the cluster location.

If $T(z) = T_0(1+z)^{1-\alpha}$, then the reduced frequency varies as $x(z, \alpha) = x_0(1+z)^\alpha$ and the spectral frequency dependence of $G(\nu)$, the tSZE, now also depends on α: $G(x) = G(\nu_0, \alpha, z)$. From Equation (4.2), neglecting the kSZE contribution, it follows that measuring the ratio of temperature decrements at two different frequencies ν_1 and ν_2 provides:

$$R(\nu_1, \nu_2, z, \alpha) \equiv \frac{\Delta T(\hat{n}, \nu_1, z)}{\Delta T(\hat{n}, \nu_2, z)} \simeq \frac{G(\nu_1, z, \alpha)}{G(\nu_2, z, \alpha)} \tag{4.3}$$

This ratio is redshift independent for $\alpha = 0$, but not in the case of $\alpha \neq 0$. This method has the advantage that, by taking ratios, the dependence on the Comptonization parameter y_c (and therefore on the cluster properties) is removed and the need to account for model uncertainties on the gas density and temperature profile is avoided (Battistelli et al 2002, Luzzi et al 2009). Note that in this approach the distribution of temperature ratios is, in general, non-Gaussian (Luzzi et al. 2009) and needs to be properly modelled.

One important source of noise in these measurements is the primary anisotropy of the CMB. To precisely measure $\Delta T(\hat{n}, \nu)$ for a single cluster, we would have to remove the primary CMB anisotropies in the direction $\hat{n}$. In principle, this could be done by subtracting the CMB temperature measured near the SZE null frequency, which, in the case of $\alpha = 0$ and non-relativistic ICM, is given by a map obtained at 217 GHz (de Martino et al. 2012). Alternatively, because the primary CMB fluctuations are random, it is possible to reduce this source of noise by averaging over a large sample of clusters (e.g. Hurier et al. 2014).

In Reichardt et al. (2013), the SPT cluster sample was selected using a matched multi-frequency spatial filter (Melin et al., 2006), designed to optimally measure the cluster signal given knowledge of the cluster profile and the noise in the maps. The cluster gas profiles are assumed to be well fit by a spherical β model (Cavaliere & Fusco-Femiano, 1976), with $\beta = 1$ and twelve possible core radii, θ_c, linearly spaced from 0.25 to 3 arcmin. The noise contributions include, astrophysical (e.g., the CMB, point sources) and the instrumental (e.g., atmospheric, detector) contributions. For each cluster, the maximum signal to noise in the spatially filtered maps was denoted as ξ.

In this work, we measure the ratio of the CMB temperature decrements in the SPT data at 95 and 150 GHz (T_{95} and T_{150}). We extract the cluster signal from the single-frequency spatially filtered maps at 95 and 150 GHz, using the SPT position and core radius favored by the multi-frequency analysis in Reichardt et al. (2013). To compare the decrement at each frequency, we need to account for the smaller beam at 150 GHz. We do this by convolving

the 150 GHz data to the same beam size as the 95 GHz noisier data, and then using the 95 GHz filter to extract the signal from the resultant 150 GHz maps. Therefore, we adopt the following Fourier domain spatial filter:

$$\psi(k_x, k_y) = \frac{B_{95}(k_x, k_y) S(|\vec{k}|)}{B_{95}(k_x, k_y)^2 N_{astro}(|\vec{k}|\ ) + N_{95}(k_x, k_y)} \tag{4.4}$$

where ψ is the matched filter, B_{95} is the SPT beam for the 95 GHz band and S is the assumed source template. The noise contributions N_{astro} and N_{95} respectively encapsulate the astrophysical (mainly CMB) and the instrumental noise for the 95 GHz band.

The associated uncertainty ΔT_{95} and ΔT_{150} in the CMB temperature decrement would be equal to the R.M.S. of the single-frequency spatially filtered maps. We note that this method is unbiased with respect to the assumed cluster profile. In fact, as the two bands have been homogenized to the larger 95 GHz beam, different assumptions of source template S would only result in tighter or weaker constraints. We also note that in practice, adopting different cluster profiles as a Gaussian template, Arnaud et al. (2010) or Nagai et al. (2007) pressure profile has a negligible impact on the estimated ξ (Vanderlinde et al. 2010).

Finally, we use the derived values of temperature in the two bands and the associated cluster redshift to constrain α from Equation (4.3) through a maximum likelihood analysis (Luzzi et al. 2009) where the likelihood is defined as :

$$\mathcal{L}(\alpha) \propto \prod_{i=1}^{N_{\rm clus}} \exp\left\{ -\frac{[T_{150}^{(i)} R(z^{(i)}, \alpha) - T_{95}^{(i)}]^2}{2[(\Delta T_{150}^{(i)} R(z^{(i)}, \alpha))^2 + (\Delta T_{95}^{(i)})^2]} \right\}, \tag{4.5}$$

and $R(z, \alpha) \equiv R(95\ \text{GHz}, 150\ \text{GHz}, z, \alpha)$ according to Equation (4.3) is calculated by integrating:

$$R(z, \alpha) = \frac{\int G(\nu, z, \alpha) F_{95}(\nu) d\nu}{\int G(\nu, z, \alpha) F_{150}(\nu) d\nu}, \tag{4.6}$$

where F_{95} and F_{150} are the measured filter response of the SPT 95 and 150 GHz bands, normalized such that the integral over each of the bands is one. We have assumed the non-relatitivistic expression for $G(\nu, z, \alpha)$, however, we find relativistic corrections have a negligible effect on our result. For the range of electron temperatures and optical depths expected in our cluster sample (e.g. Reichardt et al. 2013, Vikhlinin et al. 2009a, Arnaud et al. 2010), including relativistic corrections from Itoh et al. (1998) changes our final constraints on α by less than 1 per cent.

4.4 Verification of Method with Simulations

We test the method described above using simulations. To do so, we make mock SPT observations of clusters that are formed in a large volume, high resolution cosmological hydrodynamical simulation (Dolag et al., in preparation). The simulation has been carried out with P-GADGET3, a modification of P-GADGET-2 (Springel, 2005). The code uses an entropy-conserving formulation of SPH (Springel & Hernquist, 2002) and includes treatment of radiative cooling, heating by a UV background, star formation and feedback processes from supernovae explosions and active galactic nuclei (Springel & Hernquist, 2003; Fabjan et al., 2010). Cosmological parameters are chosen to match WMAP7 (Komatsu et al. 2011). The

simulation box is 1244 Mpc per side and contains 1526^3 dark matter particles and as many gas particles, from which five simulated SZE light-cones, each of size $13^\circ \times 13^\circ$ (i.e., the total solid angle is 845 deg^2) have been extracted up to $z \sim 2$. From each of these simulated SZE maps, we then construct simulated SPT maps at 95 and 150 GHz.

The details of the construction of the simulated SZE light-cones will be presented in a forthcoming paper (Liu et al. 2014, in preparation), we highlight here the basic properties. In these mock observations, we include contributions from: (1) primary CMB anisotropies, (2) convolution with the SPT 150 GHz and 95 GHz beams, (3) instrumental noise consistent with the observed SPT map depths of 18 and 44 μK-arcmin for the 150 GHz and 95 GHz bands, respectively, and (4) associated filter transfer functions for the two simulated bands. Finally, from these mock maps we identify clusters with the same approach adopted for real SPT clusters (e.g., Staniszewski et al., 2009; Reichardt et al., 2013), obtaining a sample of 212 clusters above signal to noise $\xi = 4.5$.

We then measure the ratio of the temperatures in the two bands, using the approach described in Section 2. We first convolve the 150 GHz maps to match the larger beam of the 95 GHz band. We then individually filter the 95 GHz and the 150 GHz maps with the 95 GHz filter and measure the signal at the position and θ_C scale that maximize the signal to noise in the multifrequency analysis. We then maximize the likelihood to determine α (Equation (4.5)). We recover $\alpha = 0.0019 \pm 0.022$, in agreement with the input value of $\alpha = 0$.

4.5 SPT Results

We measure the temperature decrement ratios at the positions of the SPT-selected cluster sample from (Reichardt et al., 2013), which included data from 720 of the 2500 deg^2 SPT-Sunyaev-Zel'dovich (SZ) survey. The SPT-SZ data used here has typical noise levels of 44 μK-arcmin and 18 μK-arcmin in CMB temperature units at 95 GHz and 150 GHz, respectively. The exceptions are the two fields centered at $23^h30^m, -55^d$ and $5^h30^m, -55^d$ from Reichardt et al. (2013), which have a depth of 13 μK-arcmin in the 150 GHz data used in this work. Since the publication of Reichardt et al. (2013), these fields had been re-observed in the SPT-SZ survey, with the new observations providing new 95 GHz measurements and deeper 150 GHz data. The final cluster sample used here consists of 158 clusters with both a $\xi > 4.5$ from Reichardt et al. (2013), and either a spectroscopic or photometric redshift reported in Song et al. (2012b). We refer the reader to Staniszewski et al. (2009), Vanderlinde et al. (2010), Schaffer et al. (2011), Williamson et al. (2011), Reichardt et al. (2013) for a detailed description of the survey strategy and dataset characteristics .

We apply the same technique described in § 4.3 and tested in § 4.4 to measure the evolution of the CMB temperature with SPT clusters.

Using SPT data alone, we constrain the temperature evolution of the CMB to be

$$\alpha = 0.017^{+0.030}_{-0.028}, \tag{4.7}$$

which is consistent with the adiabatic expectation of $\alpha = 0$. We estimate the instrumental uncertainties associated with the beams, calibration, and filter responses, and find them all to have a negligible result on this constraint. Moreover, the statistical uncertainty is $\sim 30\%$ larger than the limit on possible observational biases implied by the results of § 4.4, implying that our analysis method is shown to be unbiased at or below the level of the statistical uncertainty.

We further combine our results with previously published data (Figure 4.1). In particular we include other cluster measurements (Luzzi et al., 2009; Hurier et al., 2014) and fine structure absorption lines (Noterdaeme et al., 2011; Muller et al., 2013). In doing this we exclude from the likelihood calculation (Equation (4.5)) the 16 SPT clusters that were part of the main sample analysed by Hurier et al. (2014). We thus obtain a tighter constraint on the $T(z) = T_0(1+z)^{(1-\alpha)}$ law:

$$\alpha = 0.005 \pm 0.012, \tag{4.8}$$

a $\sim 10\%$ improvement in measurement uncertainty in comparison to the previously reported $\alpha = 0.006 \pm 0.013$ (Hurier et al., 2014). We note that because the SPT data are on average a factor of 3 deeper than Planck, and the SPT beam is ~ 8 times smaller, the SPT dataset provides stronger constraints on a per cluster basis and is particularly well suited for studies of the high redshift tail of the cluster distribution. In fact, only 4% the Planck selected clusters have redshifts larger than the median redshift of the SPT sample.

The measurement presented here is consistent with the adiabatic evolution of the CMB radiation temperature ($\alpha = 0$) expected from the standard hot Big-Bang model. Considering alternative cosmological models, Jetzer et al. (2011) demonstrated that measuring $T(z)$ at different redshifts allows one to constrain the effective equation of state of decaying dark energy ($p = w_{\rm eff}\rho$). Following Noterdaeme et al. (2011), by fitting the combined constraints on $T(z)$ with the temperature-redshift relation (Eq. 22 in Jetzer et al. 2011), taking $\Omega_{\rm m} = 0.255 \pm 0.016$ (Reichardt et al., 2013) and fixing the adiabatic index γ to the canonical value (4/3), we get $w_{\rm eff} = -0.994 \pm 0.010$, which improves upon previous constraints (Noterdaeme et al., 2011; Hurier et al., 2014).

4.5.1 Selection bias

A number of possible selection biases could affect our measurements. In particular, cluster candidates were identified using a multi-band matched-filter approach (Melin et al. 2006) where the temperature evolution of the Universe is assumed to be adiabatic. This could therefore bias our selection towards clusters that best mimic this behavior. To show that this is not the case, we construct SPT mock lightcones similar to the ones presented in § 4.4 but assuming different values of α. We then performed the same analysis described in § 4.4 and show that we are able to recover the input value. Specifically we test simulations with input values of α offset by more than 3σ from the adiabatic value, $\alpha = -0.12$ and $\alpha = 0.12$. We then select clusters with the above described matched-filter multi-frequency cluster finder under the assumption of adiabatic evolution and constrain α. We obtain unbiased measurements for the underlying input value $\alpha = -0.111^{+0.022}_{-0.018}$ and $\alpha = 0.110^{+0.014}_{-0.014}$, thus demonstrating that the selection is not driving our constraints (bottom panel of Figure 4.1).

Another potential source of bias in our measurement of α is the fact that the temperature fluctuations of the CMB at the location of the SPT clusters should not average to zero. In fact, due to the adopted cluster selection, negative temperature fluctuations are more likely than positive ones (Vanderlinde et al., 2010). We estimate this effect to be negligible using the simulations described in § 4.4. We also note that this effect should be less significant at larger SPT signal to noise ξ (Benson et al., 2013). If we restrict our analysis to the clusters with $\xi > 8$, which reduces the cluster sample by a factor of $\sim$6 to the 24 highest signal-to-noise clusters, we constrain $\alpha = 0.023^{+0.044}_{-0.038}$. This is consistent with our main result with only a modest 30% increase in the uncertainty in α. This demonstrates that the constraints depend most significantly on the highest signal to noise clusters, which will be less biased by the

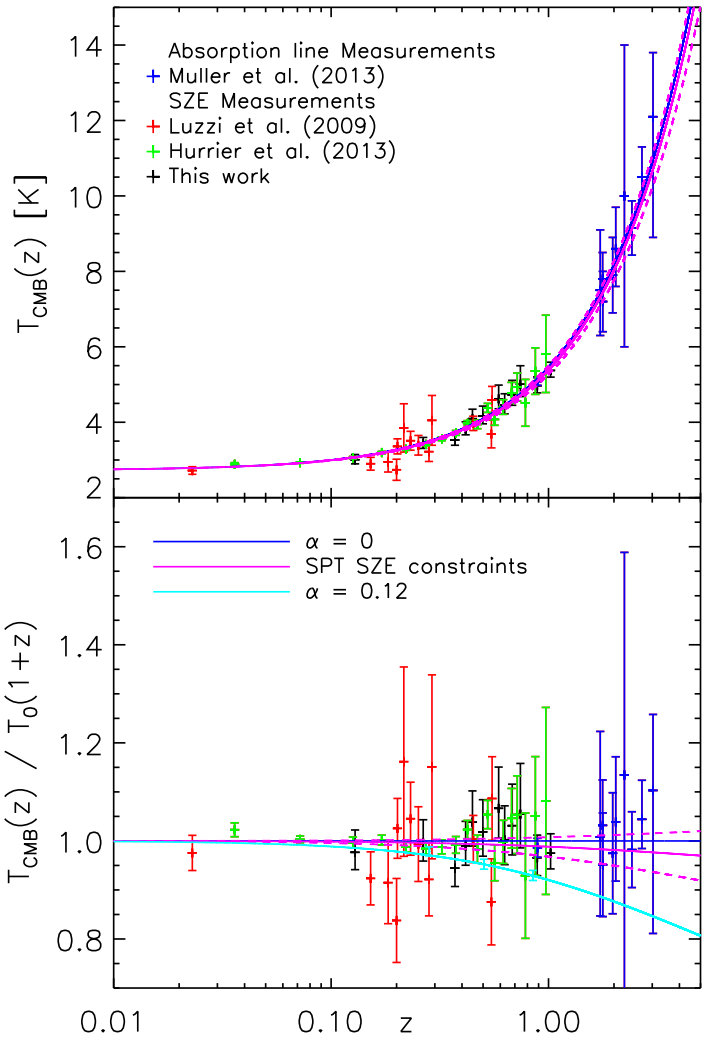

Figure 4.1: *Top panel:* Measurements of the temperature of the CMB as a function of redshift. Blue points are absorption lines studies (see Muller et al 2013 and references therein). SZE measurments toward galaxy clusters are highlighted in red (see Luzzi et al. 2009 and references therein) and green for the stacked Planck SZE selected clusters (Hurier et al. 2013). Black points are the SPT-SZ cluster constraints. For visualisation purposes SPT clusters results have been obtained by reverting Eq. 1 from the measured contraints on α in each of 12 equally populated redshift bins. The blue continuous line corresponds to the relation $T(z) = T_0 \times (1 + z)$ and solid and dashed purple lines are the evolution corresponding to the best fit and $\pm 1\sigma$ models. *Bottom panel:* Deviation of the measured temperature of the CMB as a function of redshift with respect to the adiabatic evolution. Cyan points represent the measured temperature of the CMB in three stacked redshift bins for a simulation with input value $\alpha = 0.12$ (cyan solid line).

CMB from the SPT-selection. Similarly, we estimate the bias associated with lensed dusty sources to be unimportant for our analysis; their primary impact would be introducing some skewness in the scatter of clusters about our best fit model (Hezaveh et al., 2013).

Emission from cluster galaxies can also potentially bias our measurement. We estimate the effect to be negligible by performing the analysis presented here on subsamples of clusters above different ξ thresholds and by excluding clusters in proximity to known SUMSS sources (Mauch et al., 2003). All subsamples examined provide statistically consistent results. For example, using a subsample of 75 clusters with no associated SUMSS sources brighter than 20 mJy within a projected distance of 3 arcmin from the cluster centers, we obtain consistent results of $\alpha = 0.021^{+0.042}_{-0.038}$.

4.6 Conclusions

We have studied deviations from the adiabatic evolution of the mean temperature of the CMB in the form of $T(z) = T_0(1+z)^{(1-\alpha)}$. We present a method based on matched-filtering of clusters at the SPT frequencies and show that we are able to recover unbiased results using simulated clusters. The simulated lightcones we use come from a large cosmological hydrodynamical simulation and include realistic SPT beam effects, CMB anisotropy and SPT noise levels for both the 150 GHz and 95 GHz bands.

We apply this method to a sample of 158 SPT clusters selected from 720 square degrees of the 2500 square degree SPT-SZ survey, which span the redshift range $0.05 < z < 1.35$, and measure $\alpha = 0.017^{+0.030}_{-0.028}$, consistent with the standard model prediction of $\alpha = 0$. Our measurement gives competitive constraints and significantly extends the redshift range with respect to previously published results based on galaxy clusters (e.g., Luzzi et al., 2009; Avgoustidis et al., 2012; de Martino et al., 2012; Muller et al., 2013; Hurier et al., 2014). Combining our measurements with published data we obtain $\alpha = 0.005 \pm 0.012$, improving current published constraints.

Such tight limits on deviations from the adiabatic evolution of the CMB also put interesting constraints on the effective equation of state of decaying dark energy models, $w_{\rm eff}$. Indeed, from SPT clusters alone we are able to measure $w_{\rm eff} = -0.988^{+0.029}_{-0.033}$, in good agreement with previous constraints based on quasar absorption lines (Noterdaeme et al., 2011) and other SZE measurements from clusters (Hurier et al., 2014).

Future analyses will be able to draw upon larger cluster samples (e.g., the full 2500 square degree SPT-SZ survey and the upcoming SPTpol and SPT-3G surveys) and quasar surveys (e.g., SDSS III). By expanding the data volume at high redshifts, these surveys will enable precision tests of the temperature evolution of the CMB across cosmic time. Moreover, because clusters and quasars suffer from different systematics, the comparison will provide an important cross-check on systematics. These surveys will improve constraints on non-standard cosmological models.

The Munich SPT group is supported by the DFG through TR33 “The Dark Universe” and the Cluster of Excellence “Origin and Structure of the Universe”. The South Pole Telescope program is supported by the National Science Foundation through grant ANT-0638937. Partial support is also provided by the NSF Physics Frontier Center grant PHY-0114422 to the Kavli Institute of Cosmological Physics at the University of Chicago, by the Kavli Foundation and the Gordon and Betty Moore Foundation and by NASA grant number PF2-130094. Galaxy cluster research at Harvard is supported by NSF grants AST-1009012 and DGE-

1144152. Galaxy cluster research at SAO is supported in part by NSF grants AST-1009649 and MRI-0723073. The McGill group acknowledges funding from the National Sciences and Engineering Research Council of Canada, Canada Research Chairs program, and the Canadian Institute for Advanced Research.

Chapter 5

Conclusions

In this thesis we reviewed the basic framework of modern cosmology and focused on cosmological studies with galaxy clusters in Chapter 1. Clusters provide rich information about structure formation and are sensitive to the density fluctuations present in the Universe. Among multiple wavelengths, the microwave techniques developed in recent years provide a unique tool to enhance studies of galaxy clusters. The SZE imprints clusters on the CMB via the interaction between hot Intra-Cluster Medium (ICM) gas and CMB photons. In this thesis we capitalise upon the advantages of the SZE to advance our understanding of the Universe.

5.1 Summary of Results

In Chapter 2 we presented results of a study of *Planck* SZE selected galaxy cluster candidates using Panoramic Survey Telescope & Rapid Response System (Pan-STARRS) imaging data. To complete the power of SZE surveys for cosmological investigations, the redshifts of clusters are required. In this work we examined 237 *Planck* galaxy cluster candidates that have no redshift in the *Planck* source catalogue. Among these cluster candidates, we were able to confirm 60 new galaxy clusters and measure their redshifts. We achieved an photometric redshift accuracy of $\sigma_{z/(1+z)} \sim 0.022$ under a blind analysis of 150 *Planck* confirmed galaxy clusters with spectroscopic redshifts. For the rest of the candidates, a further 83 candidates were so heavily contaminated by stars due to their locations near the Galactic plane that we were not able to identify optical counterparts. For the remaining 94 candidates we found no counterparts and expect that the majority are noise fluctuations rather than galaxy clusters, given the contamination estimates from the *Planck* analysis. Nevertheless, we estimate that about a dozen may be higher redshift clusters for which the Pan-STARRS data are not deep enough to enable optical confirmation. Given the depth of the optical imaging for each candidate together with a model of the expected galaxy population for a massive cluster, we assigned a redshift limit beyond which we would not have expected to detect the cluster with at a minimum of 95 percent confidence.

In Chapter 3 we explored the SZE signature of a sample of 46 X-ray selected groups and clusters within SPT 150 GHz and 95 GHz maps. The X-ray sample drawn from $\sim 6\text{deg}^2$ of the *XMM-Newton* Blanco Cosmology Survey (XMM-BCS) probes lower X-ray luminosities ($\sim 10^{42}$ – 10^{44} ergs s^{-1}) up to redshift 1.02, making it complementary to previous studies.

Using X-ray luminosity as a mass proxy, we develop and test an analysis tool that extracts selection-bias corrected constraints on the SZE significance- and Y_{500}-mass relations for low mass clusters and groups. The SZE significance-mass relation is in good agreement with an extrapolation of the relation obtained from high mass clusters. However, the fit to the Y_{500}-mass relation at low masses, while in good agreement with the extrapolation from high mass SPT clusters, is in tension at 2.8σ with the constraints from the *Planck* sample. We examine the tension with the *Planck* relation, discussing sample differences and biases that could contribute to the tension. We also present an analysis of the radio galaxy point source population in this ensemble of X-ray selected systems. We find 18 of our systems have 1 GHz SUMSS sources within 2 arcmin of the X-ray centre, and 3 of these are detected also by SPT. Two of these three SPT point sources are associated with the group BCG, and the third is a quasar candidate. We examine the impact of these point sources on our SZE scaling relation analyses and find no evidence of biases. We also examined the impact of dusty galaxies by stacking the 220 GHz data. We found $2.8\,\sigma$ significant evidence of flux excess, which would correspond to an average underestimate of the SZE signal that is $(17 \pm 9)\,\%$ in this sample of low mass systems. Finally, we explore the impact of improved data that will be available from SPTpol and XMM-XXL, showing that it will lead to a factor of four to five tighter constraints on these SZE mass-observable relations.

In Chapter 4 we used clusters as a tool to examine one prediction of standard cosmology: the adiabatic evolution of the temperature of the CMB blackbody radiation. We used SPT data to study the spectrum of the SZE in a sample of galaxy clusters over a range of redshifts to probe for deviations from the expected adiabatic evolution of the CMB temperature of the form $T(z) = T_0(1+z)^{1-\alpha}$. We developed a method to constrain the temperature evolution of the CMB by the ratio of the SZE signal measured at 95 and 150 GHz in the SPT data. We verified this approach with mock observations of clusters from a new set of hydrodynamical simulations. We applied this method to a sample of 158 SPT-selected clusters from 720 deg^2 spanning a redshift range of $0.05 < z < 1.35$. The measured $\alpha = 0.017^{+0.030}_{-0.028}$, is consistent with the standard model prediction of $\alpha = 0$. Combining with other published results, we find $\alpha = 0.005 \pm 0.012$, an improvement of $\sim 10\%$ over published constraints. In addition analyses of the combined results provides a strong constraint on the effective equation of state in models of decaying dark energy $w_{\rm eff} = -0.994 \pm 0.010$.

5.2 Beyond the Standard Model

Currently the so-called concordance model of the Universe is accurate at the percent level. However, that is only a phenomenological model and we lack a fundamental understanding.

Dark matter has been shown to play a crucial role in the formation of the observed CMB perturbations, in the emergence of massive haloes that host galaxy clusters and in dominating the rotational dynamics of galaxies. But the dark matter particle has not been directly detected in any physics lab on Earth. One begins to question whether there is a real particle to be found?

Dark energy is even more mysterious. It behaves similarly to the vacuum energy discovered in laboratory physics, but its energy density differs from the laboratory dark energy by many orders of magnitude. Theories have been developed in an attempt to explain this difference and to provide a natural explanation for the dark energy, but so far no compelling idea has emerged. The dark energy we measure in the Universe could simply be an indication that

General Relativity (GR) is not a good description of gravity on cosmological distance scales.

In addition, studies of the early universe continue to focus on questions about the initial state of the Big Bang. Did inflation play a key role in the origin of the Universe? Are there additional dimensions?

To obtain improved answers to these questions, we need both theoretical insights and improved observational constraints on cosmological models. Over the past few years projects like *Planck*, SPT and the Sloan Digital Sky Survey (SDSS) have used galaxy clusters to constrain cosmological models. However they are limited by small sample size, large uncertainties in mass and an incomplete understanding of the galaxy cluster selection; this is particularly true in the case of the optical cluster selection methods. In the coming years, new projects will mature that will focus on using multi-wavelength data and improved simulation to address these limitations so that the full power of galaxy cluster samples can be used to address cosmological questions.

In the coming years, the Dark Energy Survey (DES), SPTpol, and ACTpol will continue to explore the dark Universe with state-of-art sensitivities. The eRosita all sky X-ray survey will soon be launched, enabling a new all-sky study of galaxy clusters that is expected to yield samples of 100,000 systems. In the longer term, Euclid, Large Synoptic Survey Telescope (LSST) and James Webb Space Telescope (JWST) are either under development or in the planning stages. All these experiments should address the current limitations of galaxy cluster cosmology, enabling us to reduce the systematic uncertainties present in our current constraints and ultimately delivering constraints that are precise and accurate enough to enable us to robustly test the GR description of gravity on cosmological scales and to characterise spatial and temporal variations in the dark energy.

Bibliography

Abell, G. O. 1958: *The Distribution of Rich Clusters of Galaxies.*, ApJS, 3, 211

Abell, G. O., Corwin, Jr., H. G., & Olowin, R. P. 1989: *A catalog of rich clusters of galaxies*, ApJS, 70, 1

Anderson, L., Aubourg, E., Bailey, S., Bizyaev, D., Blanton, M., Bolton, A. S., Brinkmann, J., Brownstein, J. R., Burden, A., Cuesta, A. J., da Costa, L. A. N., et al. 2012: *The clustering of galaxies in the SDSS-III Baryon Oscillation Spectroscopic Survey: baryon acoustic oscillations in the Data Release 9 spectroscopic galaxy sample*, MNRAS, 427, 3435

Andersson, K., Benson, B. A., Ade, P. A. R., Aird, K. A., Armstrong, B., Bautz, M., Bleem, L. E., Brodwin, M., Carlstrom, J. E., Chang, C. L., Crawford, T. M., et al. 2011: *X-Ray Properties of the First Sunyaev-Zel'dovich Effect Selected Galaxy Cluster Sample from the South Pole Telescope*, ApJ, 738, 48

Arnaud, M., Pratt, G. W., Piffaretti, R., Böhringer, H., Croston, J. H., & Pointecouteau, E. 2010: *The universal galaxy cluster pressure profile from a representative sample of nearby systems (REXCESS) and the Y_{SZ} - M_{500} relation*, A&A, 517, A92

Austermann, J. E., Aird, K. A., Beall, J. A., Becker, D., Bender, A., Benson, B. A., Bleem, L. E., Britton, J., Carlstrom, J. E., Chang, C. L., Chiang, H. C., et al. 2012: *SPTpol: an instrument for CMB polarization measurements with the South Pole Telescope*

Avgoustidis, A., Luzzi, G., Martins, C. J. A. P., & Monteiro, A. M. R. V. L. 2012: *Constraints on the CMB temperature-redshift dependence from SZ and distance measurements*, J. Cosmology Astropart. Phys., 2, 13

Battistelli, E. S., De Petris, M., Lamagna, L., Melchiorri, F., Palladino, E., Savini, G., Cooray, A., Melchiorri, A., Rephaeli, Y., & Shimon, M. 2002: *Cosmic Microwave Background Temperature at Galaxy Clusters*, ApJ, 580, L101

Benson, B. A., Church, S. E., Ade, P. A. R., Bock, J. J., Ganga, K. M., Henson, C. N., & Thompson, K. L. 2004: *Measurements of Sunyaev-Zel'dovich Effect Scaling Relations for Clusters of Galaxies*, ApJ, 617, 829

Benson, B. A., de Haan, T., Dudley, J. P., Reichardt, C. L., Aird, K. A., Andersson, K., Armstrong, R., Ashby, M. L. N., Bautz, M., Bayliss, M., Bazin, G., et al. 2013: *Cosmolog-*

ical Constraints from Sunyaev-Zel'dovich-selected Clusters with X-Ray Observations in the First 178 deg^2 of the South Pole Telescope Survey, ApJ, 763, 147

Bertin, E. 2011: *Automated Morphometry with SExtractor and PSFEx*, in Astronomical Society of the Pacific Conference Series, Vol. 442, Astronomical Data Analysis Software and Systems XX, ed. I. N. Evans, A. Accomazzi, D. J. Mink, & A. H. Rots, 435

Bertin, E. & Arnouts, S. 1996: *SExtractor: Software for source extraction.*, AAPS, 117, 393

Bertin, E., Mellier, Y., Radovich, M., Missonnier, G., Didelon, P., & Morin, B. 2002: *The TERAPIX Pipeline*, in Astronomical Society of the Pacific Conference Series, Vol. 281, Astronomical Data Analysis Software and Systems XI, ed. D. A. Bohlender, D. Durand, & T. H. Handley, 228

Best, P. N., Kauffmann, G., Heckman, T. M., Brinchmann, J., Charlot, S., Ivezić, Ž., & White, S. D. M. 2005: *The host galaxies of radio-loud active galactic nuclei: mass dependences, gas cooling and active galactic nuclei feedback*, MNRAS, 362, 25

Beutler, F., Blake, C., Colless, M., Jones, D. H., Staveley-Smith, L., Campbell, L., Parker, Q., Saunders, W., & Watson, F. 2011: *The 6dF Galaxy Survey: baryon acoustic oscillations and the local Hubble constant*, MNRAS, 416, 3017

Blake, C., Kazin, E. A., Beutler, F., Davis, T. M., Parkinson, D., Brough, S., Colless, M., Contreras, C., Couch, W., Croom, S., Croton, D., et al. 2011: *The WiggleZ Dark Energy Survey: mapping the distance-redshift relation with baryon acoustic oscillations*, MNRAS, 418, 1707

Bleem, L. E. 2013: *A multi-wavelength study of optically selected galaxy clusters from the Blanco Cosmology Survey*, PhD thesis, The University of Chicago

Bock, D. C.-J., Large, M. I., & Sadler, E. M. 1999: *SUMSS: A Wide-Field Radio Imaging Survey of the Southern Sky. I. Science Goals, Survey Design, and Instrumentation*, AJ, 117, 1578

Bocquet, S., Saro, A., Mohr, J. J., Aird, K. A., Ashby, M. L. N., Bautz, M., Bayliss, M., Bazin, G., Benson, B. A., Bleem, L. E., Brodwin, M., et al. 2014: *Mass Calibration and Cosmological Analysis of the SPT-SZ Galaxy Cluster Sample Using Velocity Dispersion σ_v and X-ray Y_X Measurements*, arXiv:1407.2942 [astro-ph.CO]

Böhringer, H., Schuecker, P., Guzzo, L., Collins, C. A., Voges, W., Cruddace, R. G., Ortiz-Gil, A., Chincarini, G., De Grandi, S., Edge, A. C., MacGillivray, H. T., et al. 2004: *The ROSAT-ESO Flux Limited X-ray (REFLEX) Galaxy cluster survey. V. The cluster catalogue*, A&A, 425, 367

Bouy, H., Bertin, E., Moraux, E., Cuillandre, J.-C., Bouvier, J., Barrado, D., Solano, E., & Bayo, A. 2013: *Dynamical analysis of nearby clusters. Automated astrometry from the ground: precision proper motions over a wide field*, A&A, 554, A101

Bruzual, G. & Charlot, S. 2003: *Stellar population synthesis at the resolution of 2003*, MNRAS, 344, 1000

Bryan, G. L. & Norman, M. L. 1998: *Statistical Properties of X-Ray Clusters: Analytic and Numerical Comparisons*, ApJ, 495, 80

Carlstrom, J. E., Ade, P. A. R., Aird, K. A., Benson, B. A., Bleem, L. E., Busetti, S., Chang, C. L., Chauvin, E., Cho, H.-M., Crawford, T. M., Crites, A. T., et al. 2011: *The 10 Meter South Pole Telescope*, PASP, 123, 568

Carlstrom, J. E., Holder, G. P., & Reese, E. D. 2002: *Cosmology with the Sunyaev-Zel'dovich Effect*, ARAA, 40, 643

Carvalho, P., Rocha, G., Hobson, M. P., & Lasenby, A. 2012: *PowellSnakes II: a fast Bayesian approach to discrete object detection in multi-frequency astronomical data sets*, MNRAS, 427, 1384

Cavaliere, A. & Fusco-Femiano, R. 1976: *X-rays from Hot Plasma in Clusters of Galaxies*,A&A, 49, 137

Committee on the Physics of the Universe, N. R. C. 2003, Connecting Quarks with the Cosmos:Eleven Science Questions for the New Century (The National Academies Press)

de Martino, I., Atrio-Barandela, F., da Silva, A., Ebeling, H., Kashlinsky, A., Kocevski, D., & Martins, C. J. A. P. 2012: *Measuring the Redshift Dependence of the Cosmic Microwave Background Monopole Temperature with Planck Data*, ApJ, 757, 144

Desai, S., Armstrong, R., Mohr, J. J., Semler, D. R., Liu, J., Bertin, E., Allam, S. S., Barkhouse, W. A., Bazin, G., Buckley-Geer, E. J., Cooper, M. C., et al. 2012: *The Blanco Cosmology Survey: Data Acquisition, Processing, Calibration, Quality Diagnostics, and Data Release*, ApJ, 757, 83

Dicke, R. H., Peebles, P. J. E., Roll, P. G., & Wilkinson, D. T. 1965: *Cosmic Black-Body Radiation.*, ApJ, 142, 414

Duffy, A. R., Schaye, J., Kay, S. T., & Dalla Vecchia, C. 2008: *Dark matter halo concentrations in the Wilkinson Microwave Anisotropy Probe year 5 cosmology*, MNRAS, 390, L64

Efstathiou, G. 1995: *An anthropic argument for a cosmological constant*, MNRAS, 274, L73

Einstein, A. 1917: *Kosmologische Betrachtungen zur allgemeinen Relativitätstheorie*, Sitzungsberichte der Königlich Preußischen Akademie der Wissenschaften (Berlin), Seite 142-152., 142

Eke, V. R., Cole, S., & Frenk, C. S. 1996: *Cluster evolution as a diagnostic for Omega*, MNRAS, 282, 263

Fabbri, R., Melchiorri, F., & Natale, V. 1978: *The Sunyaev-Zel'dovich effect in the millimetric region*, MNRAS, 282, 263

Fabjan, D., Borgani, S., Tornatore, L., Saro, A., Murante, G., & Dolag, K. 2010: *Simulating the effect of active galactic nuclei feedback on the metal enrichment of galaxy clusters*, MNRAS, 401, 1670

Fixsen, D. J., Cheng, E. S., Gales, J. M., Mather, J. C., Shafer, R. A., & Wright, E. L. 1996: *The Cosmic Microwave Background Spectrum from the Full COBE FIRAS Data Set*, ApJ, 473, 576

Fixsen, D. J., Kogut, A., Levin, S., Limon, M., Lubin, P., Mirel, P., Seiffert, M., Singal, J., Wollack, E., Villela, T., & Wuensche, C. A. 2009: *ARCADE 2 Measurement of the Extra-Galactic Sky Temperature at 3-90 GHz*, arXiv:0901.0555 [astro-ph.CO]

Fowler, J. W., Niemack, M. D., Dicker, S. R., Aboobaker, A. M., Ade, P. A. R., Battistelli, E. S., Devlin, M. J., Fisher, R. P., Halpern, M., Hargrave, P. C., Hincks, A. D., et al. 2007: *Optical design of the Atacama Cosmology Telescope and the Millimeter Bolometric Array Camera*, Applied Optics, 46, 3444

Friedmann, A. 1922: *Über die Krümmung des Raumes*, Zeitschrift fur Physik, 10, 377

Gladders, M. D. & Yee, H. K. C. 2000: *A New Method For Galaxy Cluster Detection. I. The Algorithm*, AJ, 120, 2148

Gladders, M. D. & Yee, H. K. C. 2005: *The Red-Sequence Cluster Survey. I. The Survey and Cluster Catalogs for Patches RCS 0926+37 and RCS 1327+29*, ApJS, 157, 1

Gladders, M. D., Yee, H. K. C., Majumdar, S., Barrientos, L. F., Hoekstra, H., Hall, P. B., & Infante, L. 2007: *Cosmological Constraints from the Red-Sequence Cluster Survey*, ApJ, 655, 128

Gunn, J. E. & Gott, III, J. R. 1972: *On the Infall of Matter Into Clusters of Galaxies and Some Effects on Their Evolution*, ApJ, 176, 1

Guth, A. H. 1981: *Inflationary universe: A possible solution to the horizon and flatness problems*, Phys. Rev. D, 23, 347

Hao, J., McKay, T. A., Koester, B. P., Rykoff, E. S., Rozo, E., Annis, J., Wechsler, R. H., Evrard, A., Siegel, S. R., Becker, M., Busha, M., et al. 2010: *A GMBCG Galaxy Cluster Catalog of 55,424 Rich Clusters from SDSS DR7*, ApJS, 191, 254

Hasselfield, M., Hilton, M., Marriage, T. A., Addison, G. E., Barrientos, L. F., Battaglia, N., Battistelli, E. S., Bond, J. R., Crichton, D., Das, S., Devlin, M. J., et al. 2013: *The Atacama Cosmology Telescope: Sunyaev-Zel'dovich selected galaxy clusters at 148 GHz from three seasons of data*, J. Cosmology Astropart. Phys., 7, 8

Hezaveh, Y., Vanderlinde, K., Holder, G., & de Haan, T. 2013: *Lensing Noise in Millimeter-wave Galaxy Cluster Surveys*, ApJ, 772, 121

High, F. W., Stubbs, C. W., Rest, A., Stalder, B., & Challis, P. 2009: *Stellar Locus Regression: Accurate Color Calibration and the Real-Time Determination of Galaxy Cluster Photometric Redshifts*, AJ, 138, 110

Hinshaw, G., Larson, D., Komatsu, E., Spergel, D. N., Bennett, C. L., Dunkley, J., Nolta, M. R., Halpern, M., Hill, R. S., Odegard, N., Page, L., et al. 2013: *Nine-year Wilkinson Microwave Anisotropy Probe (WMAP) Observations: Cosmological Parameter Results*, ApJS, 208, 19

Hoekstra, H. 2007: *A comparison of weak-lensing masses and X-ray properties of galaxy clusters*, MNRAS, 379, 317

Hoyle, B., Jimenez, R., Verde, L., & Hotchkiss, S. 2012: *A critical analysis of high-redshift, massive, galaxy clusters. Part I*, J. Cosmology Astropart. Phys., 2, 9

Hubble, E. 1929: *A Relation between Distance and Radial Velocity among Extra-Galactic Nebulae*, Proceedings of the National Academy of Science, 15, 168

Hurier, G., Aghanim, N., Douspis, M., & Pointecouteau, E. 2014: *Measurement of the T_{CMB} evolution from the Sunyaev-Zel'dovich effect*, A&A, 561, A143

Itoh, N., Kohyama, Y., & Nozawa, S. 1998: *Relativistic Corrections to the Sunyaev-Zeldovich Effect for Clusters of Galaxies*, ApJ, 502, 7

Jaeckel, J. & Ringwald, A. 2010: *The Low-Energy Frontier of Particle Physics*, Annual Review of Nuclear and Particle Science, 60, 405

Jetzer, P., Puy, D., Signore, M., & Tortora, C. 2011: *Limits on decaying dark energy density models from the CMB temperature-redshift relation*, General Relativity and Gravitation, 43, 1083

Jetzer, P. & Tortora, C. 2011: *Constraints from the CMB temperature and other common observational data sets on variable dark energy density models*, Phys. Rev. D, 84, 043517

Kaiser, N., Aussel, H., Burke, B. E., Boesgaard, H., Chambers, K., Chun, M. R., Heasley, J. N., Hodapp, K.-W., Hunt, B., Jedicke, R., Jewitt, D., et al. 2002: *Pan-STARRS: A Large Synoptic Survey Telescope Array*,in Society of Photo-Optical Instrumentation Engineers (SPIE) Conference Series, Vol. 4836, Survey and Other Telescope Technologies and Discoveries, ed. J. A. Tyson & S. Wolff, 154–164

Klein, J. R. & Roodman, A. 2005: *Blind Analysis in Nuclear and Particle Physics*, Annual Review of Nuclear and Particle Science, 55, 141

Koester, B. P., McKay, T. A., Annis, J., Wechsler, R. H., Evrard, A., Bleem, L., Becker, M., Johnston, D., Sheldon, E., Nichol, R., Miller, C., et al. 2007: *A MaxBCG Catalog of 13,823 Galaxy Clusters from the Sloan Digital Sky Survey*, ApJ, 660, 239

Komatsu, E., Smith, K. M., Dunkley, J., Bennett, C. L., Gold, B., Hinshaw, G., Jarosik, N., Larson, D., Nolta, M. R., Page, L., Spergel, D. N., et al. 2011: *Seven-year Wilkinson Microwave Anisotropy Probe (WMAP) Observations: Cosmological Interpretation*, ApJS, 192, 18

Lacey, C. & Cole, S. 1993: *Merger rates in hierarchical models of galaxy formation*, MNRAS, 262, 627

Laganá, T. F., Martinet, N., Durret, F., Lima Neto, G. B., Maughan, B., & Zhang, Y.-Y. 2013: *A comprehensive picture of baryons in groups and clusters of galaxies*, A&A, 555, A66

Lemaître, G. 1927: *Un Univers homogène de masse constante et de rayon croissant rendant compte de la vitesse radiale des nébuleuses extra-galactiques*, Annales de la Societe Scietifique de Bruxelles, 47, 49

Lima, J. A. S., Silva, A. I., & Viegas, S. M. 2000: *Is the radiation temperature-redshift relation of the standard cosmology in accordance with the data?*, MNRAS, 312, 747

Lin, Y., Mohr, J. J., & Stanford, S. A. 2004: *K-Band Properties of Galaxy Clusters and Groups: Luminosity Function, Radial Distribution, and Halo Occupation Number*, ApJ, 610, 745

Lin, Y., Partridge, B., Pober, J. C., Bouchefry, K. E., Burke, S., Klein, J. N., Coish, J. W., & Huffenberger, K. M. 2009: *Spectral Energy Distribution of Radio Sources in Nearby Clusters of Galaxies: Implications for Sunyaev-Zel'Dovich Effect Surveys*, ApJ, 694, 992

Lin, Y.-T. & Mohr, J. J. 2007: *Radio Sources in Galaxy Clusters: Radial Distribution, and 1.4 GHz and K-band Bivariate Luminosity Function*, ApJS, 170, 71

Luzzi, G., Shimon, M., Lamagna, L., Rephaeli, Y., De Petris, M., Conte, A., De Gregori, S., & Battistelli, E. S. 2009: *Redshift Dependence of the Cosmic Microwave Background Temperature from Sunyaev-Zeldovich Measurements*, ApJ, 705, 1122

Majumdar, S. & Mohr, J. J. 2004: *Self-Calibration in Cluster Studies of Dark Energy: Combining the Cluster Redshift Distribution, the Power Spectrum, and Mass Measurements*, ApJ, 613, 41

Mana, A., Giannantonio, T., Weller, J., Hoyle, B., Hütsi, G., & Sartoris, B. 2013: *Combining clustering and abundances of galaxy clusters to test cosmology and primordial non-Gaussianity*, MNRAS, 434, 684

Mancone, C. L. & Gonzalez, A. H. 2012: *EzGal: A Flexible Interface for Stellar Population Synthesis Models*, PASP, 124, 606

Mantz, A., Allen, S. W., Ebeling, H., Rapetti, D., & Drlica-Wagner, A. 2010a: *The observed growth of massive galaxy clusters - II. X-ray scaling relations*, MNRAS, 406, 1773

Mantz, A., Allen, S. W., Rapetti, D., & Ebeling, H. 2010b: *The observed growth of massive galaxy clusters - I. Statistical methods and cosmological constraints*, MNRAS, 406, 1759

Martins, C. J. A. P. 2002: *Cosmology with varying constants*, Royal Society of London Philosophical Transactions Series A, 360, 2681

Matyjasek, J. 1995: *Cosmological models with a time-dependent Λ term*, Phys. Rev. D, 51, 4154

Mauch, T., Murphy, T., Buttery, H. J., Curran, J., Hunstead, R. W., Piestrzynski, B., Robertson, J. G., & Sadler, E. M. 2003: *SUMSS: A Wide-Field Radio Imaging Survey of the Southern Sky - II. The Source Catalogue*, MNRAS, 342, 1117

McDonald, M., Benson, B. A., Vikhlinin, A., Stalder, B., Bleem, L. E., de Haan, T., Lin, H. W., Aird, K. A., Ashby, M. L. N., Bautz, M. W., Bayliss, M., et al. 2013: *The Growth of Cool Cores and Evolution of Cooling Properties in a Sample of 83 Galaxy Clusters at $0.3 \leq z \leq 1.2$ Selected from the SPT-SZ Survey*, ApJ, 774, 23

Mehrtens, N., Romer, A. K., Hilton, M., Lloyd-Davies, E. J., Miller, C. J., Stanford, S. A., Hosmer, M., Hoyle, B., Collins, C. A., Liddle, A. R., Viana, P. T. P., et al. 2012: *The XMM Cluster Survey: optical analysis methodology and the first data release*, MNRAS, 423, 1024

Melin, J.-B., Aghanim, N., Bartelmann, M., Bartlett, J. G., Betoule, M., Bobin, J., Carvalho, P., Chon, G., Delabrouille, J., Diego, J. M., Harrison, D. L., et al. 2012: *A comparison of algorithms for the construction of SZ cluster catalogues*, A&A, 548, A51

Melin, J.-B., Bartlett, J. G., & Delabrouille, J. 2005: *The selection function of SZ cluster surveys*, A&A, 429, 417

Melin, J.-B., Bartlett, J. G., & Delabrouille, J. 2006: *Catalog extraction in SZ cluster surveys: a matched filter approach*, A&A, 459, 341

Metcalfe, N., Farrow, D. J., Cole, S., Draper, P. W., Norberg, P., Burgett, W. S., Chambers, K. C., Denneau, L., Flewelling, H., Kaiser, N., Kudritzki, R., et al. 2013: *The Pan-STARRS1 Small Area Survey 2*, MNRAS, 435, 1825

Mohr, J. J., Adams, D., Barkhouse, W., Beldica, C., Bertin, E., Cai, Y. D., da Costa, L. A. N., Darnell, J. A., Daues, G. E., Jarvis, M., Gower, M., et al. 2008: *The Dark Energy Survey data management system*, in Society of Photo-Optical Instrumentation Engineers (SPIE) Conference Series, Vol. 7016

Mohr, J. J., Armstrong, R., Bertin, E., Daues, G., Desai, S., Gower, M., Gruendl, R., Hanlon, W., Kuropatkin, N., Lin, H., Marriner, J., et al. 2012: *The Dark Energy Survey data processing and calibration system*, in Society of Photo-Optical Instrumentation Engineers (SPIE) Conference Series, Vol. 8451

Mohr, J. J., Mathiesen, B., & Evrard, A. E. 1999: *Properties of the Intracluster Medium in an Ensemble of Nearby Galaxy Clusters*, ApJ, 517, 627

Molaro, P., Levshakov, S. A., Dessauges-Zavadsky, M., & D'Odorico, S. 2002: *The cosmic microwave background radiation temperature at $z_{abs} = 3.025$ toward QSO 0347-3819*, A&A, 381, L64

Molnar, S. M., Hearn, N. C., & Stadel, J. G. 2012: *Merging Galaxy Clusters: Offset between the Sunyaev-Zel'dovich Effect and X-Ray Peaks*,ApJ, 748, 45

Mortonson, M. J., Hu, W., & Huterer, D. 2011: *Simultaneous falsification of ΛCDM and quintessence with massive, distant clusters*, Phys. Rev. D, 83, 023015

Motl, P. M., Hallman, E. J., Burns, J. O., & Norman, M. L. 2005: *The Integrated Sunyaev-Zeldovich Effect as a Superior Method for Measuring the Mass of Clusters of Galaxies*, Phys. Rev. D, 83, 023015

Muller, S., Beelen, A., Black, J. H., Curran, S. J., Horellou, C., Aalto, S., Combes, F., Guélin, M., & Henkel, C. 2013: *A precise and accurate determination of the cosmic microwave background temperature at $z = 0.89$*, A&A, 551, A109

Murphy, M. T., Webb, J. K., & Flambaum, V. V. 2003: *Further evidence for a variable fine-structure constant from Keck/HIRES QSO absorption spectra*, MNRAS, 345, 609

Nagai, D., Kravtsov, A. V., & Vikhlinin, A. 2007: *Effects of Galaxy Formation on Thermodynamics of the Intracluster Medium*, ApJ, 668, 1

Navarro, J. F., Frenk, C. S., & White, S. D. M. 1997: *A Universal Density Profile from Hierarchical Clustering*, ApJ, 490, 493

Ngeow, C., Mohr, J. J., Alam, T., Barkhouse, W. A., Beldica, C., Cai, D., Daues, G., Plante, R., Annis, J., Lin, H., Tucker, D., et al. 2006: *Cyber-infrastructure to support science and data management for the Dark Energy Survey*, in Society of Photo-Optical Instrumentation Engineers (SPIE) Conference Series, Vol. 6270

Noterdaeme, P., Petitjean, P., Srianand, R., Ledoux, C., & López, S. 2011: *The evolution of the cosmic microwave background temperature. Measurements of T_{CMB} at high redshift from carbon monoxide excitation*, A&A, 526, L7

Olsen, L. F., Scodeggio, M., da Costa, L., Benoist, C., Bertin, E., Deul, E., Erben, T., Guarnieri, M. D., Hook, R., Nonino, M., Prandoni, I., et al. 1999: *ESO imaging survey. II. Searching for distant clusters of galaxies*, A&A, 345, 681

Overduin, J. M. & Cooperstock, F. I. 1998: *Evolution of the scale factor with a variable cosmological term*, Phys. Rev. D, 58, 043506

Padmanabhan, N., Xu, X., Eisenstein, D. J., Scalzo, R., Cuesta, A. J., Mehta, K. T., & Kazin, E. 2012: *A 2 per cent distance to $z = 0.35$ by reconstructing baryon acoustic oscillations - I. Methods and application to the Sloan Digital Sky Survey*, MNRAS, 427, 2132

Peebles, P. J. E. & Yu, J. T. 1970: *Primeval Adiabatic Perturbation in an Expanding Universe*, ApJ, 162, 815

Penzias, A. A. & Wilson, R. W. 1965: *A Measurement of Excess Antenna Temperature at 4080 Mc/s.*, ApJ, 142, 419

Perlmutter, S., Aldering, G., Goldhaber, G., Knop, R. A., Nugent, P., Castro, P. G., Deustua, S., Fabbro, S., Goobar, A., Groom, D. E., Hook, I. M., et al. 1999: *Measurements of Ω and Λ from 42 High-Redshift Supernovae*,ApJ, 517, 565

Phillips, M. M. 1993: *The absolute magnitudes of Type IA supernovae*, ApJ, 413, L105

Pierre, M., Pacaud, F., Juin, J. B., Melin, J. B., Valageas, P., Clerc, N., & Corasaniti, P. S. 2011: *Precision cosmology with a wide area XMM cluster survey*, MNRAS, 414, 1732

Piffaretti, R., Arnaud, M., Pratt, G. W., Pointecouteau, E., & Melin, J.-B. 2011: *The MCXC: a meta-catalogue of x-ray detected clusters of galaxies*, A&A, 534, A109

Plagge, T., Benson, B. A., Ade, P. A. R., Aird, K. A., Bleem, L. E., Carlstrom, J. E., Chang, C. L., Cho, H., Crawford, T. M., Crites, A. T., de Haan, T., et al. 2010: *Sunyaev-Zel'dovich Cluster Profiles Measured with the South Pole Telescope*, ApJ, 716, 1118

Planck Collaboration, 2011: *Planck early results. X. Statistical analysis of Sunyaev-Zeldovich scaling relations for X-ray galaxy clusters*, A&A, 536, A10

Planck Collaboration, 2013a: *Planck 2013 results. XXIX. Planck catalogue of Sunyaev-Zeldovich sources*, arXiv:1303.5089 [astro-ph.CO]

Planck Collaboration, 2013b: *Planck 2013 results. XVI. Cosmological parameters*, arXiv:1303.5076 [astro-ph.CO]

Planck Collaboration, 2013c: *Planck 2013 results. XX. Cosmology from Sunyaev-Zeldovich cluster counts*, arXiv:1303.5080 [astro-ph.CO]

Poggianti, B. M., Bridges, T. J., Mobasher, B., Carter, D., Doi, M., Iye, M., Kashikawa, N., Komiyama, Y., Okamura, S., Sekiguchi, M., Shimasaku, K., et al. 2001: *A Photometric and Spectroscopic Study of Dwarf and Giant Galaxies in the Coma Cluster. III. Spectral Ages and Metallicities*, ApJ, 562, 689

Postman, M., Lubin, L. M., Gunn, J. E., Oke, J. B., Hoessel, J. G., Schneider, D. P., & Christensen, J. A. 1996: *The Palomar Distant Clusters Survey. I. The Cluster Catalog*, AJ, 111, 615

Pratt, G. W., Croston, J. H., Arnaud, M., & Böhringer, H. 2009: *Galaxy cluster X-ray luminosity scaling relations from a representative local sample (REXCESS)*, A&A, 498, 361

Press, W. & Schechter, P. 1974: *Formation of Galaxies and Clusters of Galaxies by Self-Similar Gravitational Condensation*, ApJ, 187, 425

Puy, D. 2004: *Thermal balance in decaying Λ cosmologies*, A&A, 422, 1

Reichardt, C. L., Stalder, B., Bleem, L. E., Montroy, T. E., Aird, K. A., Andersson, K., Armstrong, R., Ashby, M. L. N., Bautz, M., Bayliss, M., Bazin, G., et al. 2013: *Galaxy Clusters Discovered via the Sunyaev-Zel'dovich Effect in the First 720 Square Degrees of the South Pole Telescope Survey*, ApJ, 763, 127

Rephaeli, Y. 1980: *On the determination of the degree of cosmological Compton distortions and the temperature of the cosmic blackbody radiation*, ApJ, 241, 858

Riess, A. G., Filippenko, A. V., Challis, P., Clocchiatti, A., Diercks, A., Garnavich, P. M., Gilliland, R. L., Hogan, C. J., Jha, S., Kirshner, R. P., Leibundgut, B., et al. 1998: *Observational Evidence from Supernovae for an Accelerating Universe and a Cosmological Constant*, AJ, 116, 1009

Robertson, H. P. 1935: *Kinematics and World-Structure*, ApJ, 82, 284

Rosati, P., della Ceca, R., Norman, C., & Giacconi, R. 1998: *The ROSAT Deep Cluster Survey: The X-Ray Luminosity Function Out to z=0.8*, ApJ, 82, 284

Rozo, E. & Rykoff, E. S. 2014: *redMaPPer II: X-Ray and SZ Performance Benchmarks for the SDSS Catalog*, ApJ, 783, 80

Rozo, E., Rykoff, E. S., Bartlett, J. G., & Melin, J. B. 2014: *redMaPPer III: A Detailed Comparison of the Planck 2013 and SDSS DR8 RedMaPPer Cluster Catalogs*, arXiv:1401.7716 [astro-ph.CO]

Rozo, E., Wechsler, R. H., Rykoff, E. S., Annis, J. T., Becker, M. R., Evrard, A. E., Frieman, J. A., Hansen, S. M., Hao, J., Johnston, D. E., Koester, B. P., et al. 2010: *Cosmological Constraints from the Sloan Digital Sky Survey maxBCG Cluster Catalog*, ApJ, 708, 645

Rykoff, E. S., Rozo, E., Busha, M. T., Cunha, C. E., Finoguenov, A., Evrard, A., Hao, J., Koester, B. P., Leauthaud, A., Nord, B., Pierre, M., et al. 2014: *redMaPPer. I. Algorithm and SDSS DR8 Catalog*, ApJ, 785, 104

Saliwanchik, B. R., Montroy, T. E., Aird, K. A., Bayliss, M., Benson, B. A., Bleem, L. E., Bocquet, S., Brodwin, M., Carlstrom, J. E., Chang, C. L., Cho, H. M., et al. 2013: *Measurement of Galaxy Cluster Integrated Comptonization and Mass Scaling Relations with the South Pole Telescope*, arXiv:1312.3015 [astro-ph.CO]

Sarazin, C. L. 1988, X-Ray Emission from Clusters of Galaxies, Cambridge Astrophysics Series (Cambridge University, Cambridge, UK), 212

Saro, A., Liu, J., Mohr, J. J., Aird, K. A., Ashby, M. L. N., Bayliss, M., Benson, B. A., Bleem, L. E., Bocquet, S., Brodwin, M., Carlstrom, J. E., et al. 2014: *Constraints on the CMB temperature evolution using multiband measurements of the Sunyaev-Zel'dovich effect with the South Pole Telescope*, MNRAS, 440, 2610

Schaffer, K. K., Crawford, T. M., Aird, K. A., Benson, B. A., Bleem, L. E., Carlstrom, J. E., Chang, C. L., Cho, H. M., Crites, A. T., de Haan, T., Dobbs, M. A., et al. 2011: *The First Public Release of South Pole Telescope Data: Maps of a 95 deg^2 Field from 2008 Observations*, ApJ, 743, 90

Schechter, P. 1976: *An analytic expression for the luminosity function for galaxies.*, ApJ, 203, 297

Schlafly, E. F., Finkbeiner, D. P., Jurić, M., Magnier, E. A., Burgett, W. S., Chambers, K. C., Grav, T., Hodapp, K. W., Kaiser, N., Kudritzki, R.-P., Martin, N. F., et al. 2012: *Photometric Calibration of the First 1.5 Years of the Pan-STARRS1 Survey*, ApJ, 756, 158

Schlegel, D. J., Finkbeiner, D. P., & Davis, M. 1998: *Maps of Dust Infrared Emission for Use in Estimation of Reddening and Cosmic Microwave Background Radiation Foregrounds*, ApJ, 500, 525

Semler, D. R., Šuhada, R., Aird, K. A., Ashby, M. L. N., Bautz, M., Bayliss, M., Bazin, G., Bocquet, S., Benson, B. A., Bleem, L. E., Brodwin, M., et al. 2012: *High-Redshift Cool-Core Galaxy Clusters Detected via the Sunyaev-Zel'dovich Effect in the South Pole Telescope Survey*, ApJ, 761, 183

Sheth, R. K. & Tormen, G. 1999: *Large-scale bias and the peak background split*, MNRAS, 308, 119

Shirokoff, E., Reichardt, C. L., Shaw, L., Millea, M., Ade, P. A. R., Aird, K. A., Benson, B. A., Bleem, L. E., Carlstrom, J. E., Chang, C. L., Cho, H. M., et al. 2011: *Improved Constraints on Cosmic Microwave Background Secondary Anisotropies from the Complete 2008 South Pole Telescope Data*, ApJ, 736, 61

Skrutskie, M. F., Cutri, R. M., Stiening, R., Weinberg, M. D., Schneider, S., Carpenter, J. M., Beichman, C., Capps, R., Chester, T., Elias, J., Huchra, J., et al. 2006: *The Two Micron All Sky Survey (2MASS)*, AJ, 131, 1163

Song, J., Mohr, J. J., Barkhouse, W. A., Warren, M. S., & Rude, C. 2012a: *A Parametrized Galaxy Catalog Simulator For Testing Cluster Finding, Mass Estimation and Photometric Redshift Estimation in Optical and Near Infrared Surveys*, ApJ, 747, 58

Song, J., Zenteno, A., Stalder, B., Desai, S., Bleem, L. E., Aird, K. A., Armstrong, R., Ashby, M. L. N., Bayliss, M., Bazin, G., Benson, B. A., et al. 2012b: *Redshifts, Sample Purity, and BCG Positions for the Galaxy Cluster Catalog from the First 720 Square Degrees of the South Pole Telescope Survey*, ApJ, 761, 22

Springel, V. 2005: *The cosmological simulation code GADGET-2*, MNRAS, 364, 1105

Springel, V. & Hernquist, L. 2002: *Cosmological smoothed particle hydrodynamics simulations: the entropy equation*, MNRAS, 333, 649

Springel, V. & Hernquist, L. 2003: *Cosmological smoothed particle hydrodynamics simulations: a hybrid multiphase model for star formation*, MNRAS, 339, 289

Srianand, R., Chand, H., Petitjean, P., & Aracil, B. 2004: *Limits on the Time Variation of the Electromagnetic Fine-Structure Constant in the Low Energy Limit from Absorption Lines in the Spectra of Distant Quasars*, MNRAS, 339, 289

Srianand, R., Noterdaeme, P., Ledoux, C., & Petitjean, P. 2008: *First detection of CO in a high-redshift damped Lyman-α system*, A&A, 482, L39

Srianand, R., Petitjean, P., & Ledoux, C. 2000: *The cosmic microwave background radiation temperature at a redshift of 2.34*, Nature, 408, 931

Stanek, R., Evrard, A. E., Böhringer, H., Schuecker, P., & Nord, B. 2006: *The X-Ray Luminosity-Mass Relation for Local Clusters of Galaxies*, ApJ, 648, 956

Staniszewski, Z., Ade, P. A. R., Aird, K. A., Benson, B. A., Bleem, L. E., Carlstrom, J. E., Chang, C. L., Cho, H.-M., Crawford, T. M., Crites, A. T., de Haan, T., et al. 2009: *Galaxy Clusters Discovered with a Sunyaev-Zel'dovich Effect Survey*, ApJ, 701, 32

Story, K. T., Reichardt, C. L., Hou, Z., Keisler, R., Aird, K. A., Benson, B. A., Bleem, L. E., Carlstrom, J. E., Chang, C. L., Cho, H.-M., Crawford, T. M., et al. 2013: *A Measurement of the Cosmic Microwave Background Damping Tail from the 2500-Square-Degree SPT-SZ Survey*, ApJ, 779, 86

Sun, M., Voit, G. M., Donahue, M., Jones, C., Forman, W., & Vikhlinin, A. 2009: *Chandra Studies of the X-Ray Gas Properties of Galaxy Groups*, ApJ, 693, 1142

Sunyaev, R. A. & Zel'dovich, Y. B. 1970: *The Spectrum of Primordial Radiation, its Distortions and their Significance*, Comments on Astrophysics and Space Physics, 2, 66

Sunyaev, R. A. & Zel'dovich, Y. B. 1972: *The Observations of Relic Radiation as a Test of the Nature of X-Ray Radiation from the Clusters of Galaxies*,Comments on Astrophysics and Space Physics, 4, 173

Sunyaev, R. A. & Zeldovich, Y. B. 1980: *The Velocity of Clusters of Galaxies Relative to the Microwave Background - The Possibility of its Measurement*, MNRAS, 190, 413

Susskind, L. 2003: *The Anthropic Landscape of String Theory*, in The Davis Meeting On Cosmic Inflation

Szabo, T., Pierpaoli, E., Dong, F., Pipino, A., & Gunn, J. 2011: *An Optical Catalog of Galaxy Clusters Obtained from an Adaptive Matched Filter Finder Applied to Sloan Digital Sky Survey Data Release 6*, ApJ, 736, 21

Szalay, A. S., Connolly, A. J., & Szokoly, G. P. 1999: *Simultaneous Multicolor Detection of Faint Galaxies in the Hubble Deep Field*, AJ, 117, 68

Tauber, J. A., Mandolesi, N., Puget, J.-L., Banos, T., Bersanelli, M., Bouchet, F. R., Butler, R. C., Charra, J., Crone, G., Dodsworth, J., & et al. 2010: *Planck pre-launch status: The Planck mission*, A&A, 520, A1

Tinker, J., Kravtsov, A. V., Klypin, A., Abazajian, K., Warren, M., Yepes, G., Gottlöber, S., & Holz, D. E. 2008: *Toward a Halo Mass Function for Precision Cosmology: The Limits of Universality*, A&A, 520, A1

Tolman, R. C. 1934, Relativity, Thermodynamics, and Cosmology (Clarendon Press)

Tonry, J. L., Stubbs, C. W., Lykke, K. R., Doherty, P., Shivvers, I. S., Burgett, W. S., Chambers, K. C., Hodapp, K. W., Kaiser, N., Kudritzki, R.-P., Magnier, E. A., et al. 2012: *The Pan-STARRS1 Photometric System*, ApJ, 750, 99

Šuhada, R., Song, J., Böhringer, H., Mohr, J. J., Chon, G., Finoguenov, A., Fassbender, R., Desai, S., Armstrong, R., Zenteno, A., Barkhouse, W. A., et al. 2012: *The XMM-BCS galaxy cluster survey. I. The X-ray selected cluster catalog from the initial 6 deg*^{2}, A&A, 537, A39

Vanderlinde, K., Crawford, T. M., de Haan, T., Dudley, J. P., Shaw, L., Ade, P. A. R., Aird, K. A., Benson, B. A., Bleem, L. E., Brodwin, M., Carlstrom, J. E., et al. 2010: *Galaxy Clusters Selected with the Sunyaev-Zel'dovich Effect from 2008 South Pole Telescope Observations*, ApJ, 722, 1180

Vieira, J. D., Crawford, T. M., Switzer, E. R., Ade, P. A. R., Aird, K. A., Ashby, M. L. N., Benson, B. A., Bleem, L. E., Brodwin, M., Carlstrom, J. E., Chang, C. L., et al. 2010: *Extragalactic Millimeter-wave Sources in South Pole Telescope Survey Data: Source Counts, Catalog, and Statistics for an 87 Square-degree Field*, ApJ, 719, 763

Vikhlinin, A., Burenin, R. A., Ebeling, H., Forman, W. R., Hornstrup, A., Jones, C., Kravtsov, A. V., Murray, S. S., Nagai, D., Quintana, H., & Voevodkin, A. 2009a: *Chandra Cluster Cosmology Project. II. Samples and X-Ray Data Reduction*, ApJ, 692, 1033

Vikhlinin, A., Kravtsov, A. V., Burenin, R. A., Ebeling, H., Forman, W. R., Hornstrup, A., Jones, C., Murray, S. S., Nagai, D., Quintana, H., & Voevodkin, A. 2009b: *Chandra Cluster Cosmology Project III: Cosmological Parameter Constraints*, ApJ, 692, 1060

Voges, W., Aschenbach, B., Boller, T., Bräuninger, H., Briel, U., Burkert, W., Dennerl, K., Englhauser, J., Gruber, R., Haberl, F., Hartner, G., et al. 1999: *The ROSAT all-sky survey bright source catalogue*, A&A, 349, 389

Voit, G. M. 2005: *Tracing cosmic evolution with clusters of galaxies*, A&A, 349, 389

von der Linden, A., Allen, M. T., Applegate, D. E., Kelly, P. L., Allen, S. W., Ebeling, H., Burchat, P. R., Burke, D. L., Donovan, D., Morris, R. G., Blandford, R., et al. 2014: *Weighing the Giants - I. Weak-lensing masses for 51 massive galaxy clusters: project overview, data analysis methods and cluster images*, MNRAS, 439, 2

Walker, A. G. 1937: *On Milne's Theory of World-Structure*, Proceedings of the London Mathematical Society, s2-42, 90

Watson, W. A., Iliev, I. T., D'Aloisio, A., Knebe, A., Shapiro, P. R., & Yepes, G. 2013: *The halo mass function through the cosmic ages*, MNRAS, 433, 1230

Wen, Z. L., Han, J. L., & Liu, F. S. 2012: *A Catalog of 132,684 Clusters of Galaxies Identified from Sloan Digital Sky Survey III*, ApJS, 199, 34

Weymann, R. 1966: *The Energy Spectrum of Radiation in the Expanding Universe*, ApJ, 145, 560

White, S. D. M., Efstathiou, G., & Frenk, C. S. 1993: *The amplitude of mass fluctuations in the universe*, MNRAS, 262, 1023

Williamson, R., Benson, B. A., High, F. W., Vanderlinde, K., Ade, P. A. R., Aird, K. A., Andersson, K., Armstrong, R., Ashby, M. L. N., Bautz, M., Bazin, G., et al. 2011: *A Sunyaev-Zel'dovich-selected Sample of the Most Massive Galaxy Clusters in the 2500 deg^2 South Pole Telescope Survey*, ApJ, 738, 139

Wright, A. & Otrupcek, R. 1990: *Parkes Catalog, 1990, Australia telescope national facility.*, in PKS Catalog (1990)

Wright, E. L., Eisenhardt, P. R. M., Mainzer, A. K., Ressler, M. E., Cutri, R. M., Jarrett, T., Kirkpatrick, J. D., Padgett, D., McMillan, R. S., Skrutskie, M., Stanford, S. A., et al. 2010: *The Wide-field Infrared Survey Explorer (WISE): Mission Description and Initial On-orbit Performance*, AJ, 140, 1868

Wright, E. L., Meyer, S. S., Bennett, C. L., Boggess, N. W., Cheng, E. S., Hauser, M. G., Kogut, A., Lineweaver, C., Mather, J. C., Smoot, G. F., Weiss, R., et al. 1992: *Interpretation of the cosmic microwave background radiation anisotropy detected by the COBE Differential Microwave Radiometer*, ApJ, 396, L13

York, D. G., Adelman, J., Anderson, Jr., J. E., Anderson, S. F., Annis, J., Bahcall, N. A., Bakken, J. A., Barkhouser, R., Bastian, S., Berman, E., Boroski, W. N., et al. 2000: *The Sloan Digital Sky Survey: Technical Summary*, AJ, 120, 1579

Zenteno, A., Song, J., Desai, S., Armstrong, R., Mohr, J. J., Ngeow, C.-C., Barkhouse, W. A., Allam, S. S., Andersson, K., Bazin, G., Benson, B. A., et al. 2011: *A Multiband Study of the Galaxy Populations of the First Four Sunyaev-Zel'dovich Effect Selected Galaxy Clusters*, ApJ, 734, 3

Acknowledgements

I would like to express my gratitude to my advisor, Joe Mohr, for his advice and support and for providing me with the opportunity to work with the amazing group of scientists in different projects. Without him I could not have finished my study of different aspects of cluster cosmology research.

I would like to thank current and former postdocs at the Ludwig-Maximilians-Universität. It has been a joyful experience to work with Alex Saro in various projects. And the curiosity, profession and acumen by Shantanu Desai, Jörg Dietrich, Robert Šuhada, and Gurvan Bazin have guided me to explore the frontiers of the Universe.

I'd also like to thank my fellow students, Sebastian Bocquet, Christina Hennig, I-Non Chiu, Dominik C. Gangkofner, Alfredo Zenteno, and Jeesong Song for their insightful discussions. Thank you also to all the people in the South Pole Telescope collaboration and at the University Observatory at Munich (USM). Also thanks to our secretary Uta Le Guay, without her help, the life in Munich would be much harder.

Finally, thanks to my lovely family, whose unconditional support, care and love have supported me throughout my studies. Especially, thank you, Jing Jin, my wife, my best friend, for sharing the passion and ups and downs in life.

Curriculum Vitae

Jiayi Liu

Education

2010–2014	PhD in Physics, Ludwig-Maximilians-University, Munich, Germany
2008–2010	Master in Astronomy, University of Illinois, Champaign-Urbana, IL, United States
2004–2008	Bachelor in Physics, Peking University, Beijing, China
2001–2004	High School, The high school affiliated Renmin University of China, Beijing, China
1998–2001	Primary School, Renda school, Beijing, China

List of scientific publications

Refereed publications

- Saro, A.; **Liu, J.**, (68 co-authors) 2014, *Constraints on the CMB Temperature Evolution using Multi-Band Measurements of the Sunyaev Zeldovich Effect with the South Pole Telescope.* MNRAS, 440, 2610S

- Fan, Z.; Shan, H.; **Liu, J.** 2010, *Noisy Weak-lensing Convergence Peak Statistics Near Clusters of Galaxies and Beyond.* ApJ, 719, 1408

- McDonald, M.; (77 co-authors); **Liu, J.** 2013, *The Growth of Cool Cores and Evolution of Cooling Properties in a Sample of 83 Galaxy Clusters at* $0.3 < z < 1.2$ *Selected from the SPT-SZ Survey.* ApJ, 744, 23

- Benson, B. A.; (74 co-authors); **Liu, J.** 2013: *Cosmological Constraints from Sunyaev-Zel'dovich-Selected Clusters with X-ray Observations in the First 178 Square Degrees of the South Pole Telescope Survey.* ApJ, 763, 147B

- Reichardt, C. L.; (78 co-authors); **Liu, J.** 2013, *Galaxy clusters discovered via the Sunyaev-Zel'dovich effect in the first 720 square degrees of the South Pole Telescope survey.* ApJ, 763, 127R

- Stalder, B.; (81 co-authors); **Liu, J.** 2013: *SPT-CL J0205-5829: A* $z = 1.32$ *evolved massive galaxy cluster in the south pole telescope Sunyaev-Zel'dovich effect survey.* ApJ, 763, 93

- Semler, D. R.; (77 co-authors); **Liu, J.** 2012, *High-Redshift Cool-Core Galaxy Clusters Detected via the Sunyaev-Zel'dovich Effect in the South Pole Telescope Survey.* ApJ, 761, 183S

- Song, J.; (75 co-authors); **Liu, J.** 2012: *Redshifts, Sample Purity, and BCG Positions for the Galaxy Cluster Catalog from the first 720 Square Degrees of the South Pole Telescope Survey.* ApJ, 761, 22S

- High, F. W.; (84 co-authors); **Liu, J.** 2012, *Weak-Lensing Mass Measurements of Five Galaxy Clusters in the South Pole Telescope Survey Using Magellan/Megacam.* ApJ, 758, 68H

- Desai, S.; (18 co-authors); **Liu, J.** 2012, *The Blanco Cosmology Survey: Data Acquisition, Processing, Calibration, Quality Diagnostics and Data Release.* ApJ, 757, 83D
- McDonald, M.; (84 co-authors); **Liu, J.** 2012, *A massive, cooling-flow-induced starburst in the core of a luminous cluster of galaxies.* Nature, 488, 349
- Desai, S; (22 co-authors), **Liu, J.** 2012, *Optical followup of galaxy clusters detected by the South Pole Telescope.* J. Phys.: Conf. Ser. 375,032011
- Zenteno, A; (23 co-authors), **Liu, J.** 2011, *A Multiband Study of the Galaxy Populations of the First Four Sunyaev-Zel'dovich Effect Selected Galaxy Clusters.* ApJ, 734, 3Z